Technische Universität München

Physik Department

MPQ

Electric Field Controlled Collisions of Trapped Polyatomic Molecules

Manuel Koller

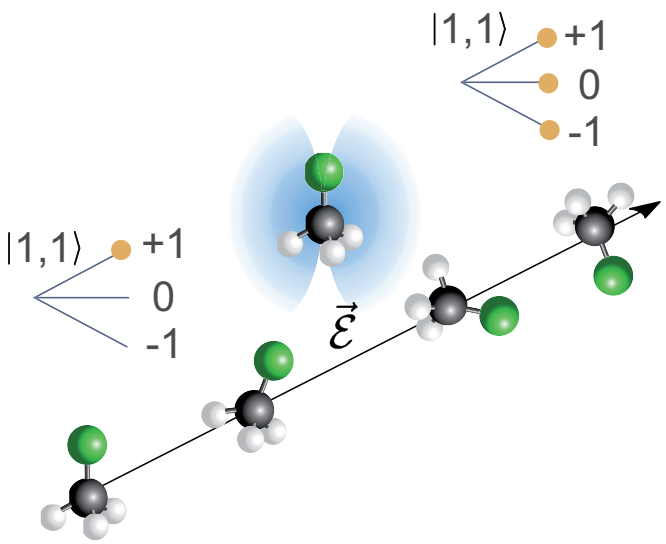

Dissertation

Max-Planck-Institut für Quantenoptik, Garching
and Physik Department, Technische Universität München

December 2021

Cover illustration: Schematic illustration of dipolar relaxation for two molecules in $|J = 1, K = 1\rangle$ in the presence of an external electric field.

Fakultät für Physik der Technischen Universität München

Electric Field Controlled Collisions of Trapped Polyatomic Molecules

Manuel Koller

Vollständiger Abdruck der von der Fakultät für Physik der Technischen Universität München zur Erlangung eines

Doktors der Naturwissenschaften (Dr. rer. nat.)

genehmigten Dissertation.

Vorsitz :	Prof. Dr. Michael Knap
Prüfer*innen der Dissertation :	1. Hon.-Prof. Dr. Gerhard Rempe
	2. Prof. Dr. Peter Fierlinger

Die Dissertation wurde am 20.12.2021 bei der Technischen Universität München eingereicht und durch die Fakultät für Physik am 07.07.2022 angenommen.

Abstract

Due to their rich internal structure and their permanent electric dipole moment polar molecules provide fascinating research opportunities, ranging from fundamental physics tests to quantum information processing and many body physics. All of these applications benefit from, or require, excellent control over the molecules' internal and external degrees of freedom. In recent years, the development of cooling techniques was a central research focus, so that nowadays deceleration, trapping and cooling of molecules can be routinely achieved, and a few selected molecules can be cooled to ultracold temperatures. As these techniques develop, and applications become broader and more ambitious, it is advantageous to explore a more diverse range of molecular species at cold and ultracold temperatures

Therefore, in the first part of this thesis we propose how to extend opto-electric Sisyphus cooling from symmetric top molecules to more diverse molecular species including diatomic radicals and linear polyatomic molecules. In addition we also consider opto-magnetic Sisyphus cooling of molecules with spin and electronic angular momentum. We found both techniques to be generally applicable to several types of molecules as they only rely on the strong interaction of the molecule's dipole or magnetic moment with an external electric or magnetic field. We provide the necessary concepts to cool an arbitrary molecule and found that molecules with degenerate or closely spaced opposite parity states in the ground state are in particular well-suited to this method. This renders symmetric top molecules as well as diatomic radicals with Λ- or Ω-doublet in the electronic ground state and linear molecules excited to a vibrational bending mode as the ideal platforms for opto-electric and opto-magnetic Sisyphus cooling. Their strong, linear interaction with an external electric or magnetic field provides ideal trapping properties and allows energy removal on the order of 1K per scattered photon. This makes opto-electric and opto-magnetic Sisyphus cooling a promising candidate to extend the scope of ultracold molecule research to more diverse species.

Due to the rapid progress in deceleration, trapping and cooling techniques, studying molecular interactions becomes increasingly important to advance the field of cold and ultracold molecule research. However, reaching sufficiently high densities to observe dipolar collisions between trapped molecules has proven to be a challenging task. In the second part of this thesis we report that by combining cryogenic buffer-gas cooling with centrifuge deceleration, we were able to confine molecular samples of sufficiently high density in our electric trap to directly observe collision-induced two-body loss. By tuning the trap offset field, we observed electric field controlled dipolar collisions and suppressed the resulting two-body losses from the trap by a factor of two. A semi-classical model showing excellent agreement with the experimental data, allowed us to identify the loss mechanism to be dipolar relaxation. In summary we were able to suppress ineleastic collisional loss without affecting thermalising elastic collisions, a prerequisite for efficient rethermalisation and potential evaporative cooling experiments.

Contents

Chapter 1

Introduction

Having full control over all internal and external degrees of freedom for a given quantum object or quantum system is one of the ultimate goals for many physics experiments. It allows fundamental understanding of the physical processes down to the quantum level and provides the opportunity to explore and exploit all the fascinating research possibilities quantum physics provides. To achieve control at this level the system or the particle of interest needs to be cooled to cold or ultracold temperatures. Five decades ago this seemed to be completely unattainable, until in 1975 Hänsch and Schawlow [1] introduced the idea that laser radiation can be utilised to cool atoms, followed by the first experimental demonstrations by Balykin et al. [2] and Phillips et al. [3] in 1985. Inspired by the fascinating research possibilities the field progressed rapidly, eventually leading to the first observation of Bose-Einstein-condensation of ^{87}Rb and Na in 1995 [4, 5], by making use of laser and evaporative cooling techniques.

The ability to cool atomic samples to ultracold temperatures opened new research areas to experimental studies, like quantum information processing [6, 7], quantum simulation [8, 9] or high precision measurements [10, 11], to name a few. The obtained results are outstanding and inspired various research groups to extend the active research from atoms to more complex quantum objects like molecules. In comparison to atoms molecules stand out due to their rich internal structure [12, 13], including electronic, vibrational and rotational states, and the fact that they can have a permanent electric dipole moment [12], allowing experimental studies beyond what is achievable with atoms. Similar to atoms, many of the envisioned applications require control over the molecule's internal and external degrees of freedom [14, 15, 16, 17]. However, the rich internal structure molecules provide, does not only open many exciting research possibilities, but also renders them hard to cool and control. Despite being challenging, the rewards for successfully achieving ultracold molecules are significant. As a result, much effort has been put into and great results have been obtained for both indirect as well as direct cooling techniques of molecules, which we will summarise in section 1.2.1 and 1.2.2, respectively.

To date only two direct cooling techniques have allowed samples of ultracold

molecules to be prepared; laser cooling [18, 19, 20] and opto-electric Siysphus cooling [21]. Laser cooling experiments are challenging, typically involving multiple repump lasers, and can only be realised for molecules with a specific electronic structure and bonding properties [22, 23, 24, 25]. In contrast opto-electric Sisyphus cooling, a technique developed by the Rempe group at MPQ, is a complementary technique that has been theoretically proposed for symmetric top molecules [26] and experimentally demonstrated for CH_3F [27] and H_2CO [21]. In chapter 2 of this thesis, we will show that opto-electric Sisyphus cooling can be extended to a larger variety of molecular species in particular to diatomic and linear triatomic radicals, and therefore extending the scope for cold and ultracold molecule research.

The advance of these cooling techniques already provides good control over the molecule's internal degrees of freedom [28, 29], even down to the quantum level [30, 31]. However an outstanding goal is the observation of a quantum degenerate gas of naturally-occurring molecules. In this respect, collisions studies become increasingly important to close the gap from cold to ultracold temperatures and form the ultracold regime to quantum degeneracy via sympathetic or evaporative cooling techniques. Of particular importance is the ability to suppress inelastic collisional loss without affecting thermalising elastic collisions. In chapter 3 we present how we suppress inelastic collisional loss from a trapped ensemble of polar symmetric top molecules by a factor of two utilising an external electric field.

1.1 Applications of cold and ultracold molecules

1.1.1 Precision Measurements

The complex internal structure of molecules provides great sensitivity to subtle effects that enable probing some of the most fundamental theories and features in physics [32, 33, 34]. This includes testing the variation of fundamental constants, e.g. the temporal variation of the proton-to-electron mass ratio [35], the measurement of the fine structure constant [36] as well as the search for dark matter [37, 38] or the electron's electric dipole moment (eEDM) [39, 32]. These experiments require precise control over the molecular states and population such that the production of cold molecule samples with high state purity is auxiliary [33]. In addition samples of slow and cold molecules have an additional merit to these high precision measurements, an increased interrogation time, that improves measurement sensitivity.

Within this section we will provide a brief overview over the search of the eEDM, whereas for a more detailed description we refer the interested reader to [40, 41]. The search for the eEDM is motivated by a fundamental question from the field of particle physics, the matter-antimatter imbalance [41]. The Standard Model of particle physics predicts the observation of an equal amount of matter and antimatter, but this stands in contrast to cosmological observations [42] and the fact that we exist. This is one of the strongest indicators that the Standard Model is incomplete. Theorists are developing several extensions to account for these issues, including

e.g. supersymmetry. The Standard Model predicts a value for the eEDM which is, to date, many orders of magnitude too low to be measured, while extensions to it predict values within reach of state-of-the-art experiments [43, 44]. Therefore, the search for the eEDM is a test for physics beyond the Standard Model, and acts as a complementary technique to the measurements looking for new supersymmetric particles with the Large Hadron Collider at CERN.

Molecules are the ideal platform for this fundamental physics test as they can be polarised easily in electric fields and due to the bonding of the atoms, the electron can feel a significantly enhanced electric field compared to the applied field, of up to 100GV/cm [45]. In addition molecules can possess states that are extremely insensitive against systematic effects [46]. The most precise upper bound for the eEDM was measured by Andreev et al in 2018 using ThO. They were able to determine an upper limit of $|d_e| < 1.1 \cdot 10^{-29}$e·cm to the dipole moment of the electron, constraining many theories beyond the Standard model to energies in range of $3-30$TeV [42]. By implementing technical improvements it is expected to increase the accuracy of the measurements even further in the near future [47, 48], into a regime where table-top AMO experiments are competing with the highest energy collider experiments.

1.1.2 Quantum Information Processing

A key ingredient for successful quantum information processing and quantum simulation is a quantum system with controllable long-ranged interactions between the individual particles which are ideally highly decoupled from environmental noise [49, 50, 51]. This allows on the one hand the exchange of quantum information between the particles and provides the possibility for scaling to larger systems, while the decoupling from the environment ensures good coherence properties [51]. Polar molecules fulfill both requirements; their long-lived rotational states have excellent coherence properties [52], while the long-ranged dipole-dipole interaction can provide the coupling between the individual particles of the system [14]. Furthermore molecules have an additional advantage; information stored in rotational states is accessible with microwave radiation, so that in total polar molecules are a very promising platform for quantum information processing experiments. We want to emphasize here that for a successful implementation of quantum information protocols excellent control over the molecules internal and external degrees of freedom are necessary such that cooling and trapping is of special importance here. In this framework Park et al. achieved an outstanding result by measuring coherence times on the order of 1s between nuclear spin states in ultracold NaK molecules [53], demonstrating the potential of polar molecules for quantum information processing purposes.

In the following we will present some selected proposals for quantum information processing with molecules but refer the interested reader to [39] for additional information. In 2002, DeMille proposed quantum computation with polar molecules that are trapped and aligned in a one-dimensional array. An electric field gradient

allows single site addressing and the dipole-dipole interaction provides the coupling between the individual quantum bits [14].

Polar molecules are also particularly well suited for hybrid quantum information systems with superconducting microwave stripline resonators [54, 55, 56]. Such a hybrid approach can combine the advantages of the different constituents, e.g. the robust control techniques and the good scaling properties of the solid state system with the good coherence properties of the molecules' rotational states [54]. For this type of system molecules are especially well suited as entanglement between the microwave resonator and the rotational states of the molecules can be achieved by the exchange of microwave photons [54].

As symmetric top molecules are the workhorse in our group, and all the experimental results presented in this thesis were obtained with CH_3F, we want to emphasise that symmetric top molecules are also promising candidates for qubits [57]. The advantage of this class of molecules is that, in contrast to diatomic molecules, they possess a linear Stark shift even at small fields. In this case, the effective dipole moment is almost unaffected by the electric field strength and the fields required for the addressing sites can be low [57]. Furthermore symmetric top molecules also allow established NMR techniques to be utilised to enhance logic gate operations [57].

1.1.3 Collision Studies

Collision studies are essential to understand the fundamental physics in molecular interactions, chemical reactions, and for the preparation of quantum degenerate gases. Consequently they are currently one of the main research areas for cold and ultracold molecule experiments.

The field of molecule-molecule collisions was pioneered using crossed-beam and merged-beam techniques [58, 59] with outstanding results like e.g. the observation of partial wave resonances in inelastic O_2–H_2 collisions [60]. Despite the great achievements, beam experiments suffer from a limited interaction time, which makes the exploitation or manipulation of the molecule-molecule interactions a challenging task. However the experimental realisation of deceleration, cooling techniques (see section 1.2) and the possibility to trap molecules has put and end to this problem. Nowadays molecules are routinely confined in optical [19], magnetic [61, 30, 62] and electric [63, 64, 65] traps with up to 60s of trapping time [65, 62], which is the perfect starting point for detailed collision and reaction studies.

In the ultracold temperature regime, there has been great success in collision experiments using molecules that have been associated from ultracold atoms. The results are summarised in various review articles [66, 67, 68] and we will only highlight a few outstanding achievements in the following. For indirectly cooled molecules, rapid trap loss has been observed due to chemical reactions [69] or due to the trapping light via an intermediate complex [70]. Furthermore, collision studies with bialkali dimers showed novel unexpected phenomena, like sticky collisions [71], the

formation of collision complexes causing significant collisional loss for non-reactive molecules like NaRb [72]. Due to the rapid progress in this research area, there is now the ability to track a chemical reaction through from the reactants to the intermediate states to the products [73]. Moreover in KRb systems, control over lossy collisions using an external electric field has allowed thermalisation to quantum degeneracy [74] and the production of a degenerate quantum gas [75].

For molecules that have been directly cooled, relatively few experiments have been able to achieve densities of trapped molecules that are required to observe collisions. One solution is to magnetically trap a dilute gas of OH molecules and use this as a target for a beam of ND_3 molecules to study collisions at 5 K [76]. Another solution is to prepare a mixture of ultracold CaF molecules and Rb atoms in a magnetic trap [77] or to trap two CaF molecules side-by-side in a pair of tweezer traps and collide particles at an individual level [28]. Here, they observe rapid loss close to the universal loss rate which is independent of internal state and magnetic field, suggesting chemical reactions or loss via complex formation in the tweezer field.

In 2017 the Rempe group at MPQ presented a unique molecular source dubbed Cryofuge, producing record high fluxes and densities of slow and cold polar molecules [78]. This allowed Wu et al. to directly observe dipolar collisions of two-dimensionally trapped CH_3F molecules by measuring collision induced loss from a quadrupole guide [78]. The first observation of collisions between three-dimensionally trapped naturally occuring molecules was performed using Zeeman-slowed oxygen molecules in a superconducting magnetic trap [62]. They were able to create high densities for molecules around 1K kinetic energy and observed collisional loss from the trap.

To advance this field, we need to progress beyond simple observation and move towards a developed understanding, as well as control over, the interactions between molecules. A first step in this direction has been made by Anderegg et al. utilising microwave radiation to suppress inelastic lossy collisions between CaF molecules trapped in optical tweezers [29]. In the framework of this thesis we demonstrate control over dipolar inelastic collisions between three-dimensionally trapped CH_3F molecules at around 0.5K temperature utilising an external electric field and suppress inelastic losses by a factor of two. These results are presented in chapter 3.

1.2 Production of cold and ultracold molecules

Many of the applications illustrated in the previous section, benefit from or even require samples of cold and ultracold molecules. As a result, the development of cooling techniques for molecules has become a central focus for molecular research. In general, one can distinguish between indirect and direct cooling techniques, which we will review in section 1.2.1 and 1.2.2, respectively. Indirect cooling produces ultracold molecules via association of ultracold atoms, while direct cooling begins with molecules and cools them from high to low temperatures.

1.2.1 Indirect cooling techniques

The starting point for molecules produced by indirect cooling methods is the preparation of a mixture of nearly quantum degenerate alkali atoms [79], typically confined in an optical dipole trap [80, 81, 82, 83]. To create polar molecules with a large enough electric dipole moment, it necessary that the molecules are associated from two different atomic species, e.g. ^{23}Na and ^{40}K, which have to be tightly bound [79] with subnanometer binding lengths [84]. This is experimentally challenging as the interatomic distance in an ultracold gas is in the μm range, such that orders of magnitude in the internuclear separation need to be overcome when converting atoms into polar molecules [84]. However, motivated by the exciting research possibilities of ultracold dipolar molecules, much effort has been put into indirect cooling techniques, such that the formation of polar molecules can now be routinely achieved by photo- or Feshbach association.

In photoassociation, a weakly bound molecular state is formed between a pair of atoms via laser excitation and with the subsequent spontaneous or stimulated emission process the molecule is transferred into a stable ground state [84]. This process allowed, for the first time, the preparation of a molecular sample in the electronic ground state with a translational temperature on the order of μK [84]. In addition, besides the production of ultracold Cs_2 [85] this method also allowed the generation of ultracold polar molecules [86, 87].

When producing molecular samples via Feshbach association an externally applied magnetic field is adiabatically swept over a Fano-Feshbach scattering resonance which can convert unbound atomic states into a short lived excited bound molecular state. Subsequently the molecules are transferred into the rovibrational ground state by stimulated Raman adiabatic passage (STIRAP) [79]. As Feshbach association is a fully coherent process extremely low temperatures and large phase space densities can be obtained [81, 82, 83, 88]. So that in 2019 De Marco et al. achieved a long-time outstanding goal, the observation of a degenerate Fermi gas of polar molecules [75]. This opened completely new and unexplored research areas like studying chemical reactions in the quantum degenerate regime or investigating degenerate molecules in an electric field.

1.2.2 Direct cooling techniques

Although the temperatures and phase space densities achieved with indirectly cooled molecules are outstanding and open great research opportunities, their production is experimentally challenging and limited to bialkali dimers. In addition, these molecules are having lots of unexpected result due to the complex nature and the collision processes occurring at the quantum level [71]. As, many of the envisioned applications, presented in section 1.1, profit from chemically diverse molecular species, there is another major research focus besides associating molecules from ultracold atoms; the cooling of naturally occurring molecules, also known as direct cooling.

Cryogenic buffergas cooling

Buffergas cooling is a frequently used technique in the field of cold and ultracold molecules [89, 90, 91] since the successful demonstration of CaH cooling by the Doyle group in 1998 [61]. One reason for this is the generality of the method as it only relies on sympathetic cooling of warm molecules with cold buffergas atoms (typically He or Ne), which are thermalised to the cell temperature. This technique can be applied to various molecular species and has been demonstrated for molecules from a gas bottle [92, 93], as well as for radicals produced by laser ablation [89, 94] or a glow source [95]. A further benefit of buffergas cooling is that both elastic and inelastic collisions contribute so that the moleules' external and internal degrees of freedom are cooled and temperatures as low as 1K can be reached. In theory, this would be a perfect starting point for collision studies or further cooling to ultracold temperatures. However, to obtain temperatures in the low K regime the molecules have to be fully thermalised with the buffergas atoms, requiring a sufficiently large density of buffer gas atoms in the cell. This in turn causes collisions between buffergas atoms and molecules in the vicinity of the exit nozzle, which is known as boosting [96]. The consequence of boosting is an acceleration of the molecules leaving the buffergas cell such that they are typically too fast to be confined in a trap, which is a prerequisite for many of the envisioned applications, introduced in section 1.1. Molecules typically exit a buffer gas source at velocities of $50 - 200$m/s. So, to fully exploit the potential of buffergas cooling efficient deceleration techniques are essential and will be covered in the next section. For further information on buffergas cooling we refer the interested reader to the review paper by Hutzler and coworkers [96].

Deceleration techniques

Trapping of molecular ensembles opens the possibility for long interaction times, which is beneficial for many of the envisioned applications introduced in section 1.1. However, as pointed out in the previous section, the mean forward velocity of molecules exiting a buffergas cell, which is typically in the range between 50ms^{-1} and 200ms^{-1}, is far beyond the trap depth of any molecular trap ($\leq 20\text{ms}^{-1}$), such that the molecular beam has to be decelerated to enable trapping and further cooling.

In 1999, for the first time, the Meijer group experimentally demonstrated Stark deceleration of neutral dipolar molecules [97] by making use of the strong interaction between an external electric field and the molecules' electric dipole moment. Depending on their quantum state molecules gain potential energy in an electric field such that a positive electric field gradient provides a potential hill which can be utilised to convert the molecules' kinetic into potential energy. However, electric fields that can be produced in a laboratory are by far too low to slow down a molecular beam exiting the buffergas cell to standstill or significantly below typical trap depths of state of the art molecule traps. For example to slow down a molecule with a dipole moment of $d = 1$D from 100m/s to 10m/s an electric field of about

850kV/cm would be required. To overcome this problem, a Stark decelerator uses a series of multiple pulsed segments, that can be switched individually and each segment provides a potential hill. The electric field of each segment is switched off when the molecule reaches the top of the potential hill [97], so that the molecule constantly loses kinetic energy while moving through the decelerator until the desired forward velocity is reached. In a more advanced version the molecules are trapped in all three-dimensions during deceleration, such that losses due to the molecules transverse motion are reduced [98]. Enabling trapping of different molecular species, including ND_3 [99] and CH_3F [100] is a ground-breaking achievement and shows the generality and capability of Stark deceleration.

Deceleration can not only be accomplished for molecules with a strong electric field interaction but also for paramagnetic molecules interacting with an external magnetic field. This is known as Zeeman slowing and here also the interaction with an external field provides a potential hill for molecules in a low-field-seeking state. Identical to Stark deceleration, multiple, individually addressable, segments provide the potential hills, necessary to slow down the molecular beam [101]. At this point we want to emphasize that both Stark and Zeeman deceleration are not dissipative, so although there is deceleration, there is no cooling. Magnetic trapping of Zeeman decelerated molecules has been accomplished for different molecular species [102, 103] and lead to the first observation of collisions between three-dimensionally trapped naturally occurring molecules [62]. A more in depth description of Stark and Zeeman deceleration can be found in these review articles [104, 105].

Until Di Rosa's proposal in 2004 [22] laser cooling and slowing of molecules seemed unachievable due to the molecules complex internal structure and the lack of cycling transitions. However, Di Rosa proposed that for a specific class of molecules with a $X^2\Sigma$-$A^2\Pi$ electronic structure and favorable vibrational branching laser cooling is feasible, opening a whole new field. This class of molecules allows to scatter $\geq 10^4$ photons, so that radiative forces can be utilised to compress the longitudinal component of the velocity distribution and slow down a molecular beam [106]. The first successful implementation of laser slowing has been demonstrated for the diatomic radical molecule SrF in 2012 [107] and in 2014 the same group demonstrated three dimensional trapping of SrF in a MOT after broadband laser slowing of a buffergas cooled molecular beam [108]. In addition deceleration of of CaF [109] and YO [106] down to the capture velocity of a MOT has been demonstrated. However, laser slowing has a major disadvantage as it suffers from losses due to the divergence of the molecular beam in combination with transverse heating [110]. Thus Fitch and coworkers proposed a method dubbed Zeeman-Sisyphus deceleration which makes use of optical pumping and a static magnetic field to decelerate a transversely guided molecular beam [110, 111].

All techniques shown in this section are great tools to decelerate molecular beams, nevertheless there are also drawbacks with each technique. Both Zeeman and Stark deceleration can only be operated with a pulsed source. This is not a problem for a molecular source, that works in pulsed-mode, like laser ablation. However for any

continuously working source, like the buffergas cell presented in chapter 3 of this thesis, the duty cycle of Stark and Zeeman deceleration and therefore the efficiency are low. In contrast, laser slowing experiments suffer from losses in the transverse direction and are only applicable to molecules which allow cycling of $\geq 10^4$ photons.

To help solve this problem, our group developed a centrifuge decelerator for molecules [112]. This provides continuous deceleration that is applicable to any electrically-guidable molecule with suitable dipole-to-mass ratio, independent of branching ratios or rotational closure [112]. In contrast to Stark deceleration, the interaction between the molecule's electric dipole moment and an externally applied electric field is not utilised to convert kinetic into potential energy, instead it provides transversal confinement during the deceleration process. For centrifuge deceleration the potential hill is provided by the centrifugal potential as the molecules are moving on a rotating disc from the periphery to the centre of the disc and thereby lose kinetic energy [112]. The working principle of the centrifuge is general and robust allowing for a wide range of molecular species to be decelerated, including CH_3F, ND_3, CH_3OH, as well as large molecules like CF_3CCH and C_3H_7OH [78]. As the centrifuge decelerator allows continuous slowing it works particularly well with a continuously operated buffergas cell, a combination we call the Cryofuge. As demonstrated in 2017 [78], the input to output efficiency of the cryofuge is 20% and a record high molecule flux of $> 1 \cdot 10^{10}$ s^{-1} at velocities below 20ms^{-1} can be obtained. These huge fluxes allowed for the observation of cold dipolar collision directly in a quadrupole guide [78, 113]. Furthermore by adding an electric trap to our system we were able to confine $> 1 \cdot 10^7$ molecules after deceleration of a buffergas cooled molecular beam with the centrifuge [114]. These high densities of trapped polar molecules enabled the collision studies presented in chapter 3.

Cooling to ultracold temperatures

To date there are two methods to directly cool molecules to ultracold temperatures; laser cooling and opto-electric Sisyphus cooling. For both techniques, compression of the phase space density is achieved by spontaneous emission. This creates irreversibility and removes entropy from the system, a prerequisite for cooling.

Laser cooling of naturally occurring molecules was first proposed by Di Rosa in 2004 [22] and identical to laser cooling of atoms one makes use of photon recoil to cool the molecular sample. However the momentum transfer of a single photon is tiny thus $\geq 10^4$ photons need to be scattered to cool an ensemble of cold molecules to ultracold temperatures. For molecules this is a challenging task due to their complex internal structure, including electronic, vibrational and rotational states. These states significantly differ in their spontaneous decay rates where electronically excited states have a decay rate in the MHz range [115] which is orders of magnitude larger than the Hz decay rates of vibrational or rotational levels [26, 116]. To scatter 10^4 photons the only practical choice for the excited state is an electronic level to minimise loss during cooling. However, since there are no strict selection rules for the

vibrational quantum number in an electronic transition only a few selected molecules are suited for laser cooling [22]. These are typically molecular radicals with highly diagonal Franck-Condon factors (FCF), which is a measure for the overlap of the vibrational wavefunction of the ground and the excited state, such that by adding vibrational repump lasers a vibrational closure of about 99.99% can be achieved. Although direct laser cooling of molecules was theoretically already proposed back in 2004 it took six years for the first experimental demonstration of one-dimensional laser cooling in 2010 by Shuman and coworkers [117]. The reason for this is that laser cooling experiments are very challenging and despite highly diagonal FCF, typically several repump lasers are required to scatter $\geq 10^4$ photons necessary for cooling.

After the first experimental demonstration of laser cooling of molecules in 2010 [117] the field progressed rapidly, such that in 2014 Barry et al. were able, for the first time, to confine molecules in in a MOT [108] and in 2016 the first sub mK samples of laser cooled naturally occurring molecules have been observed for SrF [18, 118]. Different molecular species have been confined in a MOT [108, 119], where Anderegg et al. trapped $1 \cdot 10^5$ CaF radicals at a temperature of 340μK [120]. By cooling CaF radicals to 5μK the lowest temperature of directly cooled molecules has been observed in 2018 by the Doyle group [121] and shortly after similar results were obtained in the group of Tarbutt [20] and Ye [122]. The recent demonstration of confining laser cooled molecules in magnetic [123, 30] and optical dipole traps [19] opens possibilities to reduce the temperatures of the molecular samples further and approach quantum degeneracy. Magnetic traps are perfectly suited for the implementation of sympathetic cooling techniques, whereas optical dipole traps provide the possibility to further laser cool the trapped ensemble and potentially reach quantum degeneracy [19]. In this respect, recent results from atomic physics are particularly interesting as Bose-Einstein condensation has been reached for optically trapped atoms by means of laser cooling without the necessity of evaporative cooling [124, 125].

Inspired by the research opportunities of polyatomic species, the area of active research has extended from laser cooling of diatomic radicals to more complex, polyatomic molecules. Transverse cooling has been observed for the triatomic linear molecules SrOH [126] and YbOH [127] as well as for the symmetric top molecule $CaOCH_3$ [128]. Furthermore a one dimensional MOT has been established for CaOH in 2020 by Baum and coworkers [129].

In contrast to these first proof of principle experiments, opto-electric Sisyphus cooling allowed the preparation of three-dimensionally cooled samples of polyatomic molecules in an electric trap. In 2012 Zeppenfeld et al. demonstrated cooling of about 10^6 CH_3F molecules to 29mK [27] and in 2016 Prehn and coworkers prepared $3 \cdot 10^5$ H_2CO molecules at a temperature of 420μK [21]. This is still the largest sample of any ultracold molecule that has been prepared so far.

In the following we will only provide a very brief overview of opto-electric Sisyphus cooling as a detailed theoretical description is provided in chapter 2 of this

thesis. Opto-electric Sisyphus cooling was first proposed in 2009 by Zeppenfeld et al. [26]. It relies on the strong interaction of an external electric field with the electric dipole moment of a polar molecule. In combination with optical pumping this allows to cool molecule samples from around 1K to ultracold temperatures by only scattering a few dozen photons [21]. Opto-electric Sisyphus cooling is a complementary technique to laser cooling as it allows preparation of ultracold samples of closed-shell symmetric top molecules; CH_3F and H_2CO, that cannot be laser cooled. For example H_2CO has very pure FCFs [130] and is likely to dissociate under electronic excitation [131]. However, in contrast to laser cooling this is not a problem for opto-electric Sisyphus cooling as a vibrational state can be used for optical pumping. This is possible due to the large energy removal per scattered photon of up to $k_B \times 1\text{K}$ in opto-electric Sisyphus cooling, thereby compensating the slow decay rate of a vibrational state ($\sim$Hz).

In the framework of this thesis we show how to extend opto-electric Sisyphus cooling to diatomic and linear polyatomic radicals, enabling three dimensional cooling of molecules like CaOH, which are confined in a trapping potential, to ultracold temperatures. In addition we also introduce opto-magnetic Sisyphus cooling in chapter 2, which is in particular suited for molecules with electronic and spin angular momentum. In total the work presented in chapter 2 of this thesis opens the possibility to extend the scope of cold and ultracold molecular research to more diverse species.

1.3 About this thesis

To realise all the fascinating research possibilities introduced in section 1.1, the ability to cool a broad range of different molecular species to cold and ultracold temperatures is essential. However, to date laser cooling of molecules to sub mK temperatures in all three spacial dimensions is limited to a few selected diatomic radicals with suitable cooling properties, as $\geq 10^4$ photons have to be scattered. Similarly, preparing samples of ultracold molecules by photo- and Feshbach association of ultracold atoms is restricted to bialkali dimers. However, as introduced in section 1.2.2, there is a third technique to cool molecules to ultracold temperatures; opto-electric Sisyphus cooling. In chapter 2 we show that opto-electric, as well as it's magnetic counter part, opto-magnetic Sisyphus cooling, are versatile techniques that can be used to prepare a large variety of different molecular species at cold or ultracold temperatures. We provide a general plan how to apply this technique to any molecule with suitable cooling properties. We find that molecules with degenerate or closely spaced opposite parity levels in the ground state are particularly well-suited due to their strong linear field response. This interaction allows for efficient trapping and cooling - with kinetic energy of several 100mK removed per scattering event. Thus, as depicted in chapter 2, promising candidates for opto-electric or opto-magnetic Sisyphus cooling are symmetric top molecules, diatomic radicals with

Λ- or Ω-doubling in the electronic ground state, as well as linear triatomic molecules, in an excited vibrational bending mode. So far opto-electric Sisyphus cooling has been demonstrated for the symmetric and slightly asymmetric top molecules CH_3F [27] and H_2CO [21] using a vibrational excited state with a comparably slow spontaneous decay rate on the order of 100Hz. In this thesis we show how to utilise an electronic excited state with decay rates on the order of MHz for opto-electric and opto-magnetic Sisyphus cooling to achieve fast cooling and thereby minimise trap losses. We conclude chapter 2 by exemplary illustrating an example scheme for the diatomic radical CH applying the concepts introduced throughout this chapter.

An outstanding goal in the cold molecule community is the preparation of a quantum degenerate gas of naturally occuring molecules. To achieve this, collisions between molecules become increasingly important to bridge the gap from ultracold to quantum degeneracy via sympathetic or evaporative cooling techniques. A key requirement for both techniques is the suppression of inleastic collisions that cause losses from the trap without altering thermalising elastic collisions. Motivated by these exciting research avenues, in chapter 3 of this thesis we study electric field controlled dipolar collisions between cold symmetric top molecules in a microstructured electric trap. Using a semi-classical model, we show excellent agreement with the experimental data and we are able to attribute the measured collisional loss to dipolar relaxation. We utilise an external electric field to suppress the associated inelastic collisional loss of the trapped CH_3F molecules by a factor of two without affecting thermalising elastic collisions. Therefore, these collision studies provide valuable information about interactions between the molecules and insights to eventually realise efficient rethermalisation of naturally occurring trapped dipolar molecules.

We conclude this thesis with chapter 4, giving an outlook to more advanced collision experiments and the implementation of opto-electric Sisyphus cooling of diatomic or linear polyatomic radicals with our experimental setup.

Chapter 2

Extending opto-electric and opto-magnetic Sisyphus cooling to diatomic and polyatomic radical molecules

In this chapter we propose how to extend opto-electric Sisyphus cooling, as well as it's magnetic counterpart opto-magnetic Sisyphus cooling, to more diverse species including diatomic radicals and linear triatomic molecules. In addition we also propose how to utilise an electronic excited state for these molecules and benefit from its large spontaneous decay rate. We start this chapter with a brief review of Sisyphus cooling techniques in section 2.1 and put opto-electric and opto-magnetic Sisyphus cooling into context. Subsequently we provide a compact introduction of the relevant theoretical concepts of symmetric top molecules, diatomic radicals and linear triatomic molecules, neccessary to apply opto-electric as well as opto-magnetic Sisyphus cooling to these molecules in section 2.2. After depicting the basic concepts and requirements for a successful implementation of opto-electric or opto-magnetic Sisyphus cooling for an arbitrary molecule in 2.3, we show how to apply these concepts to diatomic radicals, symmetric top and linear triatomic molecules in section 2.4. In the last part of this chapter, 2.5, we present an example scheme for opto-electric Sisyphus cooling of the diatomic radical CH, utilising an electronic excited state.

2.1 Sisyphus cooling techniques

Sisyphus cooling is probably mostly associated with the work of Dalibard and Cohen-Tannoudji [132] – polarisation gradient cooling of atoms. This technique allowed atoms to be cooled below the Doppler limit, down to the recoil limit and was awarded with the Nobel prize in 1997. However before introducing the concept of polarisation

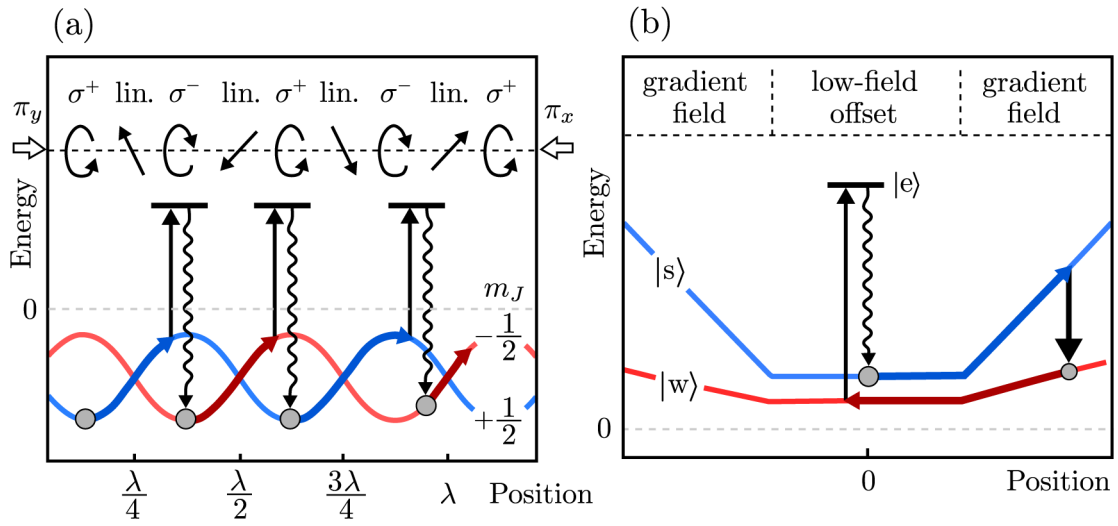

Figure 2.1: *Schematic illustration of (a) polarisation gradient cooling and (b) opto-electric Sisyphus cooling*

gradient cooling in more detail we can take one step back and briefly look at the concepts of Sisyphus cooling in general. Sisyphus cooling rests upon two ingredients; a spatially-varying state-dependent energy shift and spontaneous emission. The first part sets the amount of energy extracted, the second is required to remove entropy from the system. In the standard example, Dalibard and Cohen-Tannoudji utilise two counter-propagating laser beams with identical frequency and intensity but orthogonal linear polarisation to create a spatial modulation of the energy of the magnetic sublevels of the atom [132], as depicted in Figure 2.1 (a) for a $J = 1/2 \rightarrow J' = 3/2$ transition. The two laser beams create a standing wave with spatially varying polarisation that changes from σ^+ to σ^- every quarter of a wavelength and vice versa, with the polarisation in between being elliptical or linear [132]. The spatially varying polarisation does not only lift the degeneracy of the atom's magnetic sublevels, due to a polarisation-dependent light shift, but moreover also modulates the optical excitation probability. If the light field is red-detuned from the transition, $J = 1/2 \rightarrow J' = 3/2$ in Figure 2.1 (a), optical pumping transfers population from the higher to the lower lying m_J-level. For example, as illustrated in Figure 2.1 (a), σ^- polarised light pumps population at the top of the potential hill out of the $m_J = +1/2$-level into the $m_J = -1/2$-level, whereas σ^+ polarised light pumps population from $m_J = -1/2$ to $m_J = +1/2$. Therefore with a red-detuned light field the atom moves on average uphill more often than downhill such that kinetic energy is removed from the system. The amount of energy that can be removed with one spontaneous emission event is given by the light shift, which depends on the experimental parameters but typically does not exceed $k_B \times 1\text{mK}$. Nevertheless efficient cooling is achieved due to the fast photon cycling rate that allows many cooling cycles while the particle moves through the potential. Besides applying Sisyphus cooling techniques to atoms, Zeppenfeld et. al. proposed in

2009 [26] and demonstrated in 2012 [27] opto-electric Sisyphus cooling of polar symmetric top molecules. In contrast to producing the Sisyphus potential via light shifts in opto-electric Sisyphus cooling one makes use of the molecules' permanent electric dipole moment and its strong interaction with an external electric field. The potential is illustrated in Figure 2.1 (b) with a homogeneous low-field region in the centre and a region of steep gradient field towards the edge. If the gradient surrounds the low-field region in three dimensions it creates a trap. With experimentally realisable electric fields of up to 100kV/cm [133] and depending on the molecular properties, molecules with kinetic energies up to $E_{\text{kin}} = k_B \times 1\text{K}$ [114] can be confined.

The ground state in the example scheme, depicted in Figure 2.1 (b), consists of two states, $|s\rangle$ and $|w\rangle$ with strong and weak field interaction, respectively. Starting in $|s\rangle$, the particle climbs up a potential hill when moving from the centre region towards the edge of the potential and therefore loses kinetic energy. In the high field region, population is transferred from $|s\rangle$ to $|w\rangle$ and the molecule moves back to the centre region, where it gets optically pumped into the excited state $|e\rangle$. Spontaneous emission from $|e\rangle$ to $|s\rangle$ creates, not only a closed, unidirectional cycle, but also removes entropy from the system. The difference in the dipole moment of the $|s\rangle$ and the $|w\rangle$ state, which can be typically up to 1D, determines the amount of kinetic energy that can be removed in a single cycle. For a gradient field up to 100kV/cm, $k_B \times 1.6\text{K}$ can be removed with a single scattering event. This means that opto-electric Sisyphus cooling will remove much of the kinetic energy of the trapped particles with a single scattered photon. Consequently, the particles do not have sufficient kinetic energy to reach the resonance of the driving field when climbing up the potential hill again. Therefore, to continuously reduce the temperature of the molecular sample the frequency of the radiation driving the $|s\rangle$ to $|w\rangle$ transition needs to be adjusted according to the molecules' kinetic energy. Neglecting possible technical limitations the temperature of the molecular sample can be reduced down to the photon recoil limit using opto-electric Sisyphus cooling.

Opto-electric Sisyphus cooling allowed the temperature of $\sim 10^6$ CH_3F molecules to be reduced from 390mK to 29mK and increased the phase space density by a factor of 29 [27]. Furthermore in 2016 Prehn et al. produced a record high number of ultracold molecules, $3 \cdot 10^5$ H_2CO molecules at a temperature of 420μK, by scattering only ~ 20 photons [21]. This makes opto-electric Sisyphus cooling a great complimentary technique to direct laser cooling of molecules, as it does not require highly-closed transitions and fast decay rates. With this technique, it is possible to create an ensemble of ultracold molecules that are not amenable with laser cooling like the polyatomic molecule H_2CO. This molecule would be basically impossible to be laser cooled, due to a very unfavorable Franck-Condon factor [130] and a large probability for dissociation on electronic excitation [131].

Besides opto-electric Sisyphus cooling other Sisyphus type cooling techniques have been proposed and theoretically investigated for cold molecule experiments, including ac-Stark [134], dc-Stark [135] or Zeeman [110] slowing techniques in combi-

nation with optical pumping. Furthermore the magnetic counterpart of opto-electric Sisyphus, opto-magnetic Sisyphus cooling, has been proposed [115, 116]. The underlying concepts of both techniques are very similar but instead of utilising the interaction between an external electric field and the molecules dipole moment in opto-magnetic Sisyphus cooling one makes use of the magnetic moment interacting with an external magnetic field. Similar to opto-electric Sisyphus cooling large energy removal is possible with a single spontaneous emission event. Assuming a magnetic moment of μ_B and a magnetic field of $B = 1\text{T}$ then $k_B \times 0.6\text{K}$ can be extracted with only one scattered photon.

2.2 Types of molecules and theoretical foundations

Opto-electric and opto-magnetic Sisyphus cooling are versatile and generic techniques that can be applied to various molecular species. Opto-electric Siysphus cooling works particularly well for three categories of molecules which all have a strong linear electric field response in common. The first group is closed shell symmetric top molecules, where opto-electric Sisyphus cooling has already been experimentally demonstrated with great success [27, 21]. Furthermore linear triatomic molecules in an excited vibrational bending mode and diatomic radicals with Λ-doubling in the ground state are also perfectly suited. Finally diatomic radicals with Λ-doubling in the ground state are also the ideal candidates to realise opto-magnetic Sisyphus cooling.

In this section we will present the relevant theoretical foundations for these three groups of molecules, including their rotational energy structure as well as brief description of their interaction with an external electric or magnetic field.

2.2.1 Closed-shell symmetric top molecules

First, we consider closed shell polar symmetric top molecules, consisting of four or more atoms with a permanent electric dipole moment oriented along the principal axis of the molecule and an at least three-fold rotational symmetry about this axis. Example molecules are NH_3 or CH_3F, that has already been successfully cooled from 390mK down to 29mK utilising opto-electric Sisyphus cooling [27]. The rotational states of a symmetric top molecule are described by three quantum numbers, that are graphically illustrated in Figure 2.2 (a), the total angular momentum J, its projection onto the molecule's symmetry axis K and the projection of J onto an external field axis, described by the quantum number M [12]. Since there is no angular momentum in the ground state for closed-shell molecules J can take any positive integer value, whereas K and M can take $(2J+1)$ values for each J in range of $-J \leq K \leq J$ and $-J \leq M \leq J$. Without applying an external electric field the

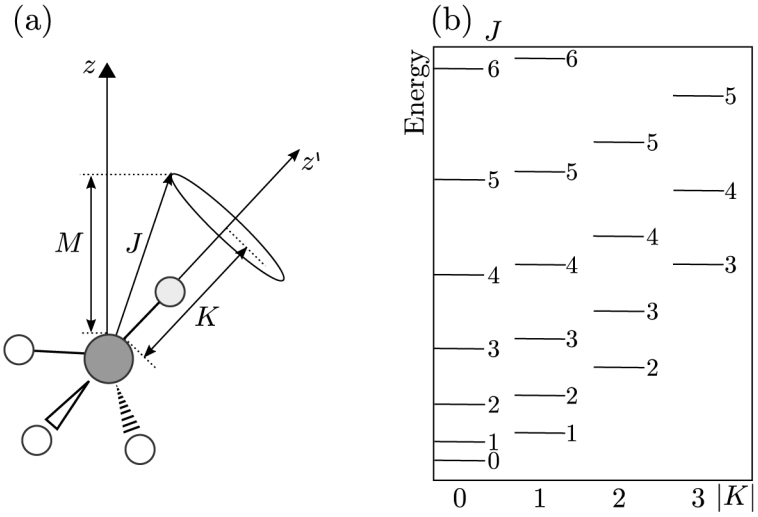

Figure 2.2: *(a) Schematic illustration of the rotational quantum numbers of a closed-shell symmetric top molecules, where z', defines the molecular symmetry axis and z the external field axis. (b) Energy level structure of a prolate symmetric top molecule.*

energy of a rotational state for a prolate symmetric top molecule is given by [12]

$$E_{\text{rot}} = BJ(J+1) + (A-B)K^2, \tag{2.1}$$

with rotational constants A and B, resulting in a rotational energy level structure as depicted in Figure 2.2 (b).

We include the interaction of the permanent electric dipole moment $\boldsymbol{d} = d\boldsymbol{e_{z'}}$ of a symmetric top molecule with an external electric field $\boldsymbol{E} = E\boldsymbol{e_z}$ using the Stark Hamiltonian

$$\hat{H}_s = -\hat{\boldsymbol{d}} \cdot \boldsymbol{E}, \tag{2.2}$$

which mixes states of opposite parity. Due to the cylindrical symmetry and the associated $\pm|K|$ degeneracy in symmetric top molecules there is an energetically degenerate pair of opposite parity states for each $|K| > 0$, that can be written as $|\Psi_\pm\rangle = 1/\sqrt{2}(|J,|K|,M\rangle \pm |J,-|K|,M\rangle)$ [136]. This gives rise to a linear electric field response and the first order Stark shift can be expressed as, [137]

$$\Delta E_{JKM} = -dE\frac{KM}{J(J+1)}. \tag{2.3}$$

The applied electric field lifts the $(2J+1)$-degeneracy of the M levels, however due to the cylindrical symmetry of the molecules each rotational state with $|K| > 0$ remains two-fold degenerate with $\pm|K|$ [12].

In the framework of this thesis we use the convention that $K = -|K|$, such that the sign of M determines the character of the electric field response. States with $M < 0$ are high-field-seeking and states with $M > 0$ are low-field-seeking.

Furthermore in the presence of an external electric field the parity states $|\Psi_{\pm}\rangle$ are mixed such that the rotational $|J, K, M\rangle$ states asymptotically become the new eigenstates of the system [136]. We want to note here that a more detailed theoretical description of the Stark effect can be found in section 3.2.6 of this thesis.

2.2.2 Diatomic radicals

In the following we will give a short theoretical introduction to the quantum numbers, energy level-structures as well as magnetic and electric field interactions of diatomic radicals, with a single unpaired electron. We will keep this section brief and only consider theoretical concepts required to apply opto-electric and opto-magnetic Sisyphus cooling to radical species. In contrast to closed shell symmetric top molecules, introduced in the previous section, these diatomic radicals possess electronic angular momentum. This increases the complexity of the theoretical description due to features like Λ-doubling [13], spin-orbit [138] and spin-rotation interaction [139]. The molecular radicals we consider here are theoretically [13, 138, 139, 140] and experimentally [141, 142, 143] well studied as the vast majority of laser coolable molecules, like CaF, SrF or YO fall in this category. However we will extend the scope beyond laser coolable molecules and will in particular focus on radicals with Λ- or Ω-doubling in the ground state like OH and CH, which are well suited for opto-electric or opto-magnetic Sisyphus cooling.

Angular momentum coupling – Hund's cases

The subsequent introduction of the basic theoretical concepts for diatomic radicals follows the description in [13]. In addition to the rotational angular momentum of the nuclei R, diatomic radicals also possess electronic orbital angular momentum L and electronic spin S. Their projections onto the internuclear axis are labelled as Λ and Σ and their sum is denoted by $\Omega = \Lambda + \Sigma$. This allows us to introduce the state notation for diatomic radicals, which is given by ${}^{2S+1}\Lambda_{\Omega}$, where $|\Lambda| = 0, 1, 2, ...$ creates electronic states with $\Sigma, \Pi, \Delta, ...$ character respectively. We note here that due to the two possible senses of rotation for the orbital angular momentum and the spin around the internuclear axis there are also two possible values for their projections $\pm\Lambda$ and $\pm\Sigma$. As usual, the projection of the total angular momentum J onto an external field axis is given by the quantum number M_J.

The coupling of all these different angular momenta makes a theoretical description of diatomic radicals a challenging task. To allow a more intuitive approach and to reduce the complexity, Hund introduced a classification of the different coupling schemes into five idealised groups, the Hund's cases [140], depending on the coupling strength of the individual angular momenta in comparison to the electrostatic interaction, the spin-orbit interaction and the rotational energy. For the purpose of this thesis the Hund's cases (a) and (b) or intermediate coupling schemes are most important. The coupling scheme of Hund's case (a) is illustrated in Figure

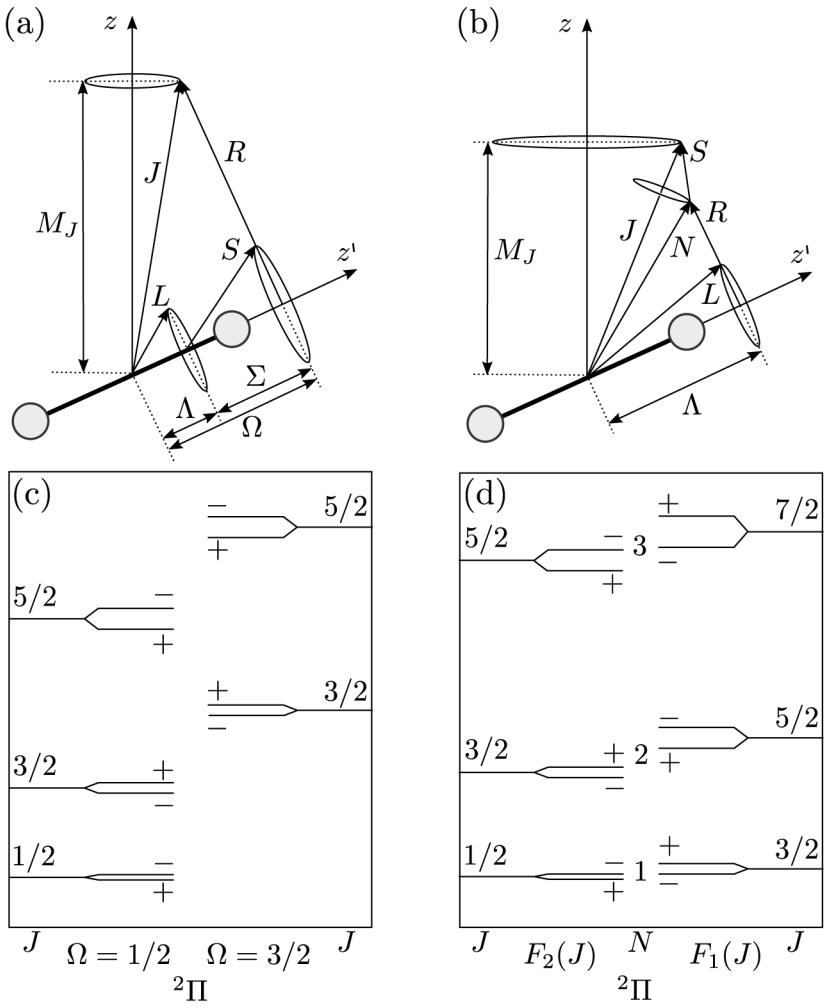

Figure 2.3: *(a) and (b) Illustration of Hunds's coupling case (a) and (b) for a diatomic radical, respectively. The corresponding energy level diagrams for a* $^2\Pi$ *radical molecule are illustrated in (c) and (d).*

2.3 (a) and characterised by the fact that the electrostatic interaction is dominant, such that L is coupled strongly to the internuclear axis. In addition the spin-orbit interaction is larger than the rotational energy such that S is strongly coupled to L and thus S is also coupled to the internuclear axis. We obtain the total angular momentum J by coupling Ω to R, so that $J \geq \Omega$. Since R is perpendicular to Ω, the projection of J onto the internuclear axis is given by Ω. In Hund's coupling case (a) both Λ and Σ and consequently also Ω are good quantum numbers such that the basis states are given by $|\Lambda, S, \Sigma, J, \Omega, M_J\rangle$. The energy level structure of a $^2\Pi$ Hund's case (a) molecule is depicted in Figure 2.3 (c). The large spin-orbit interaction results in (2S+1) fine structure components, characterised by the quantum number Ω, where each Ω has it's own ladder of rotational states with relative

energy $BJ(J+1)$, where B is the rotational constant. As can be seen in Figure 2.3 (c) each J-state is split into a positive and negative parity component of a so called Λ- or Ω-doublet. A theoretical derivation of Λ-doubling is quite challenging and beyond the scope of this thesis, so we want to refer the interested reader to [13] for a detailed description. In broad terms, the two opposite senses of rotation for Λ are energetically degenerate for a non-rotating molecule, however rotation and spin-orbit interaction lift this degeneracy to create a pair of closely spaced opposite parity states, the Λ-doublets. The parity eigenstates can be expressed as

$$|\epsilon, J, |\Omega|, M_J\rangle = \frac{1}{\sqrt{2}}\big(|+|\Lambda|, S, +|\Sigma|, J, +|\Omega|, M_J\rangle + \epsilon(-1)^{(J-S)} |-|\Lambda|, S, -|\Sigma|, J, -|\Omega|, M_J\rangle \big), \tag{2.4}$$

where the parity of the state is given by $\epsilon = \pm 1$.

The coupling scheme for Hund's case (b) is depicted in Figure 2.3 (b). Identical to Hund's case (a) the electrostatic interaction is dominant and couples L to the internuclear axis, however the coupling of L and S is weak compared to the rotational energy or not existent e.g. for molecules with $\Lambda = 0$. Therefore S is no longer coupled to the internuclear axis and in contrast to Λ, Σ is no longer well defined. The rotational quantum number R can take any integer value $R \geq 0$, so that by coupling Λ to R we obtain $N \geq \Lambda$. The total angular momentum J is then given by the sum of the angular momentum N and the spin S, so that the basis states can be written as $|\Lambda S N J M_J\rangle$. Figure 2.3 (d) shows the energy level structure of a $^2\Pi$ Hund's case (b) molecule, where the relative energy of the rotational states is given by $BN(N+1)$. The spin-rotation interaction splits the rotational levels into $(2S+1)$ fine structure features, such that for a $^2\Pi$ molecule with $S = 1/2$ we get $F_1(J)$ for $J = N + 1/2$ and $F_2(J)$ for $J = N - 1/2$, as illustrated in Figure 2.3 (d). Furthermore, in this example $|\Lambda| > 0$, where each J-state is split into two Λ-doublet components of opposite parity and the parity conserved basis states are described by

$$|\epsilon, N, |\Lambda|, J, M_J\rangle = \frac{1}{\sqrt{2}}\big(|N, +|\Lambda|, S, J, M_J\rangle + \epsilon(-1)^{(J-S)} |N, -|\Lambda|, S, J, M_J\rangle \big), \tag{2.5}$$

where again the parity of the state is given by $\epsilon = \pm 1$. Although not discussed in this thesis in principle opto-electric and opto-magnetic Sisyphus cooling can also be applied to molecules categorised by Hund's case (c), with a quite similar behaviour as Hund's case (a) molecules. However, these molecules are rather unusual and are currently not studied in the field cold and ultracold molecule research.

Stark and Zeeman interaction of radical molecules

As emphasised in section 2.1 a strong linear field response of the particles is important for trapping as well as for cooling with opto-electric or opto-magnetic Sisyphus

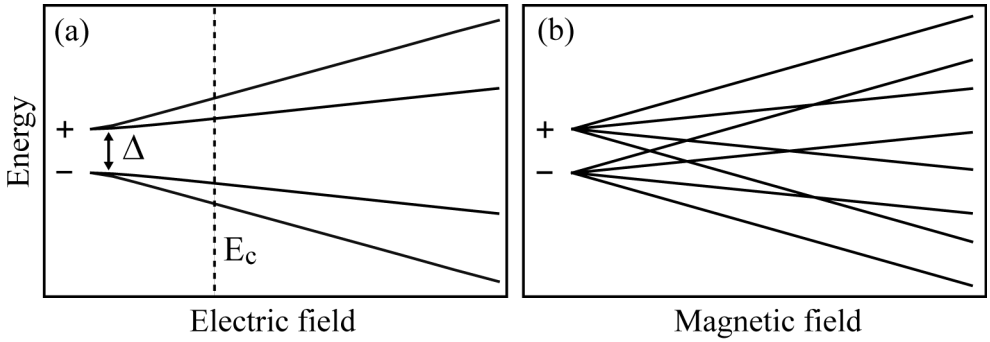

Figure 2.4: *(a) Schematic illustration of the electric field response of a molecule in a $J = 1/2$ state with inversion splitting Δ. The inversion splitting can be caused by Λ- or Ω-doubling and in the case of a linear triatomic molecule also by ℓ-doubling. E_c marks the critical field where the Stark shift starts to become linear. (b) Zeeman interaction of a diatomic radical with inversion doubling in the $J = 1/2$ state.*

cooling. This makes radicals with Λ- or Ω-doubling in the ground state promising candidates for opto-electric Sisyphus cooling due to their closely-spaced opposite parity states, which can be mixed by an external electric field, as illustrated in Figure 2.4 (a). For low electric fields the opposite parity states are only weakly mixed and the electric field response is quadratic. However, as the electric field increases, the opposite-parity states become strongly mixed and the Stark shift becomes linear. The change from quadratic to linear field response occurs at $E_c = \Delta/2d$ [144], with Δ being the splitting of the inversion-doublet and d the molecule's dipole moment. In this situation the parity eigenstates given by Equation 2.4 and 2.5 are no longer eigenfunctions, instead basis states with a well-defined signed value of Ω and Λ in Hund's case (a), given by $|J, \Omega, M_J\rangle$, and states with a signed value of Λ for Hund's case (b), given by $|N, \Lambda, J, M_J\rangle$, provide the most accurate description. These states are identical to the symmetric top basis states in the presence of a large electric field, when e.g. replacing Ω by K for Hund's case (a). The first order Stark shift is then given analogous to equation 2.3 by

$$\Delta E_{J\Omega M_J} = -dE\frac{\Omega M_J}{J(J+1)}. \tag{2.6}$$

Throughout this thesis we use the convention that $\Omega = -|\Omega|$, such that states with $M_J > 0$ are low-field seeking. Radicals can not only have large Stark shifts but due to their electronic and spin angular momentum L and S , they can also show strong Zeeman interactions, where the molecule's magnetic moment $\boldsymbol{\mu}$ interacts with an external magnetic field $\boldsymbol{B} = B\boldsymbol{e_z}$, given by the Zeeman Hamiltonian

$$\hat{H}_z = -\boldsymbol{\mu} \cdot \boldsymbol{B}. \tag{2.7}$$

Here $\boldsymbol{\mu} = \mu\hat{\boldsymbol{\sigma}}$, where $\hat{\boldsymbol{\sigma}}$ describes the direction of the average magnetic moment of the molecular state and μ its magnitude. In contrast to the Stark Hamiltonian,

the Zeeman interaction mixes states of identical parity such that inversion-doubling does not influence the molecule's magnetic field interaction and we observe a linear magnetic field response also for small values of B, as schematically depicted in Figure 2.4 (b). The Zeeman shift for a pure Hund's case (a) molecule can be expressed as

$$\Delta E_{J\Omega M_J} = \mu_B B(g_L\Lambda + g_S\Sigma)\frac{\Omega M_J}{J(J+1)}, \tag{2.8}$$

where μ_B is the Bohr magneton and the Landé g-factors associated with L and S are $g_L \approx 1$ and $g_s \approx 2$ respectively.

2.2.3 Linear molecules

In this section we will introduce the basic theoretical concepts for the third group of molecules, which is well suited for opto-electric Sisyphus cooling, linear molecules. They are characterised by a bond angle of 180° between the individual atoms and can occur as closed shell molecules, like OCS, HCN and CO_2 or radicals, like CaOH or SrOH. Although linear molecules also exist with more than three atoms, within this thesis we will focus on linear triatomic molecules.

In the absence of vibrational excitations, the electronic spectra of linear triatomic radicals are essentially identical to the spectra of diatomic radicals, including Λ-doubling, spin-orbit or spin-rotation interaction. However diatomic and linear triatomic molecules differ in their vibrational structure, since linear triatomic molecules can have three vibrational modes (v_1, v_2, v_3). The vibrational modes v_1 and v_3 are linear modes, whereas v_2 is a bending mode, that is doubly degenerate, due to the molecule being able to bend either in x'- or y'-direction perpendicular to the symmetry axis z' [12]. A 90° phase shift between the two bending modes results in a circular motion of the nuclei around the molecular symmetry axis, giving rise to the vibrational angular momentum G [145], depicted in Figure 2.5 (a). The projection of G onto the symmetry axis z' has two possible senses of rotation and is labelled by the quantum number ℓ [145], that is usually added to the notation of the vibrational bending mode as $v_2^{|\ell|}$. Possible values for ℓ are $\ell = v_2, v_2 - 2, ..., -v_2$ [146]. Figure 2.5 (a) illustrates the coupling scheme of a linear triatomic Hund's case (b) molecule. Adding the projections of L and G onto the molecular symmetry axis gives the quantum number $K = \Lambda + \ell$ [145], which we couple to the rotational angular momentum R and to the spin S to obtain the total angular momentum J. With this we can define the basis states of a linear triatomic Hund's case (b) molecule as $|\ell\Lambda SNJM_J\rangle$. In addition we can also introduce the state notation, where K is used to classify the vibronic state of the molecule [147], identical to Λ for the electronic state of a diatomic radical (see section 2.2.2), such that $|K| = 0, 1, 2, ...$ corresponds to a $\Sigma, \Pi, \Delta, ...$ state.

Linear triatomic molecules with Λ- or Ω-doubling in the ground state are, identical to diatomic radicals, perfectly suited for opto-electric or opto-magnetic Sisyphus cooling. However the additional atom provides new degrees of freedom that can

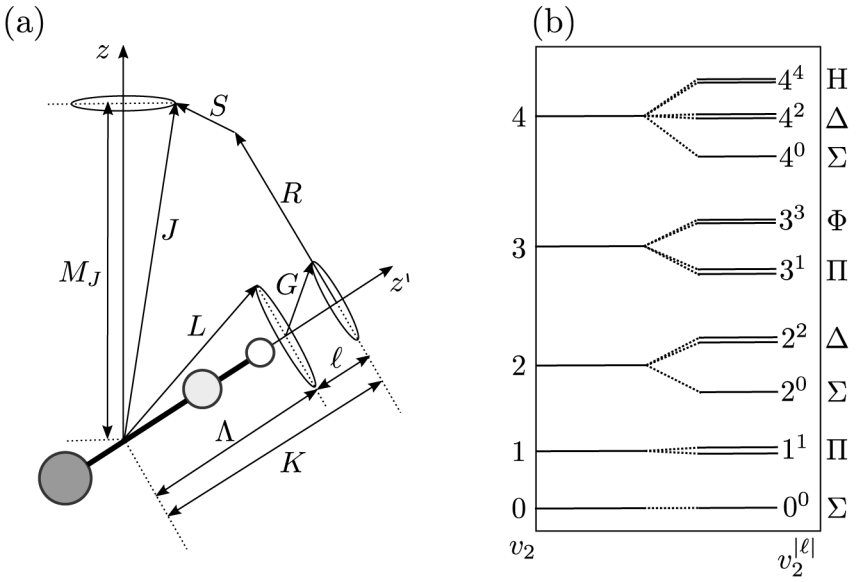

Figure 2.5: *(a) Hund's case (b) coupling scheme for a linear triatomic radical. (b) Vibrational energy level structure for the $v_2^{|l|}$-vibrational mode of a triatomic radical with Σ ground state.*

be exploited if the electronic ground state of the molecule is not suited for opto-electric Sisyphus cooling, e.g. if $\Lambda = 0$. By exciting the molecule to a vibrational bending mode with $\ell > 0$ we can create a ground state with that is well suited for opto-electric Sisyphus cooling. Here, similar to diatomic molecules with $\Lambda > 0$, the $\pm|\ell|$ degeneracy is lifted for a rotating molecule [12], resulting in a pair of closely spaced opposite parity states. Their maximum separation occurs for $|\ell| = 1$ [12] and is typically in the MHz range such that by applying electric fields of $\sim 100\,\mathrm{V/cm}$ the ℓ doublet states are strongly mixed, resulting in a strong linear Stark shift, as schematically illustrated in Figure 2.4 (a). Furthermore for molecules with $\Lambda = 0$ the spin-rotation coupling is weak and typically $\sim 100\,\mathrm{V/cm}$ are also sufficient to uncouple the electron spin, so that the eigenfunctions are most accurately given by $|\ell N M_N M_S\rangle$ and the Stark shift is obtained as

$$\Delta E_{\ell N M_N} = -dE \frac{\ell M_N}{N(N+1)}. \tag{2.9}$$

This is very similar to the results obtained for symmetric top molecules and diatomic radicals, see Equation 2.3 and 2.6, respectively. We use the convention that $\ell = -|\ell|$ so that the sign of M_N determines sign of the electric field response. States with $M_N > 0$ are low-field-seeking and states with $M_N < 0$ high-field-seeking.

Figure 2.5 (b) illustrates the vibrational energy level structure of a Hund's case (b) molecule with electronic Σ character in the vibrational ground state. The splitting between the different values of ℓ for a given vibrational state $v_2 = 0, 1, 2, 3, 4$, is typically on the order of 100GHz and caused by anharmonic contributions in the

molecular potential [146].

2.2.4 Calculation of branching ratios in the presence of an external electric or magnetic field

In this section we outline the calculation of branching ratios for electronic transitions of diatomic and linear triatomic radicals in the presence of an applied external electric or magnetic field. This is an important tool to choose the best possible excited state and to maximise the decay probability to the ground state which is most suited for opto-electric or opto-magnetic Sisyphus cooling while avoiding decay to states outside of the cooling cycle. In this section we neglect symmetric top molecules and instead refer the reader to the work performed by Zeppenfeld et. al. [26].

We start the calculation of the branching ratios by setting up the Hamiltonian for the ground and excited state in the parity conserved Hund's case (a) basis utilising the open source software PGOPHER [148]. Both Hamiltonians include Λ-doubling, spin-rotation and spin-orbit coupling as well as Stark- or Zeeman-interaction and in case of a linear triatomic molecule also ℓ-doubling. Often either the ground or the excited state is most accurately described by a Hund's case (b) or an intermediate coupling scheme. However a description in Hund's case (a) basis states is still accurate since the basis sets are complete and we can express the Hund's case (b) basis states as a linear combination of Hund's case (a) functions as [13]

$$|\Lambda, S, N, J, M_J\rangle = \sum_{\Sigma=-S}^{+S} (-)^{J-S+\Lambda}(2N+1)^{1/2} \begin{pmatrix} J & S & N \\ \Omega & -\Sigma & -\Lambda \end{pmatrix} |\Lambda, S, \Sigma, J, \Omega, M_J\rangle \,. \tag{2.10}$$

We diagonalise the Hamiltonian for the ground and the excited state at a given electric or magnetic field using PGOPHER [148] and thereby obtain the eigenfunctions of the system, which are superpositions of parity conserved Hund's case (a) basis states. The eigenfunctions of the ground state can be written as

$$|g_i\rangle = \sum_{\epsilon=\pm1} \sum_{J=0}^{J_{\max}} \sum_{\Omega=\Omega_{\min}}^{\Omega_{\max}} \sum_{M_J=-J}^{J} c_i(\epsilon, J, |\Omega|, M_J) \cdot |\epsilon, J, |\Omega|, M_J\rangle \tag{2.11}$$

with $c_i(\epsilon, J, |\Omega|, M_J)$ being complex probability amplitudes such that the square of their absolute value gives the likelihood to find $|g_i\rangle$ in the state $|\epsilon, J, |\Omega|, M_J\rangle$. We want to mention here that for a large enough electric field the opposite parity states of the inversion doublets are strongly mixed such that both parity components $\epsilon = \pm 1$ contribute equally to $|g_i\rangle$. The eigenfunctions of the excited state are given by

$$|e_j\rangle = \sum_{\epsilon'=\pm1} \sum_{J'=0}^{J'_{\max}} \sum_{\Omega'=\Omega'_{\min}}^{\Omega'_{\max}} \sum_{M'_J=-J'}^{J'} c'_j(\epsilon', J', |\Omega'|, M'_J) \cdot |\epsilon', J', |\Omega'|, M'_J\rangle \tag{2.12}$$

where, similar to the ground state, $c'(\epsilon', J', |\Omega'|, M_J')$ are complex probability amplitudes. With this we can calculate the transition strength between an excited state $|e_j\rangle$ and a given ground state $|g_i\rangle$ as

$$T_{ji} = |\langle e_j| \hat{\boldsymbol{\mu}} |g_i\rangle|^2 \tag{2.13}$$

with $\sum_i T_{ji} = 1$ and $\hat{\boldsymbol{\mu}}$ being the electric dipole moment operator. To obtain the branching ratio for an excited state $|e_j\rangle$ we need to calculate T_{ji} for each $|g_i\rangle$, the excited state can decay to. The allowed decay channels are determined by the basis states contributing to $|e_j\rangle$ and the Hund's case (a) selection rules, given by [149, 13]

$$\Delta J = 0, \pm 1, \quad \Delta\Lambda = 0, \pm 1, \quad \Delta\Sigma = 0, \quad \Delta\Omega = 0, \pm 1, \quad \Delta M_J = 0, \pm 1. \tag{2.14}$$

Since we express the eigenfunctions in terms of zero field parity conserved basis states, the parity has to change $\Delta\epsilon : +1 \leftrightarrow -1$ in a single photon electric dipole transition [146]. When considering a linear triatomic molecule then there is an additional selection rule $\Delta l = 0$ [146] that we have to take into account. In total the procedure outlined in this section enables us to calculate the branching ratios for diatomic and linear triatomic radicals in the presence of an applied electric or magnetic field.

2.3 Designing the cooling scheme

Many of the envisioned applications for cold and ultracold molecules make use of the molecule's additional degrees of freedom in comparison to atoms [45, 38, 150]. However, the additional possibilities they provide come along with an increased complexity when it comes to cooling of molecules [117]. In general multiple states are involved in the cooling scheme, so that the example, depicted in Figure 2.1 (b), illustrates the basic idea of opto-electric or opto-magnetic Sisyphus cooling very well, however it is does not reflect a real molecule. In particular we need to develop concepts for opto-electric and opto-magnetic Sisyphus cooling which are generally applicable to various molecular species especially also when the molecule is at first glance not perfectly suited for cooling.

Opto-electric and opto-magnetic Sisyphus cooling can be broken down into three basic components; a suitable cooling potential, created by electric or magnetic fields, the molecular states involved in the cooling scheme in combination with their interaction with an external field as well as radiation to transfer population between states. In the following we will present the most important features of these three components to successfully implement opto-electric or opto-magnetic Sisyphus cooling in a real molecule; techniques to distinguish states, dealing with dark states, choice of the excited state, choice of the ground states and design of the potential. Furthermore we will introduce techniques to overcome common challenges of non-ideal molecules. Throughout this section we will focus on opto-electric Sisyphus

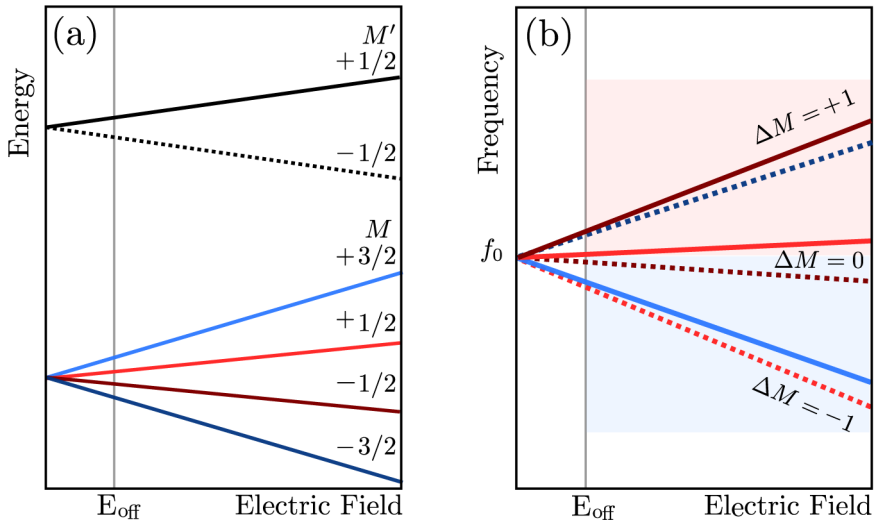

Figure 2.6: *(a) Schematic illustration of the electric field dependence of a molecule with $J = 3/2$ ground state and $J' = 1/2$ excited state. The trap offset field is denoted by E_{off}. (b) Electric field dependence of the transition frequencies between the ground and the excited state for the system shown in (a), where transition including $M' = 1/2$ are illustrated by solid lines and transitions including $M' = -1/2$ by dashed lines. The color code depicts the ground state involved in the transition.*

cooling but all the concepts we will present can be also applied to opto-magnetic Sisyphus cooling.

2.3.1 Techniques to distinguish states

The ability to separate and resolve individual states is crucial for a successful implementation of opto-electric Sisyphus cooling. The most common problems in this respect are degenerate or closely spaced states at zero or low electric fields in the centre of the potential as well as states shifted into resonance in the high field region. Therefore, without the ability to distinguish individual states, this can lead to population of states outside of the cooling cycle, which either complicates or even causes failure of the cooling scheme. To circumvent this we will present techniques to distinguish states utilising frequency selectivity, polarisation of the light field and the sign of the stark shift in combination with the trapping potential. In the absence of an external field the molecule's M-sublevels are degenerate, however by applying an electric bias field the degeneracy is lifted by the Stark effect, as illustrated in Figure 2.6 (a) for a molecule with $J' = 1/2$ excited and $J = 3/2$ ground state. For a sufficiently homogeneous electric field in the centre of the potential, denoted by E_{off} in Figure 2.6 (a), the molecular states are well separated due to the Stark splitting, allowing individual addressing of these states by tuning the frequency of the light field.

In addition to frequency selectivity we can also use the polarisation of the light field to achieve state resolution. Therefore, similar to frequency selectivity, a well defined homogeneous offset field in the centre of the potential, defining the quantisation axis, is required. Figure 2.6 (b) shows the dipole allowed transition frequencies between the ground and the excited state as a function of the applied electric field. The zero field frequency is denoted by f_0 and the color code of the lines illustrates the ground state involved in the transition. For a given, fixed polarisation the number of possible transitions in Figure 2.6 (b) reduces to two. In many cases, reducing the number of possible transitions, utilising the polarisation of the light field, provides enough state selectivity, but this of course depends on the details of the system.

The third technique to realise state selectivity for opto-electric Sisyphus cooling is to make use the high- and low-field-seeking nature of states when applying an external electric field in combination with a detuning of the light field. This is illustrated in Figure 2.6 (b) for a $J' = 1/2$ to $J = 3/2$ transition. The Stark shift of the ground and the excited state result in an electric field dependent transition frequency, where red-detuned radiation, with respect to the zero-field transition frequency f_0, excites red-detuned transitions, while blue detuned transitions remain unaffected. In contrast a blue detuned light field will only couple states with a blue detuned transition frequency. In the following we will demonstrate how to apply this technique to opto-electric Sisyphus cooling using the example depicted in Figure 2.6. To remove kinetic energy from the sample we have to transfer population from the $M = +3/2$ to the $M = +1/2$ ground state in the high field region of the potential. Therefore the $M = +3/2$ state must not be addressed by repumping light in the centre of the trap. In contrast, all the other ground states $M = +1/2, -1/2, -3/2$ have to be coupled to the excited state in the homogeneous field region to avoid losses and enable multiple cooling cycles. As can be seen in Figure 2.6 (b) this can be achieved by illuminating the molecular sample with red detuned light, which pumps population from $M = -3/2, -1/2, +1/2$ into the $M = +3/2$ state, while the $M = +3/2$ state is unaffected as the transition frequency is blue detuned.

2.3.2 Dark states

As already mentioned in 2.3 molecules have a complex internal structure, such that a cooling scheme as illustrated in Figure 2.1 (b) is almost impossible to achieve and decay channels to dark states can often not be avoided. As a consequence of the large energy removal with a single spontaneous emission process, dealing with dark states is not as crucial for opto-electric Sisyphus cooling as for laser cooling techniques. However to exploit the full potential of opto-electric Sisyphus cooling an efficient remixing of dark states is required.

Figure 2.7 summarises the most common situations for opto-electric Sisyphus cooling, where dark states $|d\rangle$ are unintentionally populated. The examples depicted in (a)-(c) are similar and the population in the dark state can be repumped with the same techniques, whereas example (d) is clearly distinct from the others. All three

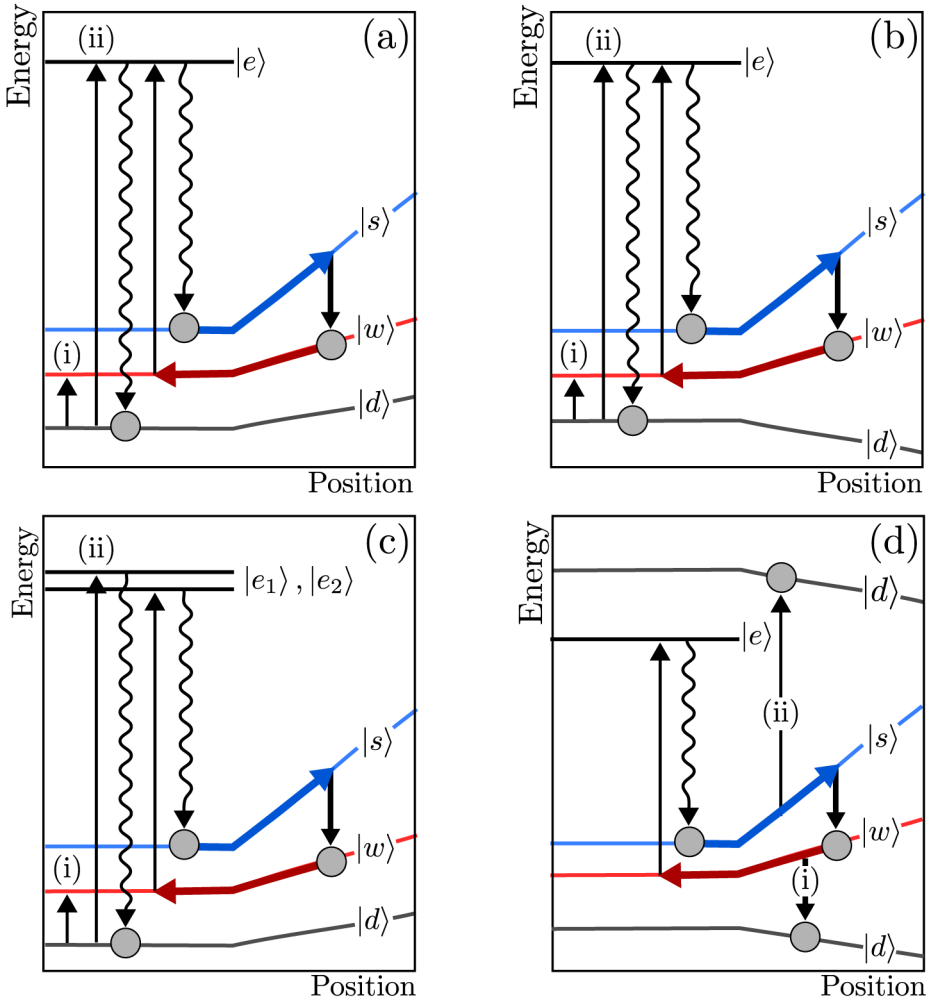

Figure 2.7: *Common examples of decay channels to dark states $|d\rangle$ in opto-electric Sisyphus cooling. (a) Decay of the excited state $|e\rangle$ to a low-field-seeking dark state that can be remixed by (i) rf/microwave radiation or by (ii) laser light. (b) Population decays from $|e\rangle$ to a high-field-seeking dark state with the remixing techniques being identical to (a). (c) Population of $|d\rangle$ due to a simultaneous excitation of a closely-spaced or degenerated excited state decaying to the dark state $|d\rangle$. (d) Dark states are shifted into resonance by the applied electric field and populated by either (i) rf/microwave radiation or (ii) a laser field.*

examples, illustrated in Figure 2.7 (a)-(c) have in common that population decays from an excited state $|e\rangle$ to a dark state $|d\rangle$ outside of the cooling cycle. In contrast to (a) and (b) in (c) the excited state that is used for opto-electric Sisyphus cooling, here labelled $|e_2\rangle$, does not decay to $|d\rangle$. However the separation to the nearby state $|e_1\rangle$ is so small that unintentional excitation of $|e_1\rangle$ can not be avoided, resulting in an additional decay channel to the dark state $|d\rangle$. Both examples depicted in Figure 2.7 (a) and (c) have in common that the dark state is low-field-seeking, such that the population accumulates in $|d\rangle$ and eventually the cooling cycle stops but the molecules remain trapped. In contrast in 2.7 (b) the dark state is high-field-seeking such that without repumping, the population will be lost from the trap. This is a key difference as the high-field-seeking dark state needs to be repumped before the population will be lost, whereas for a low-field-seeker the repumping is not that time critical. In all three examples we can apply the same repumping techniques (i) radio frequency (rf) or microwave fields coupling $|d\rangle$ to $|w\rangle$, which is then repumped to $|e\rangle$, as well as (ii) laser radiation coupling $|d\rangle$ directly to the excited state $|e\rangle$. Which technique is more suited depends on the molecule of choice and the experimental parameters. However when using rf or microwave radiation to remix $|d\rangle$ it is important to balance the power bewteen the rf or microwave field and the laser radiation such that the transition rate for $|w\rangle \rightarrow |e\rangle$ is significantly higher than for $|d\rangle \rightarrow |w\rangle$ to avoid population transfer from $|w\rangle$ to the dark state $|d\rangle$. The last example, illustrated in Figure 2.7 (d), is the most problematic out of the four when implementing opto-electric Sisyphus cooling. Here the electric field shifts dark states into resonance with the applied rf, microwave or laser radiation in the high field region of the trap. In this situation molecules will typically be directly lost from trap and cannot be repumped. Therefore it is essential to avoid this situation whenever possible utilising the techniques introduced in section 2.3.1.

In addition, when implementing opto-electric Sisyphus cooling special attention needs to be paid power of the radiation field driving the $|s\rangle$ to $|w\rangle$ transition in the high field region of the trap, illustrated in Figure 2.1 (b). Since $|w\rangle$ has to be a low-field-seeker the ground state containing $|s\rangle$ and $|w\rangle$ typically consists of at least four M-sublevels, which are driven by the same polarisation and often have an equidistant spacing. Thus we have to choose the power of the radiation, driving $|s\rangle \rightarrow |w\rangle$, very carefully to avoid population of lower lying M-levels or even high-field-seeking states. Therefore the driving rate of $|s\rangle \rightarrow |w\rangle$ has to be slow compared to the population of $|s\rangle$ via repumping of $|w\rangle$.

2.3.3 Choosing the excited state

When choosing the excited state $|e\rangle$ for an opto-electric Sisyphus cooling scheme there are three important criteria one has to keep in mind; the decay rate of the excited state, the sign of Stark shifts for the ground states $|e\rangle$ can decay to, and the number of decay channels. Decay rates can vary by several orders of magnitude, depending on whether $|e\rangle$ is an electronic, vibrational or rotational excited state.

In general a fast cooling rate is beneficial to minimise losses due to a finite trap lifetime. This requires a large spontaneous decay rate of $|e\rangle$, such that an electronic excited state is the natural choice with decay rates typically in the MHz range [115]. However for many molecular species it is not possible to use an electronic excited state, due to bad dissociation properties, an unfavorable excitation wavelength or poor vibrational branching ratios. Depending on the molecule of choice it can be beneficial to use a vibrational level, as demonstrated in [27, 21], or a rotational level, as proposed in [151], at the cost of a slower photon cycling rate ($\sim$Hz) [26, 116]. As long as the excited state only decays to low-field-seeking ground states this does in principle not affect the cooling scheme and significant cooling can be achieved [27, 21]. However, technical limitations, like a finite trap lifetime will typically limit the effectiveness of the cooling scheme, if the decay rate of the excited state is small.

If an excited state decays to high-field-seekers remixing of these states becomes a key criteria for a successful implementation of opto-electric Sisyphus cooling. In order to avoid trap losses, the repumping has to be faster than the trap frequency. This requires a fast remixing rate and thus a large spontaneous decay rate of the excited state, so that typically only systems where $|e\rangle$ is an electronic state allow a sufficiently fast remixing. Thus when choosing the excited state for opto-electric Sisyphus cooling, the requirement for vibrational or rotational excited states to solely decay to low-field-seekers is rather strict, whereas for electronic excited states this requirement can be relaxed as repumping of high-field-seekers is feasible. Furthermore the field-seeking nature of the excited state itself also needs to be considered with respect to the decay rate of $|e\rangle$. In principle the excited state can be high-field- or low-field-seeking for a molecule with a large enough spontaneous decay rate ensuring that $|e\rangle$ has decayed before the molecule will be lost from the trap. This is typically true for electronic excited states, whereas vibrational or rotational excited states are required to be low-field-seeking.

The last of the three criteria that needs to be considered when choosing the excited state is the number of decay channels. Here, of course, a small number of possible decay channels is beneficial, considering that remixing states can decrease the cooling rate significantly. Furthermore a large number of decay channels typically increases the complexity of the experimental realisation of the cooling scheme.

2.3.4 Choosing the ground states

To remove kinetic energy from the system we need, at least two ground states, one with a strong electric field response, labelled $|s\rangle$ and the other with a weaker Stark shift, labelled $|w\rangle$, as illustrated in Figure 2.1 (b). The amount of energy that can be extract with a single spontaneous emission event is set by the differential Stark shifts of these two states. In principle the pair of states with the largest differential Stark shift is best suited, however we also have to keep in mind that the magnitude of the Stark shift of $|w\rangle$ determines the trap depth after the population transfer. Depending on experimental parameters, often a compromise between energy removal

and trap depth of the $|w\rangle$ state has to be made. The criteria mentioned so far are best fulfilled for states with a degenerate or closely spaced pair of opposite parity states, resulting in a linear electric field response, as the ones introduced in section 2.2. The last requirement for the ground states to be suited for opto-electric Sisyphus cooling is that it has to be possible to transfer population from $|s\rangle$ to $|w\rangle$ ideally via direct driving of this transition using a radio-frequency or microwave source.

2.3.5 Designing the potential

A big advantage of opto-electric Sisyphus cooling, compared to other cooling techniques, is that the cooling potential can also be utilised for trapping. The ideal trap for opto-electric Sisyphus cooling provides a homogeneous electric field in the centre region and a large trapping field at the edge of the trap, as illustrated in Figure 2.1 (b). The gradient field at the edge of the trap on the one hand confines the molecules and sets the trap depth while on the other hand it determines the amount of kinetic energy that can be removed with a single spontaneous emission event. Thus for both trapping and energy removal it is beneficial if the maximum field at the edge of the trap is as large as possible. In contrast the electric field in the centre of the trap should be as homogeneous as possible such that the best possible frequency and polarisation selectivity can be achieved. In addition it is also beneficial to have the option to tune the offset field in the centre of the trap. On the one hand this allows to tune branching ratios to maximise the decay probability to $|s\rangle$ and minimise the decay to dark states, as introduced in section 2.2.4. On the other hand it provides the opportunity to adjust the mixing of opposite parity states for the inversion doublets.

The microstructured electric trap presented in [65] was designed to experimentally realise opto-electric Sisyphus cooling of molecules. Besides storing molecular samples with kinetic energies of $\sim k_B \times 0.5\text{K}$, this trap allowed the first experimental demonstration of opto-electric Sisyphus cooling in 2012 [27], reducing the temperature of $\sim 10^7$ CH_3F molecules by a factor of 13.5. In addition with this trap Prehn et. al. utilised opto-electric Sisyphus cooling to obtain largest number of trapped ultracold molecules [21]. A detailed description of the trap can be found in section 3.1.3 of this thesis, therefore we will only highlight the most important features for opto-electric Sisyphus cooling here. The trap consists of a tunable homogeneous offset field in the centre of the trap, covering a large fraction of the trap volume and a steeply rising gradient field towards the edge of the trap with electric fields of up to 60kV/cm. The well defined homogeneous offset field in the centre region allows for both frequency and polarisation selectivity. In addition, due to the large gradient field at the edge of the trap much of the molecules kinetic energy can be removed in a single spontaneous emission process, making this trap the ideal platform to realise opto-electric Sisyphus cooling.

Besides the microstructured electric trap developed in our group, there are also other traps well suited for opto-electric Sisyphus cooling, including electric field

Ioffe-Pritchard traps. For this kind of trap there exist several proposals including the "chain-link" [152], "six-wire" [153] and "EZ" [54] trap, as well as an experimental demonstration of NH_3 and ND_3 trapping with the "IP-type" trap [64], which all provide an appropriate potential for opto-electric cooling. For opto-magnetic Sisyphus cooling, the magnetic Ioffe-Pritchard type traps are especially well suited for polarisation selectivity.

In addition microwave or optical dipole traps [154] are promising platforms to implement Sisyphus cooling. They have the advantage that for a properly chosen detuning of the trapping field, all relevant states remain trapped which solves the problems associated with transitions to high-field-seeking dark states.

2.4 Implementing opto-electric and opto-magnetic Sisyphus cooling in a molecule

Closed-shell symmetric top molecules are particularly well suited for opto-electric Sisyphus cooling with the first cooling schemes proposed by Zeppenfeld et al. in 2009 [26]. In this section we will use this type of molecule as a role model to illustrate how to apply the concepts introduced in the previous section and how to establish a cooling scheme for a real molecule. With this in place we move to more diverse species by introducing cooling schemes for opto-electric as well as for opto-magnetic Sisyphus cooling for an idealised diatomic radical. Unfortunately, it is unlikely to find such an ideal molecule so in the next step we move away from the ideal case and show how to handle common challenges when designing a cooling scheme for diatomic radicals. In the last part of this section we depict how to apply opto-electric Sisyphus cooling to linear triatomic molecules.

2.4.1 Cooling of a closed-shell symmetric top molecule

The cooling scheme we present in this section is not restricted to a specific molecule, instead it is generally applicable to various closed-shell symmetric top molecules. We start the design of the cooling scheme by choosing the best-suited excited state. Although electronically excited states provide the fastest decay rate, and thereby also the fastest cooling rate, they are not suited for closed-shell symmetric top molecules due to bad dissociation properties, poor vibrational branching ratios and typically the excitation wavelength is in the ultraviolet. Instead, a better choice is a vibrational excited state or more precisely the first excited vibrational mode $v = 1$ as it has a strong decay back to the vibrational ground state $v = 0$. Typically vibrational states have decay rates of up to 100Hz and are usually accessible with commercially available near infrared laser systems. We also have to consider the rotational quantum numbers of the excited state and the corresponding selection rules given by

$$\Delta J = 0, \pm 1, \quad \Delta K = 0, \quad \Delta M_J = 0, \pm 1 \tag{2.15}$$

for a parallel vibrational transition [155].

For successful implementation of opto-electric Sisyphus cooling it is important that the excited states decays to a pair of states $|s\rangle$ and $|w\rangle$ suited to remove kinetic energy from the sample in the high field region of the trap. These states can either be M-levels of the same J or one can also select $|s\rangle$ and $|w\rangle$ from different J levels, where the method of choice of course depends on the details of the system. We want to note that there are subtleties with both methods, which we will briefly highlight in the following.

As discussed in section 2.3.4 both $|s\rangle$ and $|w\rangle$ need to be low-field-seeking, from Equation 2.3 we find that $M' \geq 2$ is mandatory if they lie within the same J. As a consequence, the ground state will comprise of at least five equally spaced levels, that are driven by radiation of the same frequency and polarisation. To avoid transitions from $|w\rangle$ to dark states the driving rate of the $|s\rangle \rightarrow |w\rangle$ transition in the gradient field has to be significantly slower than the optical pumping rate back into $|s\rangle$ via the excited state $|e\rangle$ in the centre of the potential. This has been experimentally realised with great success [26, 21], however as a consequence it significantly slows down the cooling rate. In contrast if $|s\rangle$ and $|w\rangle$ are chosen to be in different J levels the $|s\rangle \rightarrow |w\rangle$ transition can be driven at higher rates, but dark states can still be created. This requires special care when designing the cooling scheme and is highly dependent on the specific choice of molecular species and trap design. Within this thesis we will always use the more generic technique $|s\rangle$ and $|w\rangle$ from the same J, as for the molecules we consider, one can almost always find a suited pair of states.

As the decay rate of the vibrational excited state is slow compared to the trap frequency the requirement to only decay to low-field-seeking states is rather strict. Taking Equation 2.3 and 2.15 into account we find that for states with $K' \geq 1$ and $M' \geq 2$ the system only decays to low-field-seeking states including a pair of states for $|s\rangle$ and $|w\rangle$. In addition one can also exploit the fact that the number of decay channels is minimised if $J' = K' = M'$, such that a well suited $|v'; J', K', M'\rangle$ excited state is e.g. $|1, 2, 2, 2\rangle$. Stretched states with larger values for J' are equally well suited as experimentally demonstrated in [27].

Figure 2.8 (a) shows the cooling scheme for a closed-shell symmetric top molecule with the excited state $|1, 2, 2, 2\rangle$ which decays to only five ground states. The best choice for the $|s\rangle$ and $|w\rangle$ state are $|0, 2, 2, 2\rangle$ and $|0, 2, 2, 1\rangle$, respectively as they allow the largest energy removal while maintaining a good trap depth for molecules in $|w\rangle$. The $|w\rangle$ state as well as the dark states $|d_1\rangle$-$|d_3\rangle$ need to be repumped, where state selectivity can be, for example, achieved by frequency selectivity. To achieve this, an offset field E_{off} has to be applied in the central region of the trap causing a Stark splitting such that the states can be individually addressed by tuning the frequencies of the light fields. The dark states $|d_1\rangle$-$|d_3\rangle$ can be coupled to $|w\rangle$ via microwave radiation while the population in $|w\rangle$ is transferred to the excited state $|e\rangle$ by laser radiation, allowing population to accumulate in $|s\rangle$. A more advanced version of the cooling scheme is depicted in Figure 2.8 (b) utilising the low-field seeking dark states as additional cooling levels.

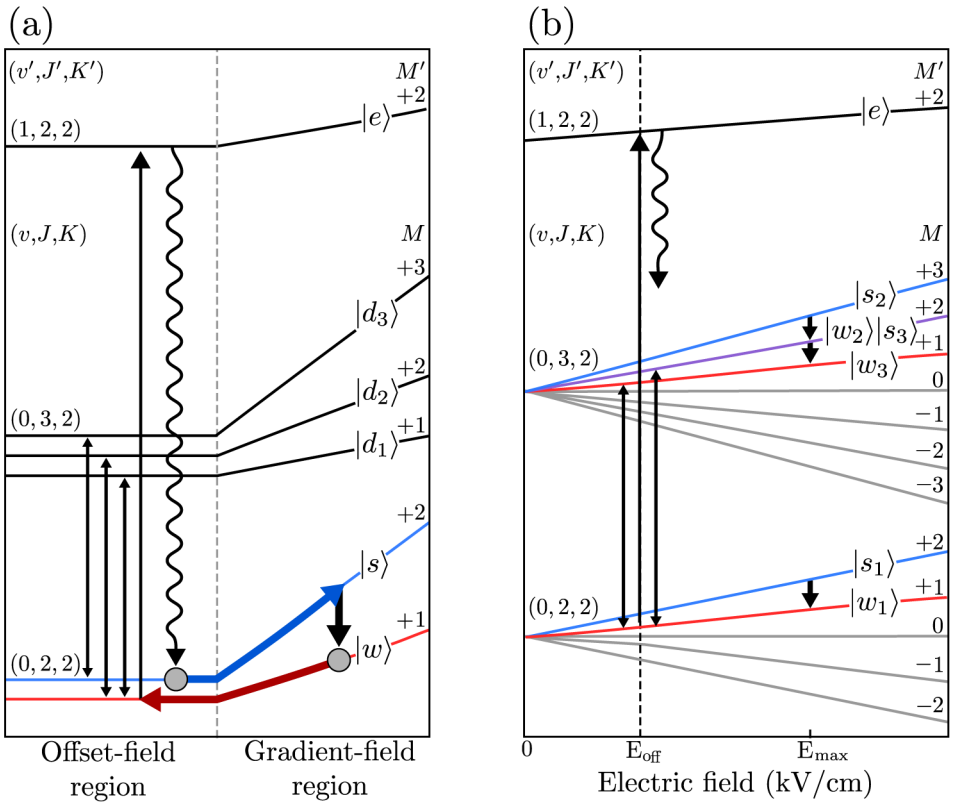

Figure 2.8: *(a) Position dependent representation of a cooling scheme for a closed-shell symmetric top molecule in an electric trap. (b) Extension of the scheme presented in (a) by including the dark states as additional cooling levels. The scheme is depicted in the electric field dependent representation and the grey colored states are not part of the cooling cycle as decays to these states are dipole forbidden.*

Using this simple, idealised example depicted in Figure 2.8, we can also illustrate polarisation selectivity. Coupling of the two rotational levels $J = 3$ and $J = 2$ involved in the cooling scheme can be achieved by using π-polarised light. The population is driven from the ground state back to the excited state by means of σ^--polarised light via $|w_1\rangle = |0, 2, 2, 1\rangle$, as illustrated in Figure 2.8 (b). So far this oonly repumps four of the five ground state thus in addition we have to couple the s_3 state into the system by radio-frequency in the high field region. However polarisation selectivity does not allow to cool both $\pm K$ states simultaneously as reversing K also reverses M.

The last of the three techniques, introduced in section 2.3.1 makes use of the electric field dependence of the transition frequencies in combination with a detuned light field. For the example depicted in Figure 2.8 (b) transitions from $J' = 2$ to $J = 2$ are especially well suited for this technique, as the dipole moments of states with $J' = J$ are typically similar. Applying an external electric field shifts the

transition frequencies such that σ^--transitions are blue-detuned. Illuminating the sample with blue-detuned light provides identical results as polarisation selectivity with σ^--polarised light with one major advantage, as it allows to simultaneously cool both components of $\pm K$. There is one important subtlety we need to consider to successfully implement this technique; the coupling of $J' = 2$ to $J = 2$ has to happen at a much faster rate than the remixing of the rotational levels.

To install an efficient cooling scheme it is important that states outside of the cooling cycle are not unintentionally populated. Therefore we need to carefully inspect the system for driving of unwanted transitions by the applied radiation fields. For closed-shell symmetric top molecules the rotational constants of the vibrational excited and the vibrational ground state are typically quite similar, such that the transition frequency of $|2, 2, M\rangle \leftrightarrow |2, 2, M'\rangle$ and $|3, 2, M\rangle \leftrightarrow |3, 2, M'\rangle$ are also similar. Furthermore microwave radiation used to couple the rotational ground states $|2, 2, M\rangle \leftrightarrow |3, 2, M\rangle$ is similar in frequency to the same transition in the excited state $|2, 2, M'\rangle \leftrightarrow |3, 2, M'\rangle$. Both scenarios can cause a population of the $|3, 2, M'\rangle$ state which creates additional decay channels outside of the cooling scheme, as e.g. populating states in the $J = 4$ level. These two specific examples for the cooling scheme depicted in Figure 2.8 are used to illustrate the problem of coupling to other states. In general the coupling to unwanted states needs careful analysis of the system as it depends a lot on the molecular parameters and the details of the experiment. Concepts to deal with other resonant state in the energy structure of the molecule can be found here 2.3.1.

2.4.2 Opto-electric and opto-magnetic Sisyphus cooling of an idealised diatomic radical

In this section we show how to design an opto-electric and an opto-magnetic Sisyphus cooling scheme for an idealised pure Hund's case (a) diatomic radical. Idealised in this respect means that we choose a molecule with a suitable but common electronic structure, as introduced in section 2.3.4, consisting of a $X^2\Pi(v = 0)$ electronic ground and a $A^2\Delta(v' = 0)$ electronic excited state. Furthermore, for now we neglect hyperfine coupling, to illustrate the important concepts for Sisyphus cooling of a diatomic radical without being lost in molecule-specific details. We also assume the FCF to be one such that we can neglect loss of population to higher vibrational states.

Opto-electric Sisyphus cooling

The idealised diatomic molecule we consider shows many similarities but, also clear deviations from, a symmetric top molecule when designing a cooling scheme. The first difference is that we can utilise an excited electronic state for diatomic radicals [22]. The merit of an electronic transition is the fast spontaneous decay rate that allows us to extend the cooling scheme to molecules with decay channels to high-

field-seeking states. The photon cycling rate, and therefore the repumping rate, can now be faster than the trap frequency, which will become important later in this section. Nevertheless one should always try to avoid decay channels to high-field-seeking states either by the methods described section 2.3 or by utilising selection rules. The selection rules for a pure Hund's case (a) electronic transition are given by Equation 2.14, which we can exploit to minimise the number of possible decay channels.

The idealise molecule we consider has a spin of $S = 1/2$, causing the excited state to split into two spin-orbit components $^2\Delta_{5/2}$ and $^2\Delta_{3/2}$ and the ground state divides into the two components $^2\Pi_{3/2}$ and $^2\Pi_{1/2}$. From inspection of the selection rules (Equation 2.14), using the $\Omega' = 5/2$ component of the excited state allows us to restrict the decay to $\Omega = 3/2$ only.

To further minimise the number of decay channels and to ideally only decay to low-field-seeking states we have to inspect the basis states of a Hund's case (a) molecule in the presence of an applied offset field. The offset field mixes the zero-field basis states with well defined parity, given by Equation 2.4, and the eigenstates asymptotically become $|J, \Omega, M_J\rangle$ states. These are states with a signed value of Ω and the sign is conserved during spontaneous emission, so that a low-field-seeking excited state can only decay to a low-field-seeking ground state. However, in contrast to closed-shell symmetric top molecules, for diatomic radicals the opposite parity states are not degenerate but typically separated by a few hundred MHz up to several GHz, depending on the molecular state and the molecule of choice. Therefore states of opposite parity are usually not well mixed at small electric fields, $E_{\text{off}} \ll \Delta/2d$, with Δ being the inversion splitting and d the dipole moment of the molecule. Consequently a description by parity eigenstates, given by Equation 2.4, is most accurate and only at large electric fields, $E_{\text{off}} \gg \Delta/2d$, states with a signed value of Ω provide a good description. For $E_{\text{off}} \gg \Delta/2d$ diatomic radicals behave identical to closed-shell symmetric top molecules and spontaneous decay can only occur from low-field-seekers to low-field-seekers. However, in an intermediate regime, where neither parity eigenstates nor states with a signed value of Ω provide an accurate description, population decays to both components of the inversion doublet, making an electronic excited state mandatory to ensure fast repumping of the high field seeking component of the inversion doublet.

Besides complicating the decay in the centre region of the potential the Λ- or Ω-doublets can also cause problems when transferring population from the $|s\rangle$ to the $|w\rangle$ state in the high field region of the trap, as illustrated in Figure 2.9 (a). If the applied offset field is too low to couple the opposite parity states of the inversion doublet strongly, population can be accidentally transferred from low-field-seeking to high-field-seeking states. This happens if the radiation driving $|s\rangle \rightarrow |w\rangle$ in the high field region is resonant with opposite parity states in the centre of the potential and can be avoided by applying a large enough offset field, $E_{\text{off}} \gg \Delta/2d$, as illustrated in Figure 2.9 (b). In this situation the eigenstates are characterised by a signed value of Ω such that transitions changing the sign of Ω or equivalently

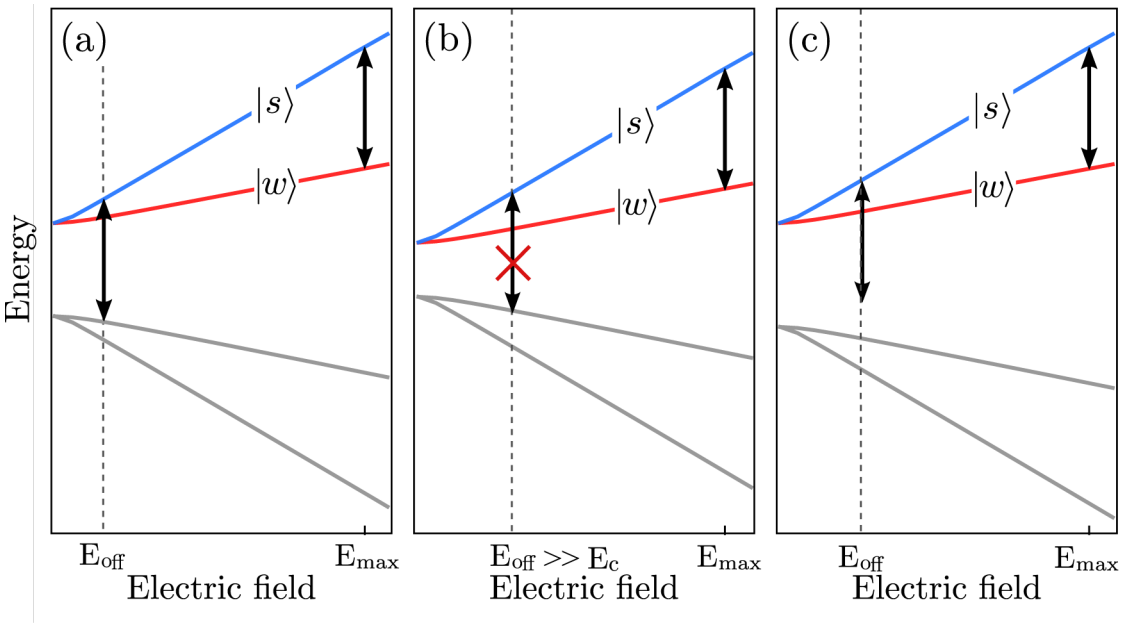

Figure 2.9: *(a) Radiation driving the $|s\rangle \rightarrow |w\rangle$ transition in the high field region also couples opposite parity states in the centre of the potential. (b) Suppression of the transition to the lower inversion component by increasing the offset field to $E_{off} \gg E_c$, with $E_c = \Delta/2d$. (c) No population transfer in the low field region of the trap as the inversion doublet is larger than the differential stark shift of the $|s\rangle$ and $|w\rangle$ state in the high field region.*

transitions between the two components of the inversion doublet are suppressed. Another possibility to avoid a coupling between the upper and the lower component of the inversion doublet is shown in Figure 2.9 (c). Here the combination of the inversion splitting with an applied offset field E_{off}, creates a separation between the opposite parity states of the Λ- or Ω-doublet that is significantly larger than the energy spacing between the $|s\rangle$ and the $|w\rangle$ state at the maximum electric field. Thus radiation driving the $|s\rangle \rightarrow |w\rangle$ transition in the high field region is no longer resonant with opposite parity states in the low field region of the trap. These three techniques are generic and can be applied across any molecule with this structure. It also highlights the power of having a tunable offset potential field, as discussed in Section 2.3.5.

Taking these considerations into account we can design an opto-electric cooling scheme for an idealised diatomic Hund's case (a) molecule with $A^2\Delta_{5/2}(v' = 0)$ excited and $X^2\Pi_{3/2}(v = 0)$ ground state, illustrated in Figure 2.10 (a). By choosing the $|\frac{5}{2}, \frac{5}{2}, \frac{5}{2}\rangle$ excited state in the $|J, \Omega, M_J\rangle$ basis, we restrict the decay to the $\Omega = 3/2$ component of the ground state and ensure that the inversion doublets of all states involved in the cooling scheme are small enough to be strongly mixed by a reasonably low offset field E_{off}. Therefore the basis $|J, \Omega, M_J\rangle$ provides the most accurate description and the low-field-seeking excited state can only decay to low-field-seeking ground states as the sign of Ω is preserved in a spontaneous emission

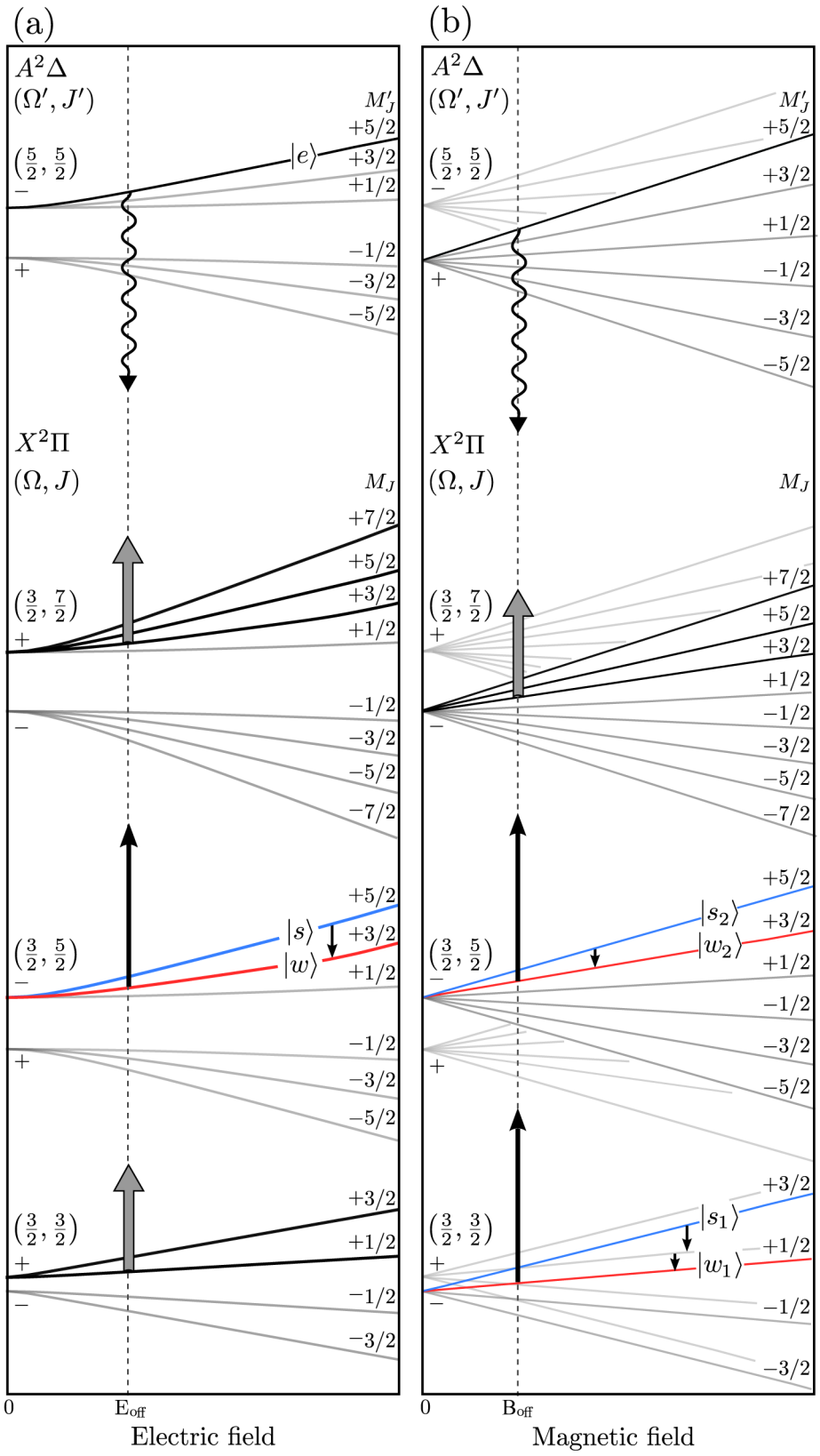

Figure 2.10: *(a) Opto-electric and (b) opto-magnetic Sisyphus cooling scheme of a pure Hund's case (a) idealised diatomic radical with $A^2\Delta(v = 0)$ electronic excited and $X^2\Pi(v' = 0)$ electronic ground state. The thick arrows illustrate repumping of multiple M-levels, whereas the thin arrows indicate repumping of a single M-state.*

event. The most suited pair of states in the ground state for $|s\rangle$ and $|w\rangle$ are the $|\frac{5}{2}, \frac{3}{2}, \frac{5}{2}\rangle$ and the $|\frac{5}{2}, \frac{3}{2}, \frac{3}{2}\rangle$ state, as they allow to remove a significant amount of energy while the population transferred to the $|w\rangle$ state remains well trapped. Here, our choice of the excited state has another merit due to it's strong decay to the $|s\rangle$ state. Further decay channels are distributed over three different J levels, $J = 7/2$, $J = 5/2$ and $J = 3/2$ according to the Hund's case (a) selection rules, given by Equation 2.14. Possible decay channels, except for $|s\rangle$ and $|w\rangle$, are highlighted by black solid lines in Figure 2.10 (a). To enable multiple cooling cycles we have to repump all decay channels, which are not required for cooling, by broad band coupling in the centre region of the trap. Thus we have to avoid $|s\rangle$ to be addressed by the repumping light in the trap centre using the methods presented in section 2.3.1. For the example presented in Figure 2.10 (a) we make use of the homogeneous offset field in the centre of the trap to achieve frequency selectivity such that we do not repump $|s\rangle$ but transfer population from $|s\rangle$ to $|w\rangle$ in the high field region of the trap to remove kinetic energy from the system.

Opto-magnetic Sisyphus cooling

Besides utilising the strong interaction between the molecules electric dipole moment and an external electric field for opto-electric Sisyphus cooling, molecular radicals are also well suited for opto-magnetic Sisyphus cooling. Here one makes use of the interaction between the spin and orbital angular momentum of the molecule and the applied external magnetic field. A key difference between opto-electric and opto-magnetic Sisyphus cooling is that electric fields mix states of opposite parity whereas magnetic fields couple states with identical parity. Thus, independent of the magnitude of the Λ- or Ω-doubling, the Zeeman shift is linear, even at small magnetic fields, as can be seen in Figure 2.10 (b) and the parity basis is well-defined across the entire potential. As a consequence, the complications arising from the inversion doublets with respect to the decay channels for opto-electric Sisyphus cooling, discussed section 2.4.2, can be omitted for it's magnetic counterpart. Applying an offset field is therefore only required to achieve state selectivity and not to suppress decay channels to high-field-seeking states. For opto-magnetic Sisyphus cooling a restriction of the decay to low-field-seekers only can be achieved simply by choosing $M'_J \geq 3/2$ for the excited state. However, the fact that opposite parity states are not mixed by the applied magnetic field complicates the population transfer from $|s\rangle$ to $|w\rangle$ in the high-field region of the trap as magnetic transitions are weak in comparison to electric dipole transitions. Consequently if the $|s\rangle \rightarrow |w\rangle$ transition is accidentally resonant with a transition between opposite parity states elsewhere in the trap, the electric dipole transition will be driven with a much larger rate. One can avoid this by carefully choosing the $|s\rangle \rightarrow |w\rangle$ transition frequency such that no opposite parity state is resonant, which works in particular well for molecules with large inversion splitting and if the upper component of the inversion doublet is used for cooling, as illustrated in Figure 2.11 (a). However, we have to keep in mind

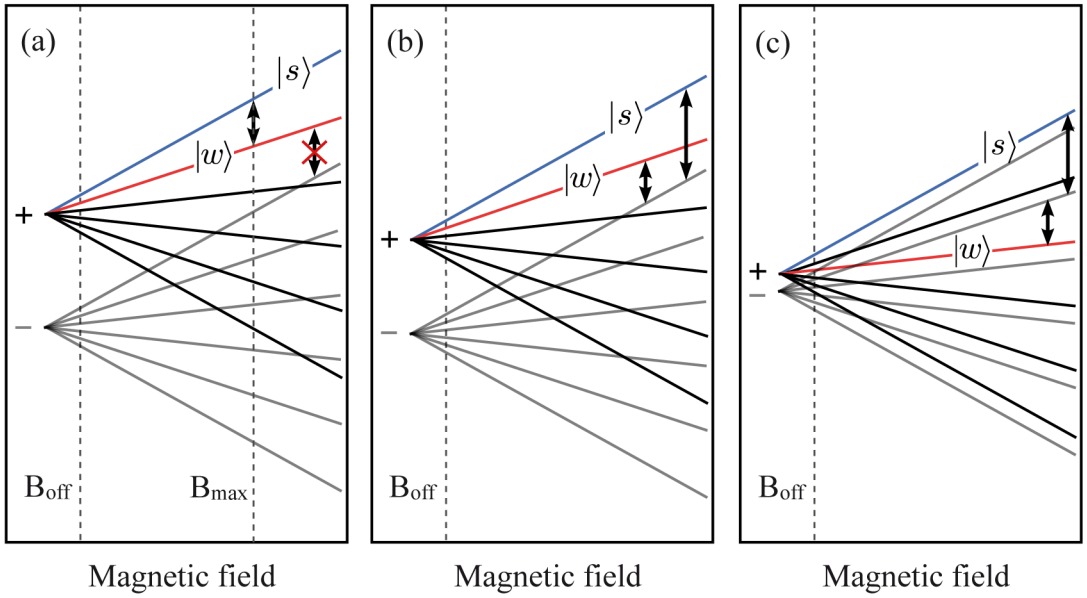

Figure 2.11: *Opto-magnetic Sisyphus cooling of a molecule with (a) large inversion splitting utilising a magnetic transition, (b) intermediate and (c) small inversion doubling using electric dipole transitions to opposite parity states.*

that this only works if the magnetic field does not exceed $B_{\max}$ or for molecules with sufficiently low kinetic energy. Otherwise, as illustrated in Figure 2.11 (a), $|w\rangle$ can be transferred to an opposite parity state, that is not suited to remove kinetic energy from the sample. As depicted in Figure 2.11 (b) and (c) one can also utilise electric dipole transitions to transfer population from $|s\rangle$ to $|w\rangle$ in the high-field region by including the opposite parity component of the Λ- or Ω-doublet utilising two light fields of different frequncy. Figure 2.11 (b) illustrates an example scheme for a rather large inversion splitting whereas (c) demonstrates a possible implementation for a small Λ- or Ω-doublet. Besides applying radiation with two distinct frequencies in the high-field region of the trap one can also choose $|s\rangle$ and $|w\rangle$ from the two opposite parity components of the inversion doublet. However in this situation both components of the inversion doublet need to be coupled to the excited state and and the inversion splitting adds or subtracts an offset to the driving frequency in the high field region.

For the example scheme depicted in Figure 2.10 (b) we use a $A^2\Delta(v' = 0)$ excited and a $X^2\Pi(v = 0)$ ground state. For molecules in a $^2\Pi$ state, only the $\Omega = 3/2$ component shows a strong magnetic field interaction. For states with $\Omega = 1/2$, $\Sigma = \pm 1/2$ and $\Lambda = \pm 1$ point in opposite directions such that in combination with the Landé g-factors of $g_L \approx 1$ and $g_s \approx 2$ the Zeeman shift is apporximately zero. Therefore we use the $\Omega' = 5/2$ component of the excited state as it solely decays to $X^2\Pi_{3/2}$. Furthermore, as already mentioned, choosing $M'_J \geq 3/2$ ensures decay to low-field seeking states only, such that $|-, \frac{5}{2}, \frac{5}{2}, \frac{5}{2}\rangle$ is a good choice for the excited

state. As we consider a pure Hund's case (a) coupling scheme and due to the fact that the parity must change in an electric dipole transition we only decay to seven states. According to the discussion of the previous paragraph we can either use a magnetic or two-electric dipole transitions to transfer population in the high-field region of the trap, which we label with $|s_2\rangle \rightarrow |w_2\rangle$ and $|s_1\rangle \rightarrow |w_1\rangle$ in Figure 2.10 (b), respectively. Which of the two schemes is more suited to remove kinetic energy depends on the molecule of choice and the experimental details.

2.4.3 Moving away from the ideal case

Unfortunately, diatomic radicals will typically deviate from the idealised example introduced in the previous section. In general there are four common complications, which we will introduce in the following and consider their impact on successful implementation of opto-electric or opto-magnetic Sisyphus cooling. Typically FCF $\neq 1$ for diatomic radicals, so that in an electronic transition population does not only decay to a single vibrational level, but can include multiple vibrational states. Here, if necessary, vibrational repump lasers can be added as for the standard laser cooling experiments. The second complication arises from the nuclear spin angular momentum diatomic radicals typically possess and the resulting hyperfine structure that needs to be considered when designing a cooling scheme. Furthermore we need to take into account that the energy level structure of diatomic molecules often deviates from a pure Hund's case (a) structure, and many diatomic molecules do not possess an inversion doublet in the ground state. For each of these we consider the complications to opto-electric and opto-magnetic Sisyphus cooling and how they can be countered for successful implementation.

Hyperfine structure

To include hyperfine structure we couple the nuclear spin I and the electronic angular momentum J of the molecule to obtain the total angular momentum F according to $F = I + J$ [13]. When no external field is applied the total angular momentum is degenerate with a $(2F+1)$-degeneracy. However, in the presence of an external field the degeneracy is lifted and M_F, the projection of F onto the external field axis, can take the values $-F, -F+1, ..., F-1, F$. In general the interaction of the nuclear spin with other angular momenta components is weak and only leads to small splittings, which typically do not exceed a few hundred MHz. Typically the application of a moderate offset field in the centre of the trap is sufficient to uncouple the nuclear spin such that $|F, M_F\rangle$ states form groups that behave like a single $|J, M_J\rangle$ state. In this situation the hyperfine levels do not need to be considered as individual states but can simply be treated as a broadening of the transition for the respective $|J, M_J\rangle$ state.

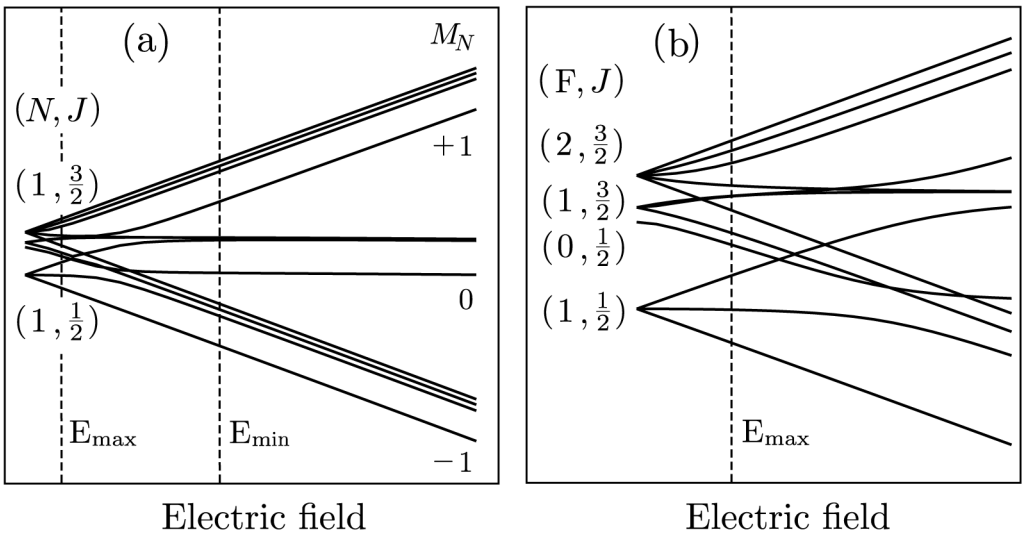

Figure 2.12: *(a) Electric field response of a Hund's case (b) diatomic molecule with* $\Lambda > 0$*. (b) Zoom-in to the low-field region of (a).*

Molecules with intermediate or Hund's case (b) coupling scheme

In the idealised example, introduced in the previous section, both the electronic excited state as well as the electronic ground state were assumed to have pure Hund's case (a) character. However, often an intermediate coupling scheme between Hund's case (a) and (b) or a description by pure Hund's case (b) is more accurate. For molecules with $\Lambda > 0$ in the electronic ground state the concepts introduced in section 2.4.2 still apply and the behavior is in many cases similar to a pure Hund's case (a) molecule, however Ω will no longer be well defined. As a consequence additional decay channels that were previously forbidden by selection rules are now allowed, creating more states that have to be repumped, such that the repumping scheme becomes more evolved. For pure Hund's case (b) molecules the spin-rotation interaction can be weak such that the splitting between the different spin-rotation components $J = N \pm S$ will be mixed already at typical offset fields in the centre of the trap. This in combination with hyperfine coupling, causing anticrossings in the low-field region, complicates the design of a successful cooling scheme. Figure 2.12 (a) illustrates two possible solutions; the first solution requires applying a minimal electric field E_{min} in the centre of the potential which ensures that all spins are decoupled. In this situation the states are described by the rotational quantum number N, where J and F are no longer well defined. The second solution requires molecules that are cold enough such that one can restrict the field to E_{max}, as depicted in Figure 2.12 (a) and by the zoom-in in Figure 2.12 (b). Here one makes use of the fact that for low enough fields the hyperfine and spin-rotation levels are still well defined.

Molecules without orbital angular momentum in the electronic ground state

The vast majority of molecules that has been directly cooled to ultracold temperatures, like CaF or SrF, has a $A^2\Pi$ electronic excited and a $X^2\Sigma$ electronic ground state, which has $\Lambda = 0$. Consequently these molecules do not possess a pair of degenerate or closely spaced opposite parity states in the electronic ground state, and therefore no linear Stark shift for low or moderate electric fields. Instead for molecules with a Σ ground state the electric field couples adjacent rotational levels resulting in a quadratic Stark shift, as can be seen in Figure 2.13 (a). As the splitting between the rotational states is typically on the order of several tens to hundreds of GHz, the field response remains quadratic even for electric fields as large as 100kV/cm. Consequently the energy removal per scattered photon is small compared to typical values for opto-electric Sisyphus cooling. Furthermore in the presence of a sufficiently large electric field parity is no longer well defined, which increases the number of possible decay channels significantly. We can take an exemplary look at the standard laser cooling transition for these molecules, given by $X^2\Sigma^+(v = 0)\,|\epsilon = -1, N = 1\rangle \rightarrow A^2\Pi_{1/2}(v' = 0)\,|\epsilon' = +1, J' = 1/2\rangle$ [117]. This transition is rotationally closed, however in the presence of a sufficiently strong electric field this is no longer the case and the excited state can decay to three rotational levels, $N = 0, 1, 2$, where each of them requires a separate repump laser. Furthermore none of these rotational levels are well suited for opto-electric Sisyphus cooling, as there is no pair of low-field-seeking states on which to operate the cooling. In contrast the $N = 3$ level can be used for opto-electric Sisyphus cooling as it provides two low-field-seeking states with a decent differential Stark shift and a $|w\rangle$ state with acceptable trap depth, as illustrated in Figure 2.13 (a). However, to enable decay to the $N = 3$ level we need to choose an excited state with larger angular momentum than the $|J', \Omega'\rangle = |1/2, 1/2\rangle$ used for laser cooling. For example $A^2\Pi_{3/2}(v' = 0)\,|J' = 7/2, \Omega' = 3/2, M'_J = 1/2\rangle$, illustrated in Figure 2.13 (a), is a good choice for the excited state with a strong decay to the $|s\rangle$ state. A consequence of the larger angular momentum is that the excited state decays now to four ($N = 2, 3, 4, 5$) instead of three rotational levels, which complicates the cooling scheme even further. Moreover molecules with a Σ ground state have another disadvantage for the implementation of opto-electric Sisyphus cooling; the state with the smallest M_J-value has the strongest low-field-seeking electric field response, such that polarisation selectivity can not be utilised to distinguish states. Thus in total opto-electric Sisyphus cooling of a $A^2\Pi - X^2\Sigma$ molecule is in principle possible but extremely challenging, and not worthwhile when many successful laser cooling techniques exist for these molecules. This illustrates how opto-electric Sisyphus cooling is a complementary technique to laser cooling.

When considering opto-magnetic Sisyphus cooling of molecules with $\Lambda = 0$ in the electronic ground state we have to take a look at the magnetic field response of

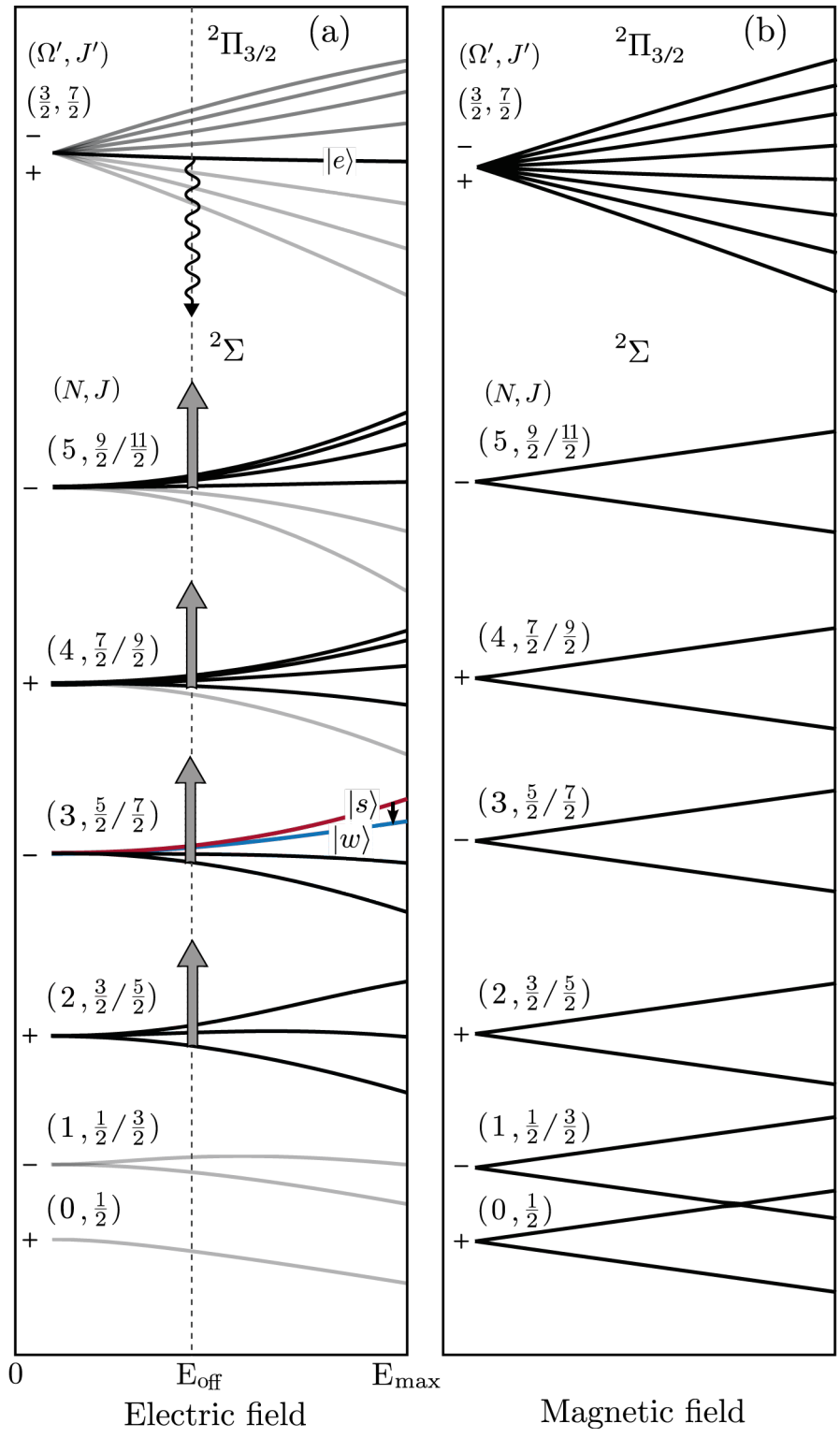

Figure 2.13: *(a) Schematic illustration of an opto-electric Sisyphus cooling scheme for molecules with an $A^2\Pi(v' = 0)$ excited and a $X^2\Sigma(v = 0)$ ground state. (b) Magnetic field response of the example illustrated in (a).*

a Hund's case (b) molecule in a strong magnetic field, which is given by [156]

$$\Delta_{\Lambda NS} = \left(g_L \frac{\Lambda^2 M_N}{N(N+1)} + g_S M_S \right) \mu_B B. \tag{2.16}$$

As usual the Bohr magneton is given by μ_B and the Landé g-factors associated with L and S are described by g_L and g_S. The projections of N and S onto the external field axis are characterised by M_N and M_S, respectively. For a molecule without orbital angular momentum in the electronic ground state, $\Lambda = 0$, we can see from Equation 2.16 that the spin quantum number M_S determines the Zeeman shift for large magnetic fields. Thus the magnetic field response of a molecule with spin $S = 1/2$ is given by a low-field- and a high-field-seeking component for a given rotational state according to $M_S = \pm 1/2$, as illustrated in Figure 2.13 (b). Consequently there is no pair of states with a suitable differential Zeeman shift across the rotational ladder of a $X^2\Sigma$ state for opto-magnetic Sisyphus cooling at large magnetic fields.

Although not shown in this thesis, at ultracold temperatures ($\sim 70\mu$K) opto-magnetic Sisyphus cooling can be realised in a Ioffe-Pritchard trap for molecules without orbital angular momentum in the electronic ground state, $\Lambda = 0$. Here, similar to example shown in section 2.4.3, one makes use of the fact that at small magnetic fields ($\sim 150\mu$T) F is still well defined as the nuclear spin is coupled to the electronic angular momentum.

2.4.4 Cooling a linear triatomic radical molecule

Another class of molecules that is amenable to opto-electric Sisyphus cooling are linear triatomic radicals. After the discussions in the previous sections this might be surprising, as the most popular examples of this class of molecules used in the field of cold and ultracold molecules, like SrOH, CaOH or YbOH, occur in a Σ vibronic ground state with Λ=0 [157]. Thus these molecules do not posses a pair of degenerate or closely spaced opposite parity states in the ground state which at first glance makes them unsuitable for opto-electric Sisyphus cooling. However, in contrast to diatomic molecules, linear triatomic molecules posses additional degrees of freedom, including the vibrational bending mode $v_2^{|\ell|}$, introduced in section 2.2.3. This degenerate vibrational bending mode can give rise to an angular momentum G with projection $\pm\ell$ onto the molecular symmetry axis. This results, similar to diatomic molecules with Λ- or Ω-doubling, in a pair of closely spaced opposite parity states, which is the perfect starting point for a successful implementation of opto-electric Sisyphus cooling. However, these molecules are not suited for opto-magnetic cooling even if a vibrational angular momentum is excited, as it only slightly modifies the magnetic moment and the Zeeman shift of the molecule. For a radical with spin $S = 1/2$ the magnetic field response in the high field limit is given by the two spin configurations $M_S = \pm 1/2$. Consequently, the differential Zeeman shift is negligible

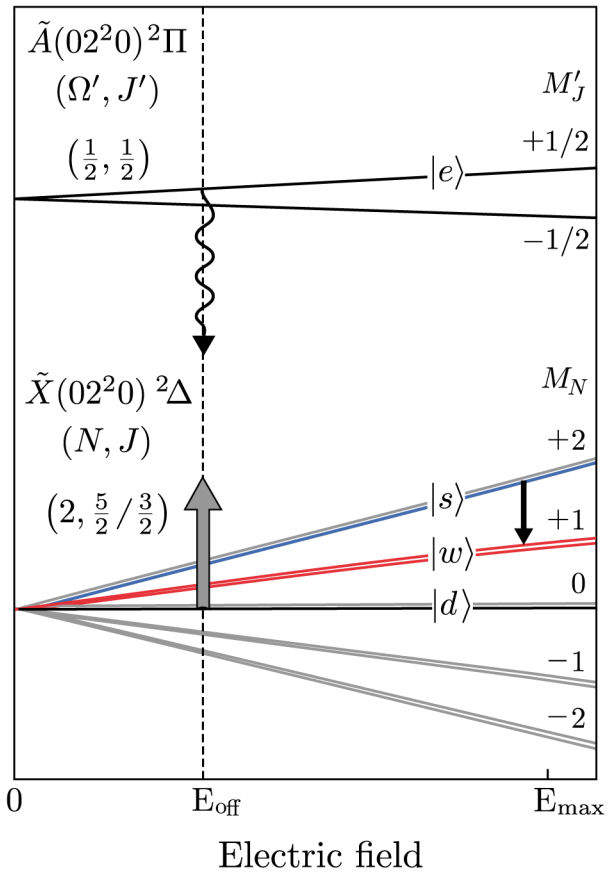

Figure 2.14: *Opto-electric Sisyphus cooling scheme for a linear triatomic radical with a $\tilde{A}^2\Pi$ excited and $\tilde{X}^2\Delta$ ground state, where both states are excited to the vibrational bending mode $v_2^{|\ell|} = 2^2$.*

over the whole rotational ladder, rendering these molecules as not useful for opto-magnetic Sisyphus cooling. Therefore the rest of this section we will focus exclusively on opto-electric Sisyphus cooling.

In order to make use of the vibrational angular momentum of linear triatomic molecules for opto-electric Sisyphus cooling, the FCFs are required to be diagonal such that the molecules remain in the vibrational bending mode throughout the cooling process. Following Kozyryev [146] we can estimate the respective FCFs, where e.g. the vibrational branching of the $\tilde{A}^2\Pi(0, 2^2, 0)$ excited state of SrOH can be calculated to be highly diagonal with FCF ≈ 0.95 and similar results are obtained for YbOH and CaOH. This allows to scatter ~ 20 photons before population is lost from the cooling cycle to higher vibrational levels. Due to the large energy removal for opto-electric Sisyphus cooling this can be enough to reach the ultracold temperature regime, however if more photons need to be scattered vibrational repump lasers can be added to the system, as in a standard laser cooling experiment. These molecules

are close to ideal, we can not only make use of the vibrational angular momentum of a linear triatomic molecule for opto-electric Sisyphus cooling but also utilise an electronic excited state to cool the polyatomic molecules and benefit from its large spontaneous decay rate.

In the example illustrated in Figure 2.14 we assume the FCF to be one and the lifetime of the vibrational bending mode sufficiently long to cool the molecular sample to ultracold temperatures, such that the vibrational quantum numbers $(v_1, v_2^{|\ell|}, v_3)$ are the same in the ground and the excited state during the cooling process. Thus the only relevant aspect of the molecules vibrational state for the design of the cooling scheme is the impact of the vibrational angular momentum on the electronic and rotational structure of the molecule. The presence of vibrational angular momentum can change the character of the state, as it is no longer described by Λ but by $K = \Lambda + \ell$, for additional information we refer the reader to section 2.2.3. For the example depicted in Figure 2.14 we assume the molecule to be excited to the vibrational bending mode $v_2^{|\ell|} = 2^2$ such that the ground state can change it's character from $\tilde{X}^2\Sigma(0,0,0)$ to $\tilde{X}^2\Delta(0,2^2,0)$ (which has the character of a $^2\Delta$ electronic state of a diatomic molecule) while the Π-character of excited state $\tilde{X}^2\Pi(0,2^2,0)$ can remain unchanged with ℓ and Λ having two opposite senses of rotation. Typically the ℓ-doubling is in the MHz range and therefore orders of magnitude smaller than Λ- or Ω doubling, thus for molecules with $\Lambda = 0$ in the electronic ground state, many of the complications discussed in section 2.4.2 can be omitted. In this situation the Hunds's case (b) basis provides the best description, as spin-orbit interaction is not existent for molecules with $\Lambda = 0$. The rotational states are labelled with the quantum number $N \geq K$, where each N is split by the spin-rotation interaction into $J = N \pm 1/2$ for a molecule with spin $S = 1/2$. As discussed in section 2.4.3 already at moderate electric fields the different spin-rotation components can be coupled strongly so that the electric field response is characterised by N, M_N and J is no longer well defined. Each N-level consists of two nearly degenerate states, as depicted in Figure 2.14, with spin components $M_S = \pm 1/2$. Depending on the angular momentum coupling scheme of the excited state this can complicate the decay in the centre of the potential. If the excited state is most accurately described by a Hund's case (b) basis then the situation is unproblematic and the decay of N' is restricted according to $\Delta N = 0, \pm 1$ [13]. However if the excited state is best described by a Hund's case (a) coupling scheme, as depicted in Figure 2.14, the situation becomes more complex as J is not well defined in the ground state and N' is not defined in the excited state. If the spin-rotation components are coupled strongly by the applied electric field, then each N-level contains a superposition of both spin-rotation components $J = N \pm 1/2$. In combination with the selection rule $\Delta J = 0, \pm 1$ [13] a given excited state with a well defined value for J' and Ω' will decay to the four ground states $N = J' \pm 1/2$ and $N = J' \pm 3/2$. However we can make use of the vibrational angular momentum to restrict the number of decay channels, as illustrated in Figure 2.14. Using a vibrational mode with $\ell \geq 2$ provides the possibility to design a cooling scheme with a $\tilde{A}^2\Pi(0,2^2,0)$ ex-

cited and a $\tilde{X}^2\Delta(0, 2^2, 0)$ ground state, where in absence of rotational excitation, the angular momentum in the ground state ($K = 2$) is larger than in the excited state ($K' = 1$). For $K' = 1$ the state with minimal angular momentum is given by $J' = 1/2, \Omega' = 1/2$ for a Hund's case (a) basis and by $N' = 1, J' = 1/2$ for a Hund's case (b) basis. As the ground state can have $K = 2$ character, the lowest rotational level is $N = 2$ and it's spin rotation components $J = 5/2$ and $J = 3/2$ are the only possible decay channels of the $J' = 1/2$ excited state. Thus, we can design a cooling scheme where the excited states decays to a single rotational level and, as illustrated in Figure 2.14, for a sufficiently large offset field E_{off} the excited state decays to low-field-seeking states only. Kinetic energy is removed from the sample by transferring population from the $M_N = 2$ to the $M_N = 1$ level in the high-field region of the trap. In this example we utilise the offset field in the centre of the potential to achieve state selectivity to repump the $M_N = 0, 1$ state. As the dark state $|d\rangle$ to first order shows no electric field response fast repumping is required to avoid that population is lost from the cooling cycle. Furthermore we want to note that for the example illustrated in Figure 2.14 we assumed that the separation between the $N = 2$ and the $N = 3$ level of the ground state is large such that they are not mixed by the applied electric field, as this would create an additional decay channel to the $N = 3$ level. This represents a feasible cooling scheme for these types of molecules, and thereby allows the preparation of cold and ultracold samples of linear polyatomic molecules.

2.5 Example scheme CH

As illustrated in the previous sections molecules with inversion doublet in the ground state are promising candidates for a successful implementation of opto-electric or opto-magnetic Sisyphus cooling. As discussed in sections 2.4.1 and 2.4.4 symmetric top and linear triatomic molecules are in general well suited candidates due to the K-degeneracy or the possibility of exciting a bending vibrational mode, respectively. In contrast, only diatomic molecules with $\Lambda > 0$ in the electronic ground state possess inversion doublets and are promising candidates. Although the majority of diatomic molecules that have been directly cooled to ultracold temperatures occur in a Σ ground state with $\Lambda = 0$ there are many examples for diatomic molecules that are potentially well suited for opto-electric or opto-magnetic Sisyphus cooling, including CH, OH, NO, NH, SH [13] with a range of interesting properties including time-variation of fundamental constants [158], chemical reactions[159] or astronomy [160].

In the following we will apply the concepts introduced in the previous sections exemplary to the diatomic radical molecule CH, that has a $A^2\Delta(v' = 0)$ electronic excited and a $X^2\Pi(v = 0)$ electronic ground state [158]. In contrast to the example schemes depicted so far, where we used frequency selectivity in the centre of the trap to distinguish states, CH is in particular well suited to illustrate how to utilise

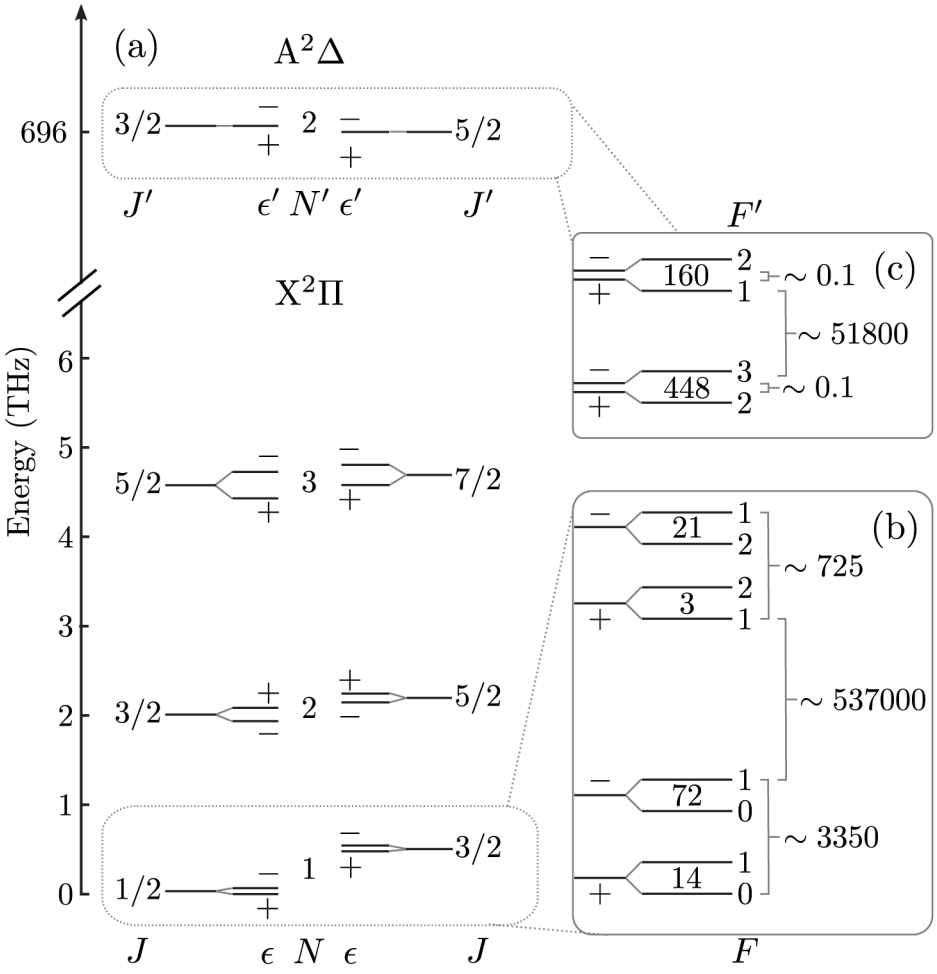

Figure 2.15: *(a) Zero-field energy spectrum of the electronic $X^2\Pi(v = 0)$ ground and $A^2\Delta(v' = 0)$ excited state of CH, with the rotational levels drawn to scale, while the parity doublets were exaggerated by a factor of 20. The ground and the excited state are best described by Hund's case (b), thus the rotational levels are labelled by N. (b) Zoom into the $N = 1$ level of the ground state and (c) the $N = 2$ level of the excited state to depict the hyperfine structure and the magnitude of the inversion doublets.*

the amplitude of the various Stark shifts to achieve state selectivity as introduced in 2.3.1. CH has a Franck-Condon factor of FCF= 0.99 [161], which enables us to utilise an electronic excited state with a spontaneous decay rate of $\Gamma = 2\pi \times 0.3$MHz [162]. The resulting fast photon cycling rate has the advantage that a successful implementation of opto-electric Sisyphus cooling is possible even if population decays to high-field-seeking states. Transitions between electronic ground state levels and the excited state, given by $|\epsilon' = -, N' = 2, |\Lambda'| = 2, J' = 3/2, M'_J = 3/2\rangle$ in the zero-field basis, are driven by $\lambda = 431$nm light [163]. The zero-field energy level structure of the relevant rotational states for cooling is depicted in Figure 2.15 (a), where the

spacing between the individual rotational levels is drawn to scale but the magnitude of the Λ-doublets is exaggerated by a factor of 20. Both the electronic excited as well as the electronic ground state are most accurately described by a Hund's case (b) basis, $|\epsilon, N, |\Lambda|, J, M_J\rangle$, so that the rotational levels are labelled by the quantum number N, as introduced in section 2.2.2. Due to an electronic spin of $S = 1/2$ each rotational level is split by the spin-rotation interaction into two components, given by $J = N \pm 1/2$. Furthermore, the degeneracy of $\pm\Lambda$ in the electronic ground and excited state is lifted by rotational and spin-orbit interaction, such that each J state is split into two opposite parity components. In addition the interaction with the nuclear spin $I = 1/2$ causes each Λ-doublet component to split into multiple hyperfine levels described by the quantum number F and is illustrated for $N = 1$ of the ground state and $N' = 2$ of the excited state in Figure 2.15 (b) and (c), respectively.

Cooling of CH is in many respects similar to the idealised example depicted in section 2.4.2, with the distinction that CH is well approximated by a Hund's case (b) coupling scheme. Consequently the selection rules for an electronic transition are given by $\Delta N = 0, \pm 1$ and $\Delta J = 0, \pm 1$ [13], as the spin-rotation interaction is large enough such that J remains well defined for typical offset fields E_{off}. In contrast, for $E_{\text{off}} = 2.0\text{kV/cm}$, F is no longer well defined, as the nuclear spin of the excited state and the ground state levels, depicted in Figure 2.16 (a) and (b), is uncoupled from J. Moreover, the offset field fully mixes the opposite parity components of the inversion doublets of the excited state, as they are only separated by about 0.1MHz. In contrast for the rotational levels of the ground state, depicted in Figure 2.16, the magnitude of the Λ-doublet varies between 725MHz and 14.9GHz, such that the field in the centre of the trap is not sufficient to fully mix the opposite parity states of all rotational levels. Thus, as depicted in Figure 2.16 (a), decay to low-field and high-field-seeking states is possible, but this does not exclude a successful cooling scheme due to the large spontaneous decay rate of the electronic excited state, which allows repumping of high-field seeking states before they are lost from the trap.

Figure 2.16 (b) shows the Stark shifts of the excited state and the ground states $|e\rangle$ can decay to, where the low-field-seeking states of the $N = 1, J = 3/2$ and of the $N = 2, J = 3/2$ level are both suited candidates for $|s\rangle$ and $|w\rangle$, with a maximum energy removal of 11.4GHz and 11.0GHz per cooling cycle, respectively. In addition to the large differential Stark shifts both rotational levels also fulfill the requirement that population transferred from $|s\rangle$ to $|w\rangle$ in the high-field region of the potential remains well trapped. In order to select which of the two rotational levels should be used for the primary Sisyphus transfer we need to consider the temperature of the molecular sample as well as the size of the inversion doublets in combination with the applied offset field E_{off}, as described in section 2.4.2. At zero electric field the inversion splittings of the $N = 1, J = 3/2$ and the $N = 2, J = 3/2$ levels have a magnitude of 725MHz and 7.4GHz, respectively. Thus, to transfer population from $|s\rangle$ to $|w\rangle$ in the high-field region of the trap at transition frequencies larger than 7.4GHz, the $N = 1$ level has to be used. This ensures that transitions from

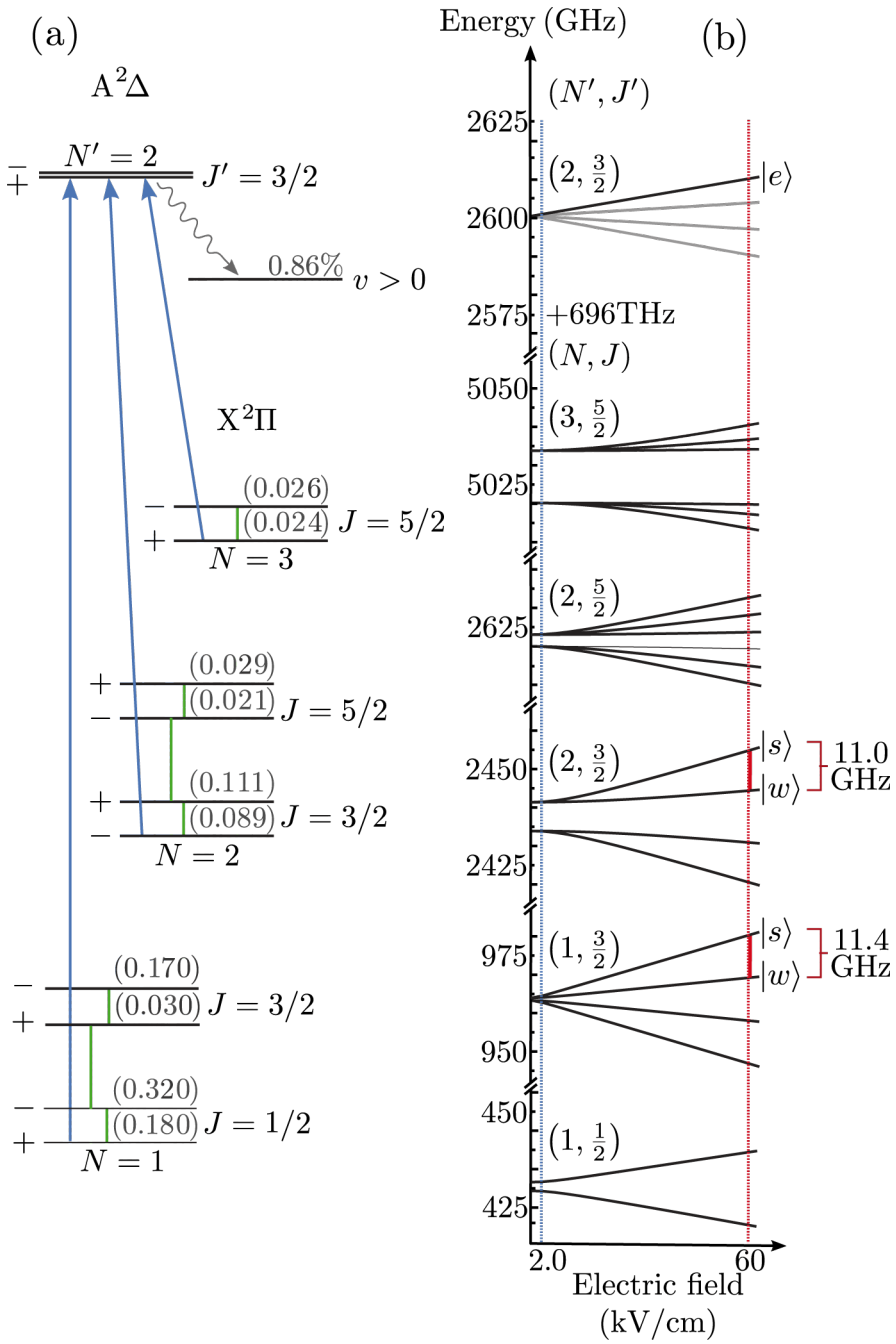

Figure 2.16: *(a) Rotational branching of $|e\rangle$ at an applied offset field of $E_{off} = 2.0 kV/cm$, indicated by the dashed blue vertical in (b). (b) Stark shifts of the relevant levels for opto-electric Sisyphus cooling of CH. A good choice for the excited state is the $N' = 2, J' = 3/2$ rotational level and depending on the temperature of the molecular sample, either the low-field-seeking states of the $N = 2, J = 3/2$ or the $N = 1, J = 3/2$ level of the ground state can be used for $|s\rangle$ and $|w\rangle$*

the $M_J = 3/2$ level to high-field seeking states are sufficiently suppressed by the applied electric field, as introduced in section 2.4.2. In contrast for the $N = 2$ level the magnitude of the inversion splitting is too large to fully mix the associated opposite parity states for most of the trapping fields. Consequently transitions from $|s\rangle$ to the high-field-seeking component of the Λ-doublet are possible anywhere in the trap where the associated energy separation is on resonance with the radiation supposed to drive $|s\rangle \rightarrow |w\rangle$ in the high-field region. With the molecules getting colder during the cooling process the transition frequency in the high-field region has to be reduced accordingly. Thus for transitions frequencies of $\sim$ 7GHz or lower the $N = 2$ level becomes well suited for the primary Sisyphus transfer. This is due to the fact that transitions to the high-field-seeking component of the Λ-doublet in the low-field region of the trap can not take place as the magnitude of inversion splitting is larger than the frequency of the light field. The already mentioned reduction of the transitions frequency during the cooling process is accompanied by the fact that the population transfer happens at lower electric fields. Consequently the $N = 1$ level becomes less suited as the inversion doublets are no longer fully decoupled for sufficiently low electric fields and population transfer to high-field-seeking states becomes more likely. However, if the transition frequency is below $\sim$ 700MHz, the $N = 1$ level is again well suited, as the transition frequency is smaller the then 725MHz splitting between the opposite parity states of the inversion doublet. At this point we want to mention that the exact frequency cutoffs can of course deviate from the numbers given in this paragraph, as they depend on the applied offset field.

State selectivity is a key requirement for a successful implementation of an opto-electric or opto-magnetic Sisyphus cooling scheme. Of particular relevance is the ability to repump all decay channels of $|e\rangle$ in the low-field region of the trap without addressing $|s\rangle$. In the following we will demonstrate how to utilise the amplitude of the Stark shifts of the ground states and the excited state to achieve the required states selectivity for CH. We start with a simplified example using the rotational levels $N = 1, J = 3/2$ of the electronic ground and $N' = 2, J' = 3/2$ of the electronic excited state of CH to introduce the basic concepts. The electric field response of both states is illustrated in Figure 2.16 (b) and in a more compact form in Figure 2.17 (a). We assume the offset the field in the centre of the trap to be sufficiently large to suppress decay to high-field seeking states, such that $|e\rangle$ can only decay to $|s\rangle$ and $|w\rangle$ for the example shown in Figure 2.17 (a) and (b). In order to make use of the amplitude of the different Stark shifts to achieve state selectivity we need to consider the electric field dependence of the corresponding transition frequencies. This is illustrated in Figure 2.17 (b) for all dipole allowed transitions of the $|s\rangle$ and $|w\rangle$ state. The color code illustrates the M_J-level of the ground state involved in the transition, where red and blue indicate transitions including the $M_J = +1/2$-level and $M_J = +3/2$-level, respectively. By choosing the detuning of the repumping light field as indicated by the dashed orange line, we couple $|w\rangle$ back to the excited state without addressing $|s\rangle$. Thus, just by using the different amplitudes of the Stark shifts of the excited state and the ground state in combination with suited

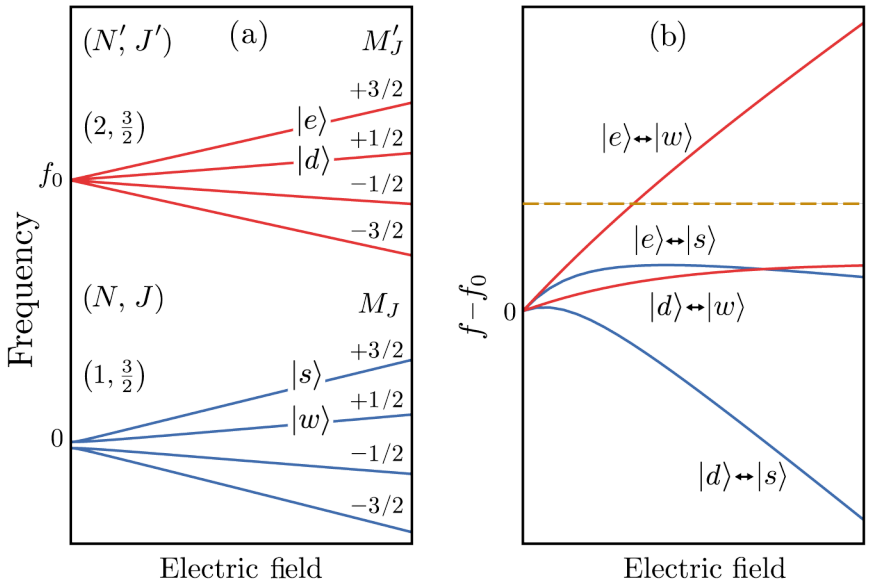

Figure 2.17: *(a) Electric field response of the $N' =, J' = 3/2$ and the $N = 1, J = 3/2$ level of the electronic excited and ground state, respectively. (b) Electric field dependence of the transition frequency between electronic ground and excited state, introduced in (a). The line color indicates the ground state involved in the transitions, with red: $M_J = +1/2$ and blue: $M_J = +3/2$. The dashed orange line depicts a a suited detuning of the light field to couple $|w\rangle$ to $|e\rangle$, without addressing $|s\rangle$.*

detuning of the light field we achieve the required state selectivity. We want to emphasize that the example, depicted in Figure 2.17 (b), is simplified as we did not consider hyperfine structure and more importantly we assumed that decay to high-field-seeking states is suppressed by the applied offset field.

Including these complications increases the complexity of the system significantly, as can be seen in Figure 2.18 (a) and (b), showing the electric field dependence of the transition frequencies between the $N' = 2, J' = 3/2$ level of the electronic excited state and the $N = 1, J = 3/2$ and $N = 2, J = 3/2$ levels of the electronic ground state, respectively. To successfully apply opto-electric Sisyphus cooling to CH, state selectivity is only required for these two ground state levels, as they are the only suited candidates for the primary Sisyphus transfer for the example scheme depicted in this section. For the other decay channels of $|e\rangle$ repumping can be simply achieved by coupling the individual rotational levels to the excited state using microwave and laser radiation, as illustrated in Figure 2.16 (a). Identical to the simplified example depicted in the previous paragraph, in Figure 2.18 (a) and (b), we use the line color to indicate the M_J level of the ground state involved in the transition (blue: $M_J = 3/2$, red: $M_J = 1/2$, black: $M_J = -1/2$ and green: $M_J = -3/2$).

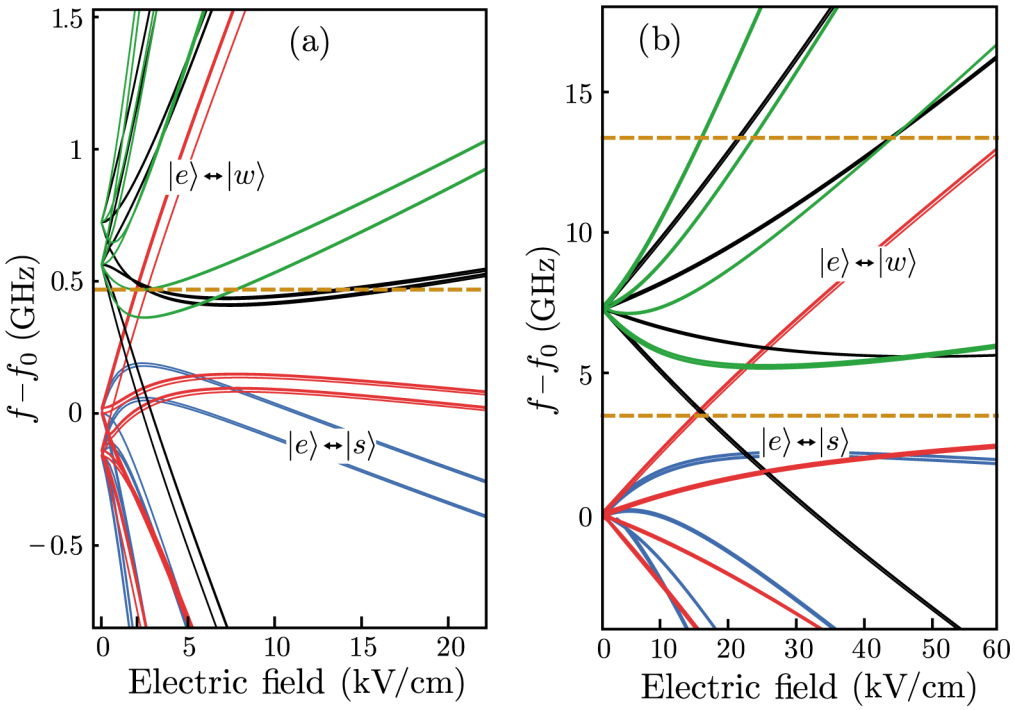

Figure 2.18: *Electric field dependence of all dipole-allowed transition frequencies between the individual M-states of the $N' = 2, J' = 3/2$ level of the electronic excited state and the (a) $N = 2, J = 3/2$ and (b) $N = 1, J = 3/2$ level of the electronic ground state, respectively. Each M_J level is associated with multiple hyperfine states. The color code labels the M_J level of the ground state inolved in the transition, with blue: $M_J = 3/2$, red: $M_J = 1/2$, black: $M_J = -1/2$ and green: $M_J = -3/2$. The orange dashed line indicates a suited detuning for the repumping light field.*

For the $N = 1, J = 3/2$ level, illustrated in Figure 2.18 (a), transitions to $|s\rangle$ can only occur up to detunings of 190MHz, whereas all the other M_J levels of the ground state can be addressed with larger positive detunings, providing the required state selectivity. Using an offset field of $E_{\text{off}} \approx 2.0$ kV/cm and a detuning of ~ 470MHz, indicated by the dashed orange line in Figure 2.18 (a), couples the different hyperfine components of $|w\rangle$ to the excited state at electric field values of about 2.0kV/cm and 2.6kV/cm. At similar field strengths transitions with $M_J = -1/2$ and $M_J = -3/2$ can be driven, such that all possible decay channels except for $|s\rangle$ are repumped in the low-field region of the trap. Using a detuning of about 470MHz has an additional advantage, as the $|w\rangle$ state is solely driven in the low-field region of the potential. This is important as additional driving of the $M_J = 1/2$ level at larger electric fields sets an upper bound to the initial kinetic energy of the molecules.

At this point we want to note that by making use of the electric field dependence of the transition frequencies in combination with a detuned light field unintentional population of other M'_J states within the rotational level of the excited state $|e\rangle$ can

often not be avoided. However, except for altering the branching ratio to $|s\rangle$, this does not affect the cooling scheme as all high- and low-field-seeking components of the ground state are repumped with this technique anyways.

For the example shown in Figure 2.18 (a) coupling to $M'_J = -1/2$ and the $M'_J = -3/2$ of the excited state is possible for radiation with a detuning of ~ 470MHz via the high-field-seeking ground states $M_J = -1/2$ and the $M_J = -3/2$. However, at an offset field of $E_{\text{off}} \approx 2.0$ kV/cm the opposite parity states of the inversion doublet of the $N = 1, J = 3/2$ level are already fairly well mixed, as they are only separated by 725MHz, such that transitions to these high-field-seeking states are possible but strongly suppressed. Only about 1% and 2% of the population in $|e\rangle$ decays to the hyperfine components of the high-field-seeking $M_J = -3/2$ and $M_J = -1/2$ state, respectively. However, as already mentioned, the repumping light couples these states not to $|e\rangle$, but to the $M'_J = -1/2$ and the $M'_J = -3/2$ level, causing a reduction of the branching ratio to $|s\rangle$ from 11% to 9%. By choosing an offset field significantly larger than $E_{\text{off}} \approx 2.0$ kV/cm decay channels to high-field-seeking states are suppressed even further such that repumping of the $M_J = -1/2$ and the $M_J = -3/2$ levels is no longer required and consequently the $M'_J = -1/2$ and the $M'_J = -3/2$ are not populated any longer. In this situation the repumping scheme strongly resembles the idealised example depicted in Figure 2.17 (b).

The second rotational level with suitable states for $|s\rangle$ and $|w\rangle$ is $N = 2, J = 3/2$, possessing a ten times larger inversion splitting than the $N = 1, J = 3/2$ level. Thus, for reasonably large electric fields in the centre of the potential, it is not possible to fully mix the opposite parity states of the inversion doublet to exclude decay to high-field-seekers. However as we address all low-field- and high-field-seeking M_J states of the $N = 2, J = 3/2$ level, except for the $|s\rangle$ state, with the repumping light field, as illustrated in Figure 2.18 (b), we can also utilise this rotational level for cooling. Driving the $|s\rangle$ state is only possible up to detunings of about 2GHz, whereas all the other M_J states of the $N = 2, J = 3/2$ level of the electronic ground states can be coupled to the $N' = 2, J' = 3/2$ level of the excited state with larger positive detunings. Thus the required state selectivity can be achieved, e.g. by using light fields with detunings of ~ 3.6GHz and ~ 13.3GHz, as depicted by the two dashed orange lines in Figure 2.18 (b). These light fields drive the $M_J = 1/2$, $M_J = -1/2$ and the $M_J = -3/2$ level at an electric field of about 15kV/cm, without additional driving of $M_J = 1/2$ for field strengths of more than 60kV/cm. A disadvantage of this repumping scheme is that the transitions occur at a comparably large electric field of 15kV/cm. At this field strength molecules in the $M_J = 3/2$ state have a potential energy of about 100mK, which limits the minimal achievable temperature as the potential energy is converted into kinetic energy when the molecules move towards lower electric fields in the trap . In principle this problem can be solved by applying an offset field of $E_{\text{off}} = 15$kV/cm, however an experimental realisation of such a large offset field can be quite challenging for many trap designs. In order to reach lower temperatures one can couple the $N = 2, J = 3/2$ ground state to the $N' = 2, J' = 3/2$ level of the excited state at a field strength of 9kV/cm, where

the potential energy of molecules in the $M_J = 3/2$ state is just slightly higher than 40mK. Therefor radiation with detunings of of 2.2GHz, 9.8GHz and 10.2GHz have to be utilised to drive transitions with the $M_J = 1/2$, $M_J = -1/2$ and the $M_J = -3/2$ level, respectively. As radiation with a detuning of $\sim$ 10GHz will also drive $M_J = 1/2$ transitions at electric fields of 44kV/cm this coupling scheme only works for molecules with sufficiently low kinetic energy.

Chapter 3

Observation of electric field dependent collisions – dipolar relaxation

The rapid progress in the field of cold and ultracold molecule research in recent years allowed both opto-electric Sisyphus cooling and direct laser cooling to prepare samples of ultracold molecules [21, 18], where the to date lowest temperatures (few μK) of directly cooled molecular samples were obtained utilising laser cooling techniques [121, 20, 122]. Since it is unlikely to lower the temperature of the molecular samples further using direct laser cooling [77], collision studies become increasingly important. They provide insights into and control over elastic and inelastic scattering rates a prerequisite for successful evaporative or sympathetic cooling [62, 164] to further increase the phase space density of the molecular samples and eventually approach quantum degeneracy [77]. In this chapter we present electric field controlled collision studies between cold polyatomic molecules in an electric trap. The record high flux of cold, slow and dense molecular samples produced by the Cryofuge [78], enables us to directly observe dipolar collisions between trapped polyatomic CH_3F molecules. A semi-classical model, showing excellent agreement with the measured data, allows us to identify the main collisional loss mechanism in our system, dipolar relaxation to untrapped states. By tuning an external electric field we can reduce the inelastic collisonal loss by a factor of two without altering the thermalising elastic collisions, a prerequisite for potential future evaporative cooling experiments.

In section 3.1 we illustrate the experimental set-up used for the collision measurements. The basic concepts of buffergas cooling are introduced in 3.1.1 as well as electrostatic guiding and centrifuge deceleration in 3.1.2. The microstructured electric trap is presented in section 3.1.3, before we end the experimental set up section by introducing our detection method in 3.1.4. The collision measurements are presented in section 3.2, starting with a description of the measurement scheme in 3.2.1, followed by the velocity and state distribution measurements in 3.2.2 and 3.2.3, respectively. In the subsequent section 3.2.4 we present the observation of col-

lisions between trapped molecules, before we show how to extract the two-body loss rate k from the collision measurements in 3.2.5. In the last section of this chapter 3.2.6 we show the electric field dependence of the collision process that we utilise to suppress inelastic losses. In addition we also introduce a semiclassical theory describing the collision process in our trap, showing excellent agreement with the measured data.

3.1 Experimental set up - the cryofuge

The starting point of our collision experiment is our unique molecular source, dubbed cryofuge [78], schematically illustrated in Figure 3.1. It combines cryogenic buffergas cooling [61] with centrifuge deceleration [112] to produce a continues high density flux of cold molecules below kinetic energies corresponding to 1K [78]. This allows us to trap the molecular sample in our microstructed electric trap [65] to perform collision studies between cold polar molecules, which we detect using a quadrupole mass spectrometer (QMS).

3.1.1 Cryogenic buffergas cooling

Buffergas cooling is a frequently used technique in the field of cold and ultracold molecules [89, 90, 91] since it allows cooling of the internal and external degrees of freedom of the molecules regardless of their complex internal structure [165, 91]. The working principle is robust and general; it relies on sympathetic cooling of warm molecules using cold buffergas atoms [92]. Warm molecules flow into the cell which is cooled to a few Kelvin. The buffers atoms (e.g. helium) are thermalised to the temperature of the cell, which can be as low as the atoms' condensation point. The buffergas atoms collide with the warm molecules allowing them to thermalise to the cell temperature [92] such that a beam of cold molecules exits the cell.

We distinguish between three regimes [166] of buffergas cooling, the effusive, the boosted and the supersonic regime, which depend on the flow rate of the molecules and density of buffer gas atoms in the cell. A schematic illustration of the three regimes is shown in Figure 3.2 (a) - (c). In the effusive regime the buffergas density is low such that the mean free path of the molecules is much larger than the exit hole diameter $\lambda \gg d$ [167]. The movement of the molecules through the cell resembles a random walk, where they either reach the exit hole and leave the cell or they freeze to the cell wall [167]. However the intensity of the molecular beam exiting the cell is low. In the effusive regime molecules undergo less then one collision with buffergas atoms in the vicinity of the exit hole. In contrast, in the boosted regime, shown in Figure 3.2 (b), where $\lambda < d$ [167], molecules collide on average more than once with buffergas atoms at the exit hole. This leads to boosting and acceleration of the molecules out of the cell. In the supersonic regime, depicted in Figure 3.2 (c), the buffergas density is so high that the mean free path of the molecules is smaller

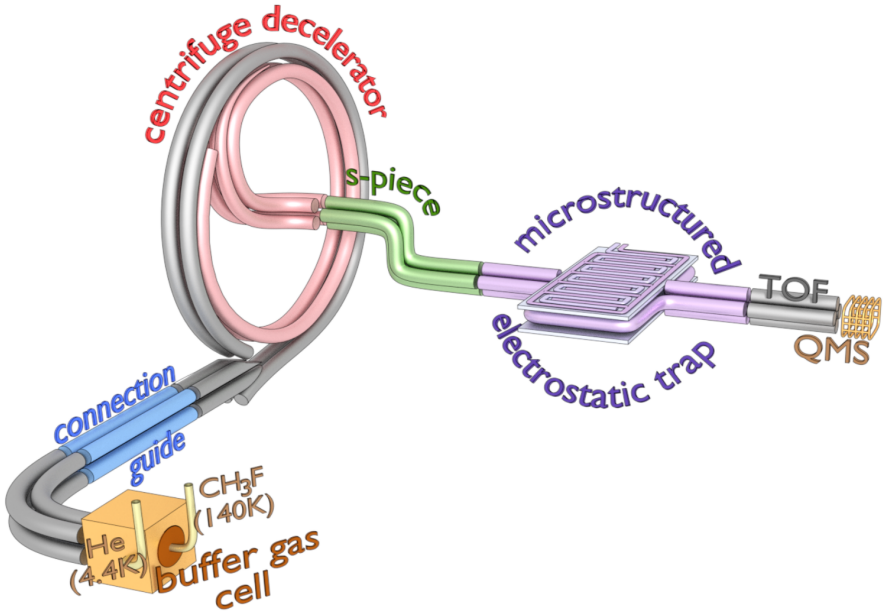

Figure 3.1: *Schematic illustration (not to scale) of the experimental setup. The starting point is the buffergas cell operated at 4K with He buffergas atoms. To prevent freezing of CH_3F molecules, the molecule line is actively heated to 140K. The centrifuge is attached to the buffergas cell via a 90° bent quadrupole guide and a straight piece of guide, dubbed connection guide. The microstructured electrostatic trap is connected to the exit of the centrifuge decelerator via a s-shaped electrostatic quadrupole guide. Molecules are unloaded from the trap using the time of flight guide (TOF) and detected by a quadrupole mass spectrometer (QMS).*

than the exit hole diamter, $\lambda \ll d$ [167]. In this regime the cell dynamics are most accurately described by a macroscopic flow through the cell, where the molecules undergo adiabatic expansion at the cell exit [167]. For all measurements presented in this thesis we operate our buffergas cell in the boosted regime, since it provides the most intense beam of cold molecules in our experiment that can be decelerated and trapped.

Our molecule of choice is the symmetric top molecule CH_3F and a detailed theoretical description of symmetric top molecules can be found in section 2.2.1. In the buffergas cell the CH_3F molecules are sympathetically cooled by He atoms. Both species come from gas bottles attached to the molecule and buffergas line, respectively. The inflow into the cell is regulated using a Alicat MCS and a Alicat MC flowmeter for the molecules and for the buffergas, respectively. Our buffergas cell as well as the buffergas and the molecule line are made out of oxygen free copper. The cell is mounted to the second cooling stage of a Cryomech PT420 pulse tube cooler, allowing us to reach temperatures down to 4K. To shield the buffergas cell from black body radiation we mount gold coated copper radiation shields to the first

and second cooling stage of the pulse tube cooler [168]. The inside of the radiation shield mounted to the second cooling stage is coated with charcoal to ensure efficient pumping of the helium buffergas atoms leaving the cell [169]. By actively heating the molecule line to 140K we prevent clogging of the copper tube due to freezing of CH_3F molecules. However freezing can not only occur at the molecule line but molecules can also stick to the cell walls or clog the exit hole. This limits the operation time of the buffergas cell to 2.2 hours for the measurements shown in this thesis. Afterwards the cell is automatically heated and cooled down in a $\sim$ 5 hour cycle allowing us to have three measurement cycles per day.

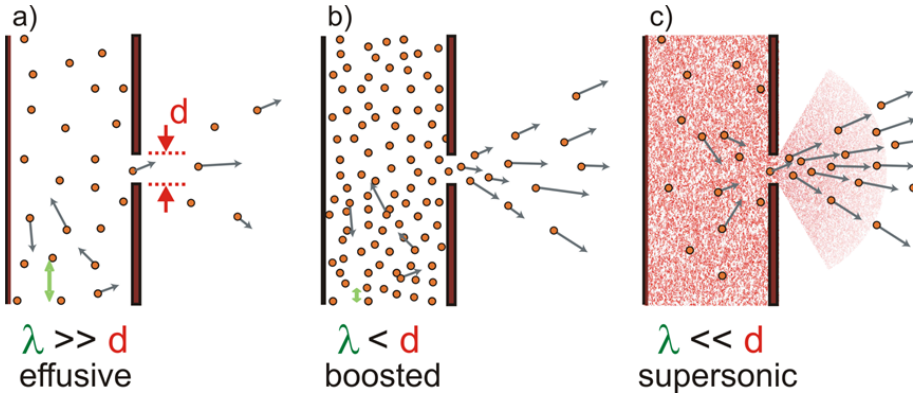

Figure 3.2: *Schematic illustration of the (a) effusive, (b) boosted and (c) supersonic regime of buffergas cooling. The mean free path of the molecules is labelled as λ and the diameter of the cell exit hole is denoted with d. We operate our cell in the boosted regime, shown in (b). The Figure is adapted from [167].*

3.1.2 Electrostatic Guiding and Centrifuge deceleration

When studying molecule-molecule collisions it is of great importance to have long interaction times and a controlled environment [78, 164]. Thus the obvious conclusion would be to load the molecules directly from the buffergas cell into a trap. However the boosting effect [170] at the cell exit accelerates the molecules such that it is impossible to directly trap the molecules after the buffergas cell, instead we need to filter out the fastest molecules and decelerate the molecular beam. In our experiment both techniques require electrostatic guiding [92, 90].

Due to the favorable dipole-to-mass ratio together with a linear electric field response, CH_3F is perfectly suited for electrostatic trapping and guiding. Figure 3.3 (a) shows a schematic illustration of a linear electric field response with low- and high-field-seeking states. A low-field-seeking state is characterised by the molecule's dipole moment being anti-aligned with the applied electric field and its potential energy is minimal at an electric field minimum [114]. In contrast, for a high-field-seeking state the potential energy is maximum at an electric field minimum and the

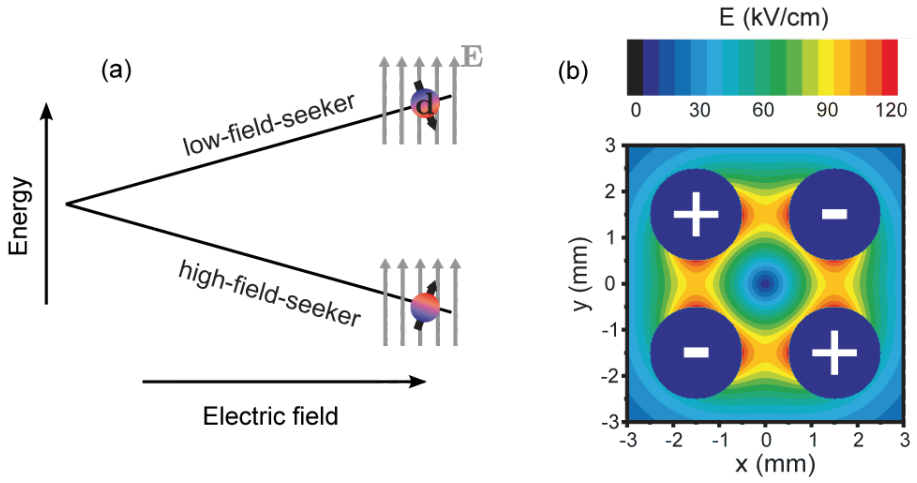

Figure 3.3: *(a) Schematic illustration of the electric field response of a low-field- and a high-field-seeking state. (b) Electric field distribution of a quadrupole guide. The Figure is adapted from [171].*

molecules dipole moment is aligned with the external electric field [114]. To trap and guide molecules they need to be in a low-field seeking state.

In our experiment the electrodes of the guides are arranged in a quadrupole shape, illustrated in Figure 3.3 (b), providing an electric field minimum at the centre surrounded by a radially increasing large trapping field [171]. Hence in a straight piece of guide molecules can move freely in the longitudinal direction but are confined transversely by the trapping potential (x- and y-direction in Figure 3.3 (b)). However we can also filter the longitudinal velocity component v_z with a bend quadrupole guide [133], as it is used in our experiment after the buffergas cell. Here molecules are lost if the centrifugal force, given by $F_{\text{centr}} = mv_z^2/R$, where m is the mass, v_z the longitudinal velocity of the molecule and R the radius of the bend guide, exceeds the restoring force of the guiding field. By controlling the voltage on the electrodes, we can control the guiding field, and therefore the longitude cut-off velocity. In our experiment the bend radius of the guide after the buffer gas cell is chosen to be identical with the radius of the centrifuge decelerator ($R = 20$cm). This ensures that all molecules that can be decelerated make it to the centrifuge and all other molecules that could lead to collisional loss in the connection guide are filtered out.

Ideally, the deceleration technique will be both continuous and generic. The continuous aspect allows for efficient use of the molecules continuously exiting the buffergas cell, while being generic allows us to study a broad range of molecular species and maintain the generality of our experiment. Both aspects are full filled with the centrifuge decelerator [112], illustrated in Figure 3.1. In the following we will only provide a brief overview of the concept and the design of the centrifuge. For more information we refer the reader to [112, 113].

The basic principle of deceleration is to transfer kinetic into potential energy.

For the centrifuge this is realised via the centrifugal potential $E_{cent} = -\frac{m}{2}(\vec{\Omega} \times \vec{r})^2$ [112], where m is the mass of the molecule, $\vec{r}$ the distance from the rotation axis and $\vec{\Omega}$ the rotation speed of the centrifuge. It allows continuous deceleration of molecules, where the height of the potential hill and thereby the amount of kinetic energy removed from the particles, can be adjusted by $\vec{\Omega}$ according to the buffergas cell settings and the molecule properties. Transversal confinement of the molecules during the deceleration process is provided by electrostatic guiding [113]. This makes centrifuge deceleration a versatile technique, applicable to large variety of molecules, since it only requires them to be electrostatically guideable and not too heavy. One of these molecules is our molecule of choice, the symmetric top CH_3F, perfectly suited due to its permanent electric dipole moment and linear electric field response.

As depicted in Figure 3.1, after exiting the buffergas cell molecules are electrically guided via a 90° bent quadrupole guide and a straight piece of guide, dubbed connection guide, to the centrifuge decelerator. Molecules enter the centrifuge via the injector and are guided by the static electrode depicted in yellow in Figure 3.4 (a) together with the rotating spiral electrodes in blue and red towards the access point of the rotating electrodes [112]. After entering the rotating spiral guide molecules climb up the centrifugal potential hill when moving from the periphery to the centre of the decelerator and thereby lose kinetic energy [113]. As depicted in Figure 3.4 (a) at the exit of the centrifuge the molecular beam is velocity filtered by a bent quadrupole guide of radius $R = 5$cm.

To perform collision studies between trapped molecules it is of special importance that the density of the trapped ensemble is large such that interactions between the molecules are frequent [78, 62]. The deepest, experimentally realisable, traps require molecules to have kinetic energies below $1K \times k_B$ [65, 64, 62], equivalent to 22m/s for CH3F. In order to maximise the flux of trappable molecules out of the centrifuge it is important to consider its acceptance window of the input velocity distribution. Molecules that are not within the acceptance window are either not energetic enough to overcome the potential hill and therefore do not reach the exit of the centrifuge or if the molecules kinetic energy is too high they cannot be trapped after deceleration [113]. Since the width of the acceptance window is only a few m/s [113] the temperature of the buffergas cell is crucial. Figure 3.4 (b) illustrates Maxwell-Boltzmann distributions for the longitudinal velocity component of molecules leaving the buffergas cell, thermalised to 4K, 7K and 20K, including boosting effects [170] at the buffergas cell exit. The dashed grey area depicts the acceptance window of the centrifuge. Its centre position can be shifted to higher or lower velocities by tuning the rotation speed Ω of the centrifuge [112]. By reducing the buffergas cell temperature the width of the Maxwell-Boltzmann distribution gets narrower [133] and thereby the fraction of molecules within the acceptance window increases and thus also the number of trappable molecules. Therefore it is important to reach the lowest possible temperature for the buffergas cell to maximise the number of trappable molecules. Although not discussed in this thesis, by carefully

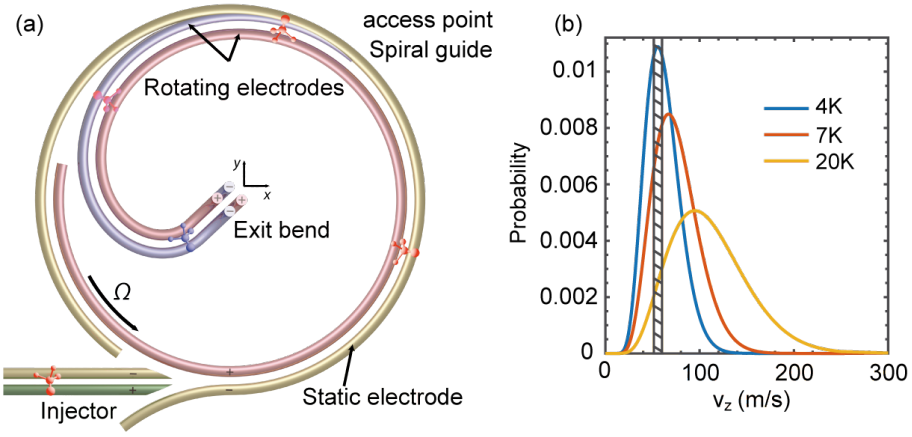

Figure 3.4: *(a) Top view of the centrifuge decelerator, adapted from [113]. Molecules enter the centrifuge via the injector and are electrically guided towards the spiral guide access point where they enter the rotating electrodes. After being decelerated the molecules leave the centrifuge out of the plane at the exit bend. (b) Boosted Maxwell-Boltzmann distributions of the longitudinal velocity component v_z for the three different buffergas cell temperatures $4K$, $7K$ and $20K$. The dashed are illustrates the acceptance window of the centrifuge for a given rotation frequency Ω.*

minimising the heat load on the buffer gas cell in our experiment the temperature of the cell was improved from 7K to 4K creating an increase in flux of about a factor of four.

3.1.3 Microstructured electrostatic trap

As illustrated in Figure 3.1 the centrifuge decelerator is connected to the microstructured electric trap by a s-shaped quadrupole guide to filter out fast molecules with kinetic energies above the acceptance window of the trap and to avoid collisional loss of slow trappable molecules moving from the centrifuge to the trap.

Figure 3.5 (a) and (b) show a graphic illustration of the electric trap consisting of two microstructured capacitor plates separated by a distance of 0.3cm [65]. A voltage difference $\pm V_\mu$ is applied to neighboring electrodes of the microstructure creating the trapping field at the edge of the trap [172]. We apply a voltage of $\pm V_\mu = 1200$V to the microstructure electrodes resulting in a maximum trapping field of $E_{\text{trap}} = 40$kV/cm. To achieve three dimensional confinement the trap is surrounded by a perimeter electrode, the ring electrode [172]. We obtain a maximum in trapped signal when applying $V_{\text{ring}} = 3V_\mu$ to the perimeter electrode. In addition to the large trapping field at the edge of the trap we can also apply voltages $\pm V_{\text{off}}$ to the capacitor plates resulting in a homogeneous offset field E_{off} at the centre of

the trap, necessary to suppress trap losses due to Majorana tranisitons [64, 65]. The large trapping field E_{trap} decays exponentially from the microstructured electrodes towards the centre of the trap [172] and thereby does not affect the homogeneous offset field. Thus in total our electric trap provides a box like potential with a tunable offset field E_{off} in the centre and a steeply rising trapping field E_{trap} towards the edge of the trap [172]. This allows us to trap CH_3F molecules with kinetic energies up to $1\text{K}\times k_B$.

In this thesis we apply offset voltages between $V_{\text{off}} = 0.05V_\mu$ and $V_{\text{off}} = 0.30V_\mu$ resulting in offset fields of $E_{\text{off}} = 0.50\text{kV/cm}$ and $E_{\text{off}} = 2.37\text{kV/cm}$, respectively. A simulation of the corresponding electric field distributions in the trap are shown in Figure 3.5 (c), with two clearly distinct peaks located at the applied trap offset fields. The simulated field distributions are obtained by rescaling the original simulations performed by Martin Zeppenfeld [172] to our experimental settings.

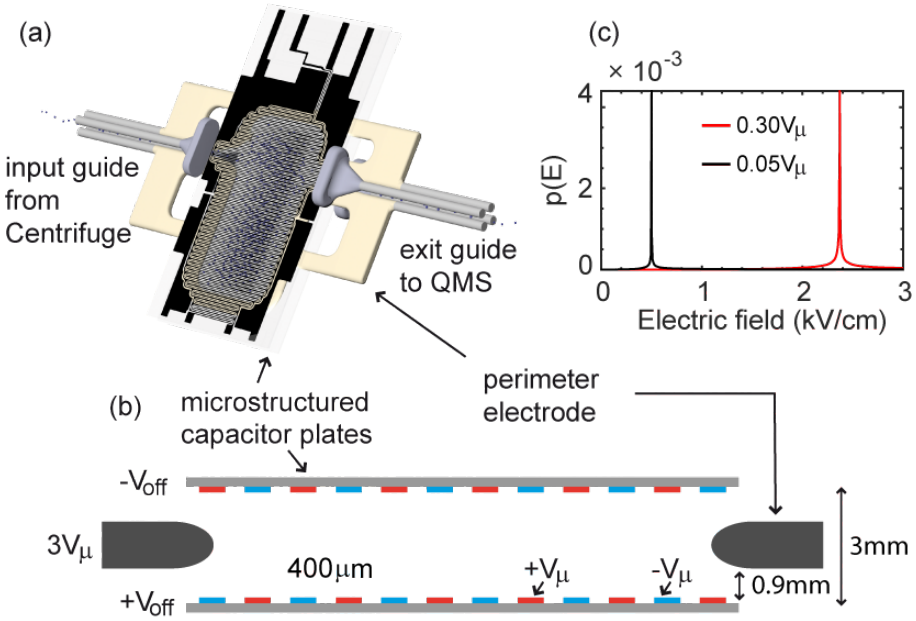

Figure 3.5: *(a) Graphic illustration of the microstructured electrostatic trap, adapted from [173]. (b) Schematic drawing of a cross-section through the trap perpendicular to the guide axis, taken from [65]. The trap consists of a pair of microstructured capacitor plates and a surrounding perimeter electrode. (c) Simulated electric field distribution for the two trap offsets $V_{off} = 0.30V_\mu$ and $V_{off} = 0.05V_\mu$.*

Molecules are lost from the trap via black-body radiation, collisions with background gas and Majorana transitions, but mostly via holes in the potential [172]. These have a non-trivial dependence on velocity with the loss rate through these holes being proportional to v^5 [172] for molecules with a linear Stark shift. Although the kinetic energy of the molecules is below the trap depth, single-body trap losses are more pronounced for fast than for slow molecules [174]. Fast molecules sample

trap regions where losses can occur, like the exit or the input hole or low electric field regions prone to Majorana losses, more frequently than slow molecules. This results in a non-trivial single-body loss rate that changes as a function of time as the velocity distribution changes throughout the trapping time. This will be important later on when we study two-body collision processes in Chapter 3.2.1.

Figure 3.6 shows trap lifetime measurements, recording the trap unloading signal as a function of the storage time for the connection guide voltages $V_{\text{conn}} = 200\text{V}$ and $V_{\text{conn}} = 2000\text{V}$, which we use to change the density in the trap. The resulting different transverse trap depths in the connection guide lead to small changes to the velocity distribution of the trapped ensembles. This, in combination with collision effects, results in the different single-body loss rates for the two connection guide voltages, visible in Figure 3.6. Both measurements, shown in Figure 3.6 are recorded for a trap offset of $V_{\text{off}} = 0.05V_{\mu}$. The solid and dashed lines depict single exponential fits to the first seven and to the last eight data points, respectively and their clearly distinct slopes show that modelling single-body trap losses with a single-exponential decay is insufficient for our electric trap.

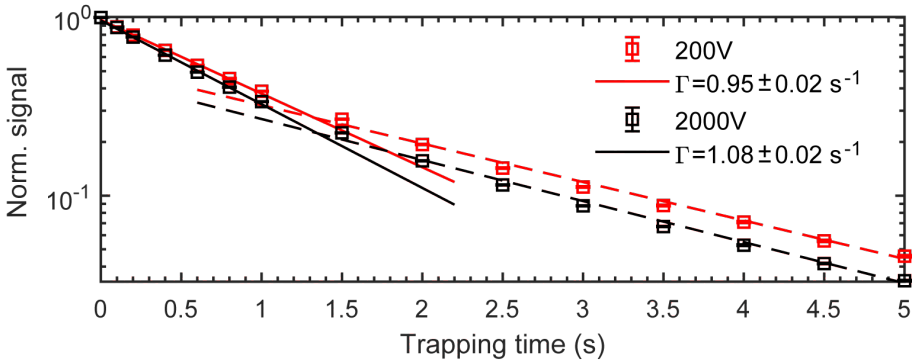

Figure 3.6: *Normalised trap unloading signal as a function of trapping time for the connection guide voltages* $V_{conn} = 200\,V$ *and* $V_{conn} = 2000\,V$ *and a trap offset field of* $E_{off} = 0.50kV/cm$. *The solid lines depict a single exponential fit to the data up to a trapping time of* $1s$, *whereas the dashed lines illustrate a single exponential fit to the data in range of* $[1.5s, 5s]$ *with decay rates of* $\Gamma_{200V} = 0.50 \pm 0.02s^{-1}$ *and* $\Gamma_{2000V} = 0.53 \pm 0.02s^{-1}$, *respectively.*

3.1.4 Detection

In addition to ensuring the three dimensional confinement of molecules in our trap the ring electrode also connects the loading and unloading guides to the trap [172]. The unloading or time-of-flight (TOF) guide, depicted in Figure 3.1 is a straight piece of guide that can be toggled on and off to record longitudinal velocity distributions $D(v_z)$ of the trapped ensemble. The molecules are detected by a Pfeiffer QMG 700 quadrupole mass spectrometer. After ionising the molecules by electron impact in

a crossed beam geometry the ions are mass filtered and counted using a secondary electron multiplier.

The count rate s measured by the QMS is related to density of molecules in the detection region n by a proportionality constant $s = c \cdot n$, which we determine by calibrating the QMS [114]. Therefore we record the count rate of the QMS as a function of CH_3F pressure in the vacuum chamber, illustrated in Figure 3.7 (a). There is one subtlety when measuring the CH_3F pressure with our hot cathode gauge. It is most sensitive to nitrogen and we have to account for the different sensitivity for CH_3F by a manufacturer given conversion factor. The offset in pressure in Figure 3.7 (a) is due to residual background gas in the vacuum chamber, which does not affect the density calibration. The black line depicts a linear fit to the data, where the slope provides the proportionality factor c between the count rate and the density in the detection region. We don't illuminate the QMS with a uniform density of molecules and so we have to take into account the beam spread of the molecules exiting the TOF-guide in vertical and horizontal direction by a geometrical correction factor c_{geo} [114]. Figure 3.7 (b) exemplary illustrates the vertical beam spread in blue together with a Gaussian fit in red as a guide to the eye. In the last step we also need to consider the time molecules spend in the detection area and thus the molecules' longitudinal velocity v_z which we determine by time-of-flight measurements as presented in section 3.2.2. Putting everything together we are able to convert the count rate detected be the QMS to the density of molecules in the trap as $f = \frac{c_{\text{geo}} \cdot v_z}{c \cdot V}$, where V is the trap volume. However there are several uncertainties associated with this calibration process. Both the hot cathode gauge as well as the QMS use electron impact ionisation to record the partial or total pressure in a given ionisation volume. This can cause distortion effects by over-estimating the total pressure due to fragmentation of CH_3F molecules [174]. During the calibration process there is a continuous flow of CH_3F into the vacuum chamber regulated by a needle valve. This counteracts our vacuum pumps and we do not have pressure equilibrium in the vacuum chamber. Thus the pressure recorded with the hot cathode gauge can be slightly different than the actual pressure in the detection region of the QMS due to the $\sim$ 10cm distance between pump and QMS. As we will see in section 3.2.6, this leads to a systematic overestimation of the conversion factor f by about a factor of two. We consistently correct the conversion factor for all following experiments shown in this thesis to obtain a consistent picture.

For high electron densities in the detection region of the QMS the molecular ions, created by electron bombardment, can be temporarily trapped. This is known as space charge effect [175, 176] which we attribute to dielectrics in the QMS charging up in the presence of a large electron current. A similar effect can appear if the density of ions in the detection region is large which can lead to an overestimation of slow molecules when measuring velocity distributions [177]. In addition we found that when there is a large space charge effect e.g. when the number of molecules in the detection region of the QMS is a large, the sensitivity to the molecules detected next is enhanced. It is crucial for us to avoid this. The collision signals we are going

to measure tend to be rather small and therefore we need to avoid systematic effects that potentially alter them. To remove the space charge effect in our measurements the TOF-guide is always in dipole configuration except during the unloading stage, see Figure 3.8 (d). Besides reducing the number of molecules in the detection region by switching the TOF-guide to dipole configuration the space charge effect can also be suppressed by reducing the electron density in the ion source of the QMS [114], which is given by

$$n_e = \frac{I_{em}}{A v_e}. \tag{3.1}$$

Here, where I_{em} is the electron emission current, A the cross-sectional area of the electron beam and v_e the electrons velocity. Since decreasing the emission current does not only reduce the magnitude of the space charge effect but also the detection efficiency, we keep the emission current fixed at $I_{em} = 0.8$mA. Instead we increase the cathode voltage V_{em} of the QMS to increase the electron velocity, $v_e \propto \sqrt{V_{em}}$, and thereby reduce the space charge effect without altering the detection efficiency [114]. By increasing the cathode voltage to $V_{em} = 75$V and keeping the TOF guide in dipole configuration while molecules are loaded into the trap we are able to get rid of the space charge effect within our measurement precision.

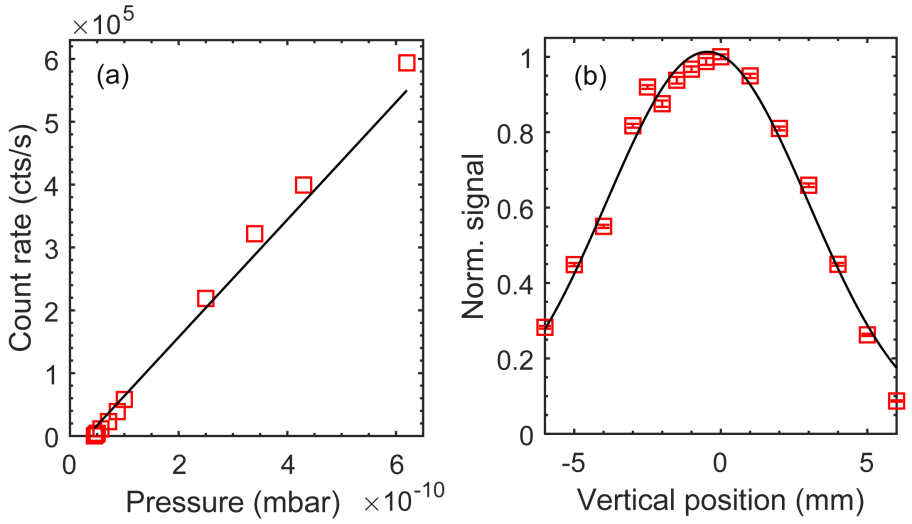

Figure 3.7: *(a) CH_3F density calibration of the QMS, showing the detected count rate as a function of the pressure in the QMS chamber. The black line is a linear fit to the data. (b) Normalised molecule signal detected by the QMS plotted against the vertical QMS position with respect to the centre of the TOF-guide. The black line depicts a Gaussian fit as a guide the eye.*

Besides the cathode voltage V_{em} another important QMS setting is the ion reference voltage $V_{\text{ion,ref}}$. It is required for electron impact ionisation of the molecules in the detection region as well as for extraction of the resulting molecular ions. $V_{\text{ion,ref}}$ is applied to a cage around the ionisation volume of the QMS whereas the end cap

of the TOF-guide is grounded. This results in a voltage difference and consequently in an electric field that can lead to a potential barrier for low-field-seeking states (see Figure 3.3) which can cause a deflection of slow molecules from the ionisation volume [174]. Prehn found strong experimental evidence for the hypothesis that we cannot detect molecules with longitudinal velocities below 3.9m/s with our QMS settings [174]. However a reduction of $V_{\mathrm{ion,ref}}$ is not practical since it comes along with a drastic decrease in detection efficiency.

3.2 Cold collision studies with the cryofuge

We start this chapter with a brief summary of the collision measurements that have been performed with the cryofuge before adding the electrostatic trap to the experiment [78, 114, 177]. The cryofuge is the ideal source to study molecule-molecule collisions. It produces such high density fluxes of slow and cold molecules that in 2017 [78] we were able to measure dipolar collisions directly in a quadrupole guide, without storing molecules in a trap. This was the first observation of collisions occurring between slow and cold polyatomic molecules.

After decelerating the molecules with the centrifuge we observed a density and velocity dependent collisional loss from the quadrupole guide, connecting the exit of the centrifuge with the QMS. The densities produced by the Cryofuge were so large that even with an interaction time as short as ~ 25ms we were able to measure collisional loss from the guide with a collision rate of 10Hz at an average collision energy of $E_{\mathrm{coll}} = 0.8\mathrm{K}\times k_B$ for CH_3F [78]. Both elastic and state changing inelastic collisions contribute to the loss. The respective two-body loss rate coefficients can be estimated using the Eikonal approximation [178] and the Langevin capture model [179] to calculate the theoretical loss rate $k_{th} = k_{el} + k_{in} = 7.7 \times 10^{-10}\mathrm{cm^3s^{-1}}$ for CH_3F [177]. This is in good agreement with the experimentally determined loss rate of $k = 1.1 \times 10^{-9}\mathrm{cm^3s^{-1}}$, considering the uncertainties in the density calibration (see section 3.1.4) as well as possible imprecisions in the calculation of the inelastic rate coefficient [114]. We want to emphasize here that the elastic cross-section itself is big with $\sigma_{el} = 2.5 \times 10^{-12}\mathrm{cm^2}$ but by utilising Monte Carlo trajectory simulations Wu et al. estimated that only 1 out of 17 elastic collisions lead to a loss from the guide [177].

After the successful demonstration of cold dipolar collisions between polyatomic molecules using the cryofuge the next step is to gain a more in depth understanding of the collision process as well as control over collisional effects. To realise this it is essential to load the molecules into a trap providing long interaction times [65] and a controlled environment [173] to perform collision studies. In 2017 we added a microstructure electrostatic trap, described in section 3.1.3, to the cryofuge experiment increasing the interaction time by at least a factor of 40.

3.2.1 Measurement scheme

The standard approach to measure collisions between trapped particles is to observe a density dependent two-body loss from the trap, [62, 71, 180], characterised by the rate constant k, in contrast to a background collision limited single exponential decay in trap signal. However our trap lifetime depends strongly on the velocity of the trapped particles, see section 3.1.3, causing deviations from a single exponential decay of the trapped signal. In combination with the fact that the measured collision loss rates are a factor of 5 to 10 lower than the single body loss rates (see section 3.2.5), makes it hard to disentangle these two effects.

To account for this we have to develop an alternative method that is robust against small changes to the single-body loss rate Γ and thereby enables us to extract a precise two-body loss rate k. The method we developed consists of three measurement schemes labelled A, B and A+B, schematically depicted in Figure 3.8 (a)-(c), respectively. In sample A we load the trap for $t_{\mathrm{load,A}} = 2$s, the loading stops by switching the connection guide and the s-piece from a guiding quadrupole configuration with guiding voltage V_{load} to dipole configuration, as illustrated in Figure 3.8 (d). This ensures that molecules are not only no longer guided but actively ejected from the quadrupole guides such that no molecules reach the trap after the loading has stopped. The loading period $t_{\mathrm{load,A}}$ follows a 100ms long trapping time before the variable time Δts starts. We label this period Δt the "interaction time", which we vary between 0–1s. At the end of the interaction time molecules are unloaded from the trap for $t_{\mathrm{unload}} = 2$s by switching the TOF guide from dipole to quadrupole configuration, also shown in Figure 3.8 (d). For sample A and $\Delta t = 0$s this means that molecules are directly unloaded after the 100ms of trapping time subsequent to the loading, whereas for $\Delta t = 1$s, there is an additional storage time of 1s before the trap is unloaded. The unloading sequence itself is identical for all three samples. For sample B, shown in Figure 3.8 (b), the loading starts at the beginning of the interaction time and continues until the end of Δt. Molecules are unloaded from the trap directly after the loading period $t_{\mathrm{load,B}}$.

With the measurement schemes A and B we create two independent samples of trapped molecules, where losses from the trap can occur due to single-body loss processes as well as due to bimolecular collisions, A–A collisions in sample A, and B–B collisions in sample B. The final measurement sequence combines these two independent samples together to create a third measurement A+B, as shown in Figure 3.8 (c). Here we allow the A and B sample to interact by consecutively loading them into the trap, separated by 100ms of dipole configuration for the connection guide and the s-piece, as shown in Figure 3.8 (d). This ensures that the loading conditions are identical for the combined sample A+B and the individual samples A and B. Due to the interaction of A and B in the combined sample there are not only A–A and B–B collisions but also additional two-body losses caused by A–B collisions. This additional loss is the collision signal $\delta n(t)$ we want to measure.

It is given by

$$\delta n(t) = n_A(t) + n_B(t) - n_{A+B}(t), \tag{3.2}$$

where $n_A(t)$, $n_B(t)$ and $n_{A+B}(t)$ are the densities of the trapped samples as a function of the interaction period and proportional to the integrated unloading signal, which is given by

$$\int_0^\tau u(t)dt = \eta \cdot N = \eta \cdot n \cdot V \propto n. \tag{3.3}$$

Here τ is the trap unloading time and $u(t)$ the trap unloading signal detected by the QMS. The integrated unloading signal is equal to the product of the number of molecules unloaded from the trap N and η, a constant related to the detection efficiency of the QMS. Taking into account the trap volume V it is evident that the integrated trap unloading signal is proportional to the density of trapped molecules n.

We want to note that in contrast to Figure 3.8 (a)-(c), where the TOF guide is in guiding configuration during loading to illustrate the loading sequences, for all other measurements presented in this thesis the TOF guide is in dipole configuration while molecules are loaded into the trap. With this we ensure molecules, which do not contribute to the collision signal, do not reach the QMS. Thereby we exclude that the space charge effect, see section 3.1.4 for more details, has an impact on our collision measurements. This is crucial since collision signals tend to be rather small such that we have to be careful that systematic effects do not alter the observed collision signals.

3.2.2 Velocity distribution of trapped molecules

An important measure when studying collisions is the relative velocity v_{rel} and thereby the collision energy $E_{\text{coll}} = \frac{1}{2}\mu v_{\text{rel}}^2$ of the particles, where μ is their reduced mass. At ultracold temperatures or equivalently ultralow collision energies the collision process is governed by quantum effects whereas for cold collisions a semi-classical description is more accurate [178]. In the following we will determine the relative velocity distribution $D(v_{\text{rel}})$ of the molecules in our microstructured electric trap.

In our experiment there are two methods to obtain the velocity distribution of trapped molecules; radio frequency depletion [181, 174] and time-of-flight measurements [181]. To record time-of-flight measurements we use exactly the same measurement sequences as for our collision measurements (see section 3.2.1) but instead of an unloading time of $t_{\text{unload}} = 2\text{s}$ we unload the trap for $t_{\text{unload}} = 4\text{s}$, to include also the slowest molecules in the velocity distribution. During unloading we toggle the 51cm long TOF-guide, connecting the trap exit with the QMS (see Figure 3.1), on and off as illustrated in blue in Figure 3.9 (a), to extract the longitudinal velocity v_z from the rising signal [181]. To ensure that the slowest molecules can reach the QMS we keep the TOF-guide in guiding configuration for $t_{\text{on}} = 290\text{ms}$, followed

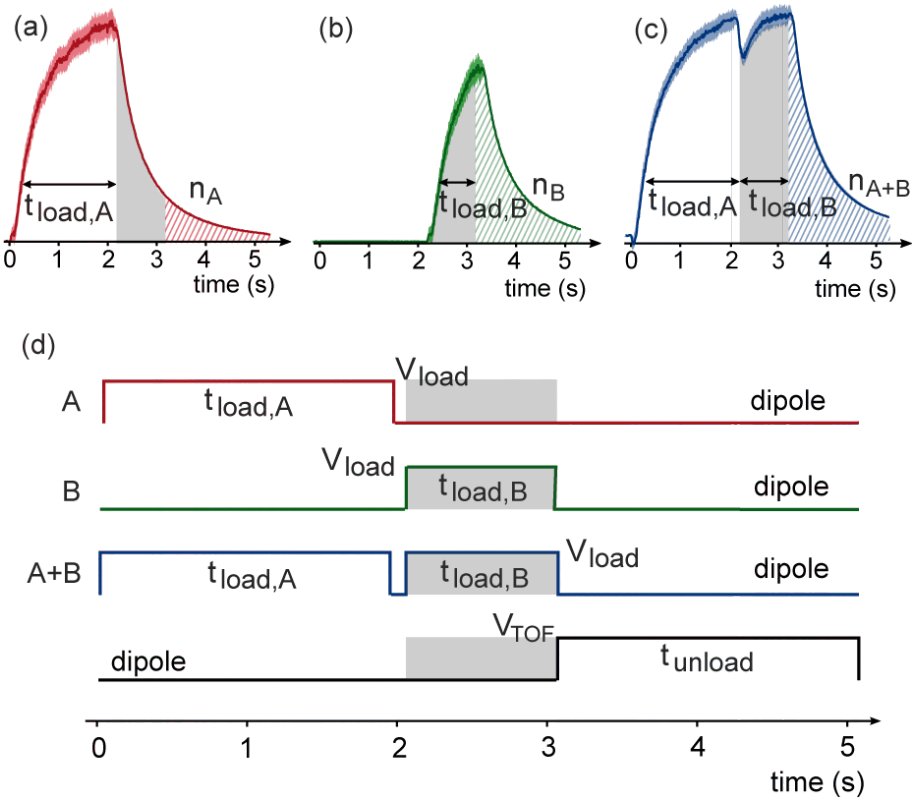

Figure 3.8: *(a)-(c) Measurements schemes for the A, B and A+B sample. The grey shaded area depicts the interaction time, here set to be $\Delta t = 1s$, and the dashed area illustrates the unloading of the molecules from the trap. The integrated unloading signal is proportional to the density of trapped molecules n. (d) Timing sequence for switching the loading and unloading guides between dipole and quadrupole configuration with guiding voltages V_{load} and V_{TOF} for the three different samples A, B and A+B. The interaction time is again set to be $\Delta t = 1s$ and illustrated by the grey shaded area. We want to note here that in (a)-(c) the TOF guide was on during loading for illustration purposes but for all other measurements presented in this thesis it is set to dipole configuration while loading the trap.*

by $t_{\text{off}} = 90$ms of dipole configuration, as depicted in Figure 3.9 (b). The overall duration for one on-off sequence is 400ms including switching times of $t_{\text{s}} = 10$ms between the different guiding configurations.

We repeat the on-off sequence ten times during the whole 4s of trap unloading in order to obtain a representative velocity distribution of the molecules in the trap [181]. This is necessary since fast molecules sample the trap exit at a faster rate (proportional to v^5 [172]) than slow molecules and therefore slow molecules would be underrepresented if we would only consider the beginning of the trap unloading. In addition we can add up the repetitions of the on sequences, illustrated in blue in the inset in Figure 3.9 (a), to improve statistics and to get the total distribution [181].

We observe an initial increase in signal from $t_{\text{unload}} = 0$ms onwards due to molecules arriving at the QMS. From the point in time where all velocity classes have reached the QMS the signal should become flat. However starting from $t_{\text{unload}} = 140$ms the signal starts to decrease instead of being constant. This can be explained by the fact that the on-off sequences are overlaid by the decay of the trap signal, visible in Figure 3.9 (a). To account for this effect we repeat the measurement sequence but we do not toggle the TOF-guide on and off during unloading instead we keep the time-of-flight guide in guiding configuration the whole unloading time t_{unload}, depicted in black in Figure 3.9 (a). We can now use this data set to fit an double-exponential decay to the trap unloading signal which we utilise to correct the decay in the on-off sequences. The result is illustrated in green in the inset of Figure 3.9 (a).

With this we can calculate the longitudinal velocity distribution $D(v_z)$ of the trapped ensemble as [181]

$$D(v_z) = -\frac{dS(t)}{dv_z} = \frac{L}{v_z^2}\frac{dS(t)}{dt}, \tag{3.4}$$

where S(t) is the signal recorded during the 290ms on period (summed and normalised), depicted in green in the inset of Figure 3.9 (a) and L is the length of the TOF-guide. The resulting velocity distribution with a mean velocity of $\bar{v}_z = 9.5$m/s is illustrated in Figure 3.9 (c) in a histogram and scatter plot after binning the data. The measurement shown here is performed for the A+B sample at a trap offset of $E_{\text{off}} = 0.05V_\mu$, a connection guide voltage of $V_{\text{conn}} = 2000$V and an interaction time of $\Delta t = 0.5$s.

In the following we will use the measured longitudinal velocity distribution $D(v_z)$ to calculate the molecules total velocity distribution in the trap $D(v_{\text{tot}})$, where $v_{\text{tot}} = \sqrt{v_x^2 + v_y^2 + v_z^2}$. Since our trap provides a uniform three dimensional confinement the maximum energy of a trappable molecule $E_{\text{tot,max}} = \frac{1}{2}mv_{\text{tot,max}}^2$ is given by a sphere in energy space. Hence we express the x-, y- and z-component of the total velocity in spherical coordinates

$$\begin{aligned} v_x &= v_{\text{tot}}\sin(\theta)\cos(\phi) \\ v_y &= v_{\text{tot}}\sin(\theta)\sin(\phi) \\ v_z &= v_{\text{tot}}\cos(\theta) \end{aligned} \tag{3.5}$$

with θ and ϕ being the standard expressions for the inclination and the azimuth. The maximum longitudinal velocity $v_{\text{z,max}}$ recorded with time-of-flight measurements allows us to calculate $E_{\text{tot,max}}$ where the molecule's velocity is solely given by v_z such that $v_{\text{tot,max}} = v_{\text{z,max}}$. With this we can compute an upper bound for the inclination θ using Equation 3.5 for each component in $D(v_z)$ as

$$\theta_{\text{max}} = \arctan\left(\sqrt{\frac{v_{\text{z,max}}^2 - v_z^2}{v_z^2}}\right). \tag{3.6}$$

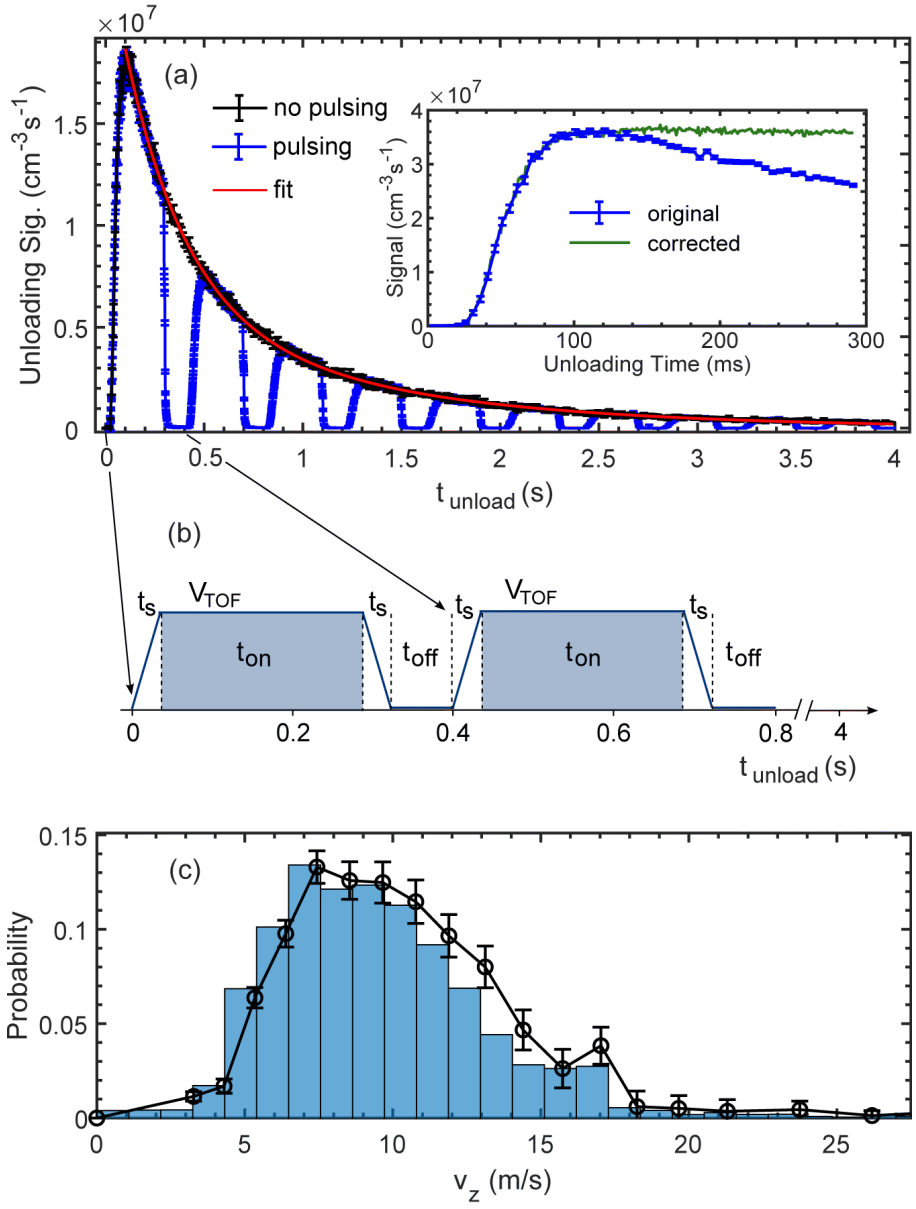

Figure 3.9: *(a) Trap unloading signal as a function of the unloading time with the TOF guide in guiding configuration in black and a double-exponential fit to the data in red. The blue data points show the trap unloading signal while the TOF guide is repeatedly toggled on and off and the sum of these sequences is depicted in the inset of (a). Here the raw data are shown in blue, while green depicts the signal corrected for the decay in the unloading curve. (b) On-off timing sequence of the TOF-guide during trap unloading for the first two blocks. (c) Velocity distribution obtained from the data depicted in green in the inset in (a) as a histogram and scatter plot.*

For a given longitudinal velocity v_z the total velocity v_{tot} can take any value between v_z and $v_{\mathrm{tot,max}} = v_{\mathrm{z,max}}$. To account for this we uniformly sample $\theta \in [0, \theta_{max}]$ to

calculate a distribution of possible v_{tot} values for each element in $D(v_z)$ according to $v_{\mathrm{tot}} = v_z/\cos(\theta)$. Calculating the mean value of the v_{tot}-distribution allows us to assign one value for the total velocity for a given v_z. By repeating this procedure for each element in $D(v_z)$ we obtain a distribution for the total velocity $D(v_{\mathrm{tot}})$ in the trap for $E_{\mathrm{off}} = 0\mathrm{kV/cm}$ and thereby also a distribution for the total energy of the molecules via $E_{\mathrm{tot}} = \frac{1}{2}m\boldsymbol{v}_{\mathrm{tot}}^2$. However since we need to apply an offset field in the centre of the trap to suppress losses due to Majorana transitions we need to account for the molecules' potential energy in the trap. It is given by the Stark interaction between the molecules' dipole moment d_{avg}, averaged over the state distribution in the trap, and the trap offset field E_{off} as $E_{\mathrm{pot}} = -d_{\mathrm{avg}} \cdot E_{\mathrm{off}}$. This allows us to calculate the kinetic energy of the trapped molecules in the presence of a non-zero offset field as $E_{\mathrm{kin}} = E_{\mathrm{tot}} - E_{\mathrm{pot}}$ which we use to obtain $D(v_{\mathrm{trap}})$. The result is illustrated in orange in Figure 3.10 (a) for the A sample with a trap offset field of $E_{\mathrm{off}} = 0.05V_{\mu}$ and an interaction time of $\Delta t = 1\mathrm{s}$.

Besides time-of-flight measurements we can also obtain the molecules' velocity distribution in the trap using radio-frequency depletion measurements [181, 174]. The starting point is our microstructured electric trap providing a box-like trapping potential with a homogeneous offset field E_{off} in the centre and a steeply rising trapping field at the edge of the trap E_{edge}, as described in section 3.1.3. The inset in Figure 3.10 (a) schematically illustrates the Stark energy of a molecule moving from the homogeneous field region in the centre of the trap (E_{off}) into the high field region at the edge of the trap trap (E_{edge}). According to the molecules' kinetic energy they climb up the potential hill, given by the Stark interaction, and thereby kinetic energy is transformed into potential energy. By coupling low-field-seeking with high-field-seeking states in the high field region of the trap using radio-frequency, as depicted in the inset of Figure 3.10 (a), we actively deplete molecules from our trap. We repeat this depletion process in separate measurements for different radio-frequency energies $E_{\mathrm{rf}} = h \cdot f$ to map out the energy distribution of the molecules. Similar to the time-of-flight measurements we need to subtract the potential energy of the molecules in the homogeneous offset field $E_{\mathrm{kin}} = E_{\mathrm{tot}} - E_{\mathrm{pot}}$ to calculate the velocity distribution $D(v_{\mathrm{trap}})$ of the trapped molecules from the remaining kinetic energy $E_{\mathrm{kin}} = \frac{1}{2}m\boldsymbol{v}_{\mathrm{trap}}^2$. The resulting velocity distribution $D(v_{\mathrm{trap}})$ is shown in blue in Figure 3.10 (a) for the A measurement at a trap offset field of $E_{\mathrm{off}} = 0.50\mathrm{kV/cm}$ and an interaction time of $\Delta t = 1\mathrm{s}$.

To ensure that we deplete all molecules for a given energy we have to saturate the corresponding transition, therefor we need to apply the radio-frequency radiation for several hundreds of ms [114]. For the data presented in Figure 3.10 (a) we apply the radio-frequency during the whole interaction period of $\Delta t = 1\mathrm{s}$ and thereby ensure that the transition is saturated.

Figure 3.10 (a) shows good agreement between the data recorded using radio-frequency depletion and time-of-flight measurements. However for low velocities we observe a deviation between the two measurement schemes, where we see less slow molecules in the time-of-flight measurement probably due to electric stray fields at

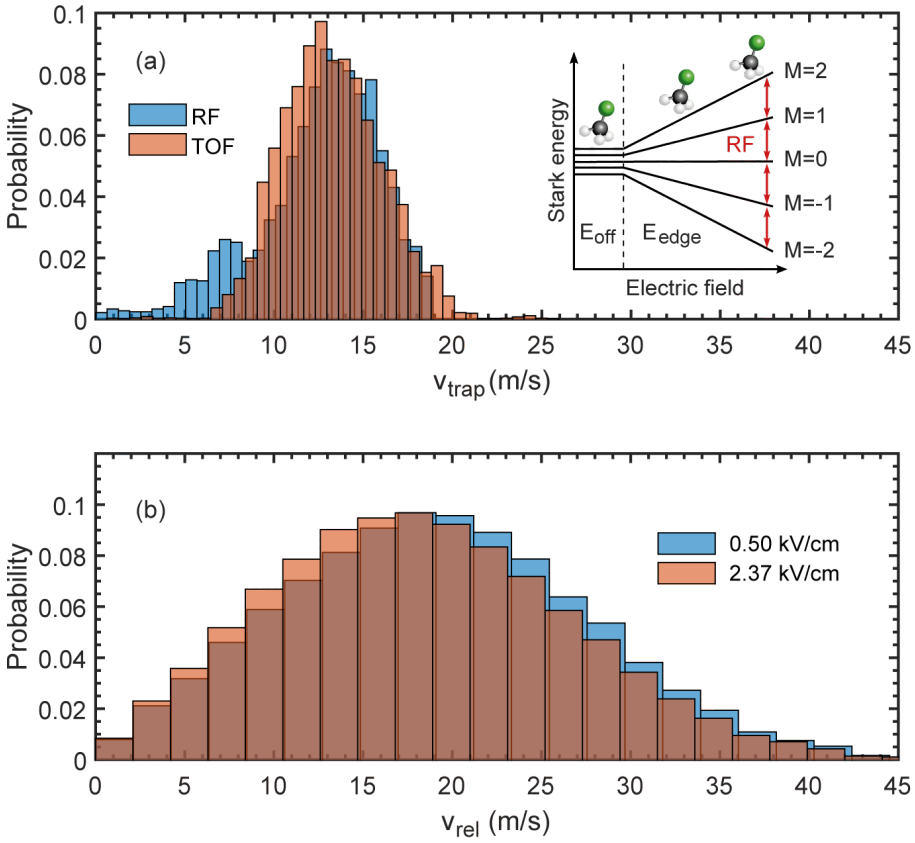

Figure 3.10: *(a) Velocity distribution of trapped molecules for the A sample recorded using time-of-flight measurements (orange) and radio frequency depletion (blue) for a trap offset of* $V_{off} = 0.05V_\mu$ *and an interaction time of* $\Delta t = 1s$*. The inset depicts a schematic illustration of the radio frequency depletion measurements. (b) Relative velocity distribution in the trap for the A+B sample for the two trap offsets* $V_{off} = 0.05V_\mu$ *(blue) and* $V_{off} = 0.30V_\mu$ *(orange).*

the QMS, repelling the slowest molecules (see section 3.1.4 for more details). In the framework of this thesis we use time-of-flight measurements to obtain velocity distributions in the trap. In comparison to radio-frequency depletion measurements this technique makes it is easier to interpret $D(v_{\mathrm{trap}})$ for different measurement schemes and interaction times Δt, since we can unload the molecules directly after the respective measurement sequence without applying radio-frequency for several hundreds of ms where the velocity distribution can change.

Using $D(v_{\mathrm{trap}})$ obtained from the time-of-flight measurements, we can now calculate the relative velocity distribution $D(v_{\mathrm{rel}})$, for colliding molecules in the trap, exemplary depicted in Figure 3.10 (b) for the A+B sample and an interaction time of $\Delta t = 0.5$s. Blue and orange show $D(v_{\mathrm{rel}})$ for the trap offsets $V_{\mathrm{off}} = 0.05V_\mu$ and $V_{\mathrm{off}} = 0.30V_\mu$, respectively. According to $E_{\mathrm{pot}} = -d_{\mathrm{avg}} \cdot E_{\mathrm{off}}$, the potential energy of a molecule in the homogeneous field region is larger for a higher trap offset field.

Thus the mean relative velocity of the trapped ensemble is lower for the trap offset field $E_{\text{off}} = 2.37\text{kV/cm}$ with $\bar{v}_{\text{rel}} = 18.4\text{m/s}$ than for $E_{\text{off}} = 0.50\text{kV/cm}$ with $\bar{v}_{\text{rel}} = 19.3\text{m/s}$.

3.2.3 State distribution in the trap

Molecule-molecule collisions, in particular inelastic state changing collisions, can show a state dependence in their dynamics [182], where e.g. the probability for a transition from low-field-seeking to high-field seeking state can be distinct for different $|J, K, M\rangle$ states [183]. Since we are going to measure collisional loss from our trap it is therefore important to determine the state distribution in our microstructured electric trap. We will cover this topic only very briefly here, since detailed descriptions can be found in several doctoral theses in our group [173, 181, 174].

For our experiment the state distribution in the trap is determined by two components, the cooling of the molecules internal degrees of freedom in the buffergas cell [93] and the electric guidability of the molecules [181] exiting the cell. The guideability is determined by the molecules electric field response, it's mass and dipole moment [133]. Only molecules in a low-field seeking state can be guided, where a light molecule with a linear Stark shift together with a large dipole moment ensures the best confinement. However not all of these properties need to be full filled to electrostatically guide a molecule but the less of them are satisfied the higher the probability for the molecule to be lost between the buffergas cell and the trap. Our molecule of choice is the symmetric top molecule CH_3F, thus mass and dipole moment are fixed for the measurements presented in this thesis. The electric field response however can vary depending on the rotational state of the molecule. As described in section 2.2.1, there is an energetically degenerate pair of opposite parity state for each rotational state in CH_3F with $|K| > 0$, resulting in a linear Stark shift, where the slope is given by $\frac{KM}{J(J+1)}$. Besides the linear electric field response, for $K = 0$ there is no energetically degenerate pair of opposite parity states that can be mixed by the electric field, so that the corresponding Stark shifts show a quadratic behavior. Consequently these molecules are worse guided than molecules in a stretched state with a linear field response.

The sympathetic cooling of the molecules' internal degrees of freedom with cold helium atoms in the buffergas cell depends on the cell temperature and the energy of the molecules' rotational levels [93]. We operate our buffergas cell in the boosted regime, where the population of the rotational states can be approximated by a Boltzmann distribution assuming that the molecules are thermalised to the cell temperature [93]. The likelihood for a state to be populated is proportional to the Boltzmann factor $e^{-E_{\text{rot}}/k_B T}$, with E_{rot} being the rotational energy of the molecule and T the cell temperature [136]. A large rotational energy and a cold cell result in a high state purity with only few rotational states being populated. We determine the state distribution in the trap by utilising microwave radiation which we use to couple different rotational states [173]. We actively deplete molecules from the

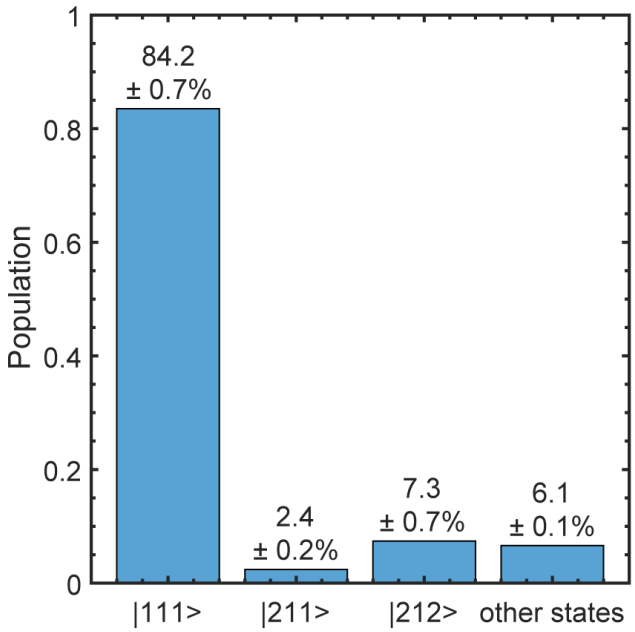

Figure 3.11: *Measured rotational state distribution $|JKM\rangle$ of CH_3F in our microstructured electric trap for a buffergas cell operated in the boosted regime at a cell temperature of 4K.*

trap by coupling populated low-field seeking with high-field seeking states, where the amount of depletion provides insights into the population in the respective $|J, K, M\rangle$ state [173]. We will not present more details on the measurement scheme or on how to extract the state distribution from the measured depletion curves here, since very detailed descriptions of these processes can be found in various doctoral theses in our group [173, 181, 174].

Instead we present the results of the microwave depletion measurements, where Figure 3.11 shows the measured state distribution in the trap for a buffergas cell temperature of 4K, operated in the boosted regime. The most significantly populated states in our trap are the $|J = 1, K = 1, M = 1\rangle$ state with $84.2 \pm 0.7\%$, the $|J = 2, K = 1, M = 2\rangle$ state with $7.3 \pm 0.7\%$ and the $|J = 2, K = 1, M = 1\rangle$ state with $2.4 \pm 0.2\%$. This adds up to a total population of 93.3%, where the missing $6.1 \pm 0.1\%$ are distributed over higher lying rotational levels, with no single $|J, K, M\rangle$ state being populated by more than 1%.

Figure 3.11 also reveals the impact of rotational state cooling in the buffergas cell with the population in the (1,1)-manifold being roughly eight times larger than the population in the (2,1)-manifold. This is due to the fact that the rotational energy of the $|J = 2, K = 1\rangle$ states is about 102GHz·h larger than for the $|J = 1, K = 1\rangle$ states, such that according to the Boltzmann factor the likelihood to populate the (2,1)-manifold at a cell temperature of 4K is significantly reduced. In addition we can also see the effect of guideabilty by comparing the

population in the $|J = 2, K = 1, M = 1\rangle$ and $|J = 2, K = 1, M = 2\rangle$ states. For these states the Boltzmann factor is identical, since the rotational energy, given by $E_{\text{rot}} = BJ(J+1) + (A-B)K^2$ with A and B being the rotational constants of a prolate symmetric top molecule, does not depend on the M-quantum number. Thus the difference in population is solely given by the guideability, where the state with a stronger Stark shift, $|J = 2, K = 1, M = 2\rangle$, and thus better confinement is more populated.

3.2.4 Observation of collisions between trapped molecules

Figure 3.12 (a) depicts the molecule signal detected by the QMS as a function of time, where $t = 0$ indicates the start of the interaction period Δt. Since the TOF guide is in dipole configuration during the interaction time no molecules arrive at the QMS. When the unloading guide is switched on we observe an initial increase in signal due to molecules arriving at the QMS followed by a decay in signal as a function of the trap unloading time t_{unload}. As expected, for an interaction time $\Delta t > 0$s, the A+B sample is largest in signal. The A sample on the other hand has already significantly decayed during the trapping time $\Delta t = 1$s and is thereby the smallest of the three trapped ensembles.

By integrating the unloading signal for interaction times in range of $\Delta t \in [0, 1]$s, we can investigate the density of trapped molecules as a function of Δt for the different measurement schemes. To ensure a representative flux of molecules for all relevant velocity classes that can be detected via the QMS ($v_z > 3.9$m/s) we wait 150ms after switching the TOF guide to quadrupole configuration before we start to integrate the trap unloading signal. The result is illustrated in Figure 3.12 (b) showing the integrated trap unloading signals for the A,B and A+B measurements as a function of the interaction period. Since no molecules are loaded into the trap for the A sample during the interaction time (see section 3.2.1) the density of trapped molecules decays as a function of Δt due to single-body loss processes as well as due to collisional loss. In sample B however molecules are loaded into the trap during the whole interaction period Δt such that the density of trapped molecules increases as a function of Δt. Since the connection guide and the s-piece are in dipole configuration before the loading is turned on the trapped signal only starts to significantly rise from $\Delta t = 0.1$s onwards due to the molecules time-of-flight time from the connection guide to the trap. Thus the trapped signal in the A and in the A+B sample overlap within the errorbars up to $\Delta t = 0.1$s in Figure 3.12 (a).

Using the measured integrated densities we can calculate the additional loss $\delta n(t)$, according to Equation 3.2. In general bimolecular collisions are characterised by a quadratic dependence of the collision signal on the density of the interacting particles [62]. Thus to confirm that the additional loss we measure is caused by bimolecular collisions, $\delta n(t)$ has to depend quadratically on the density of trapped molecules. We tune the density of the trapped samples by changing the connection

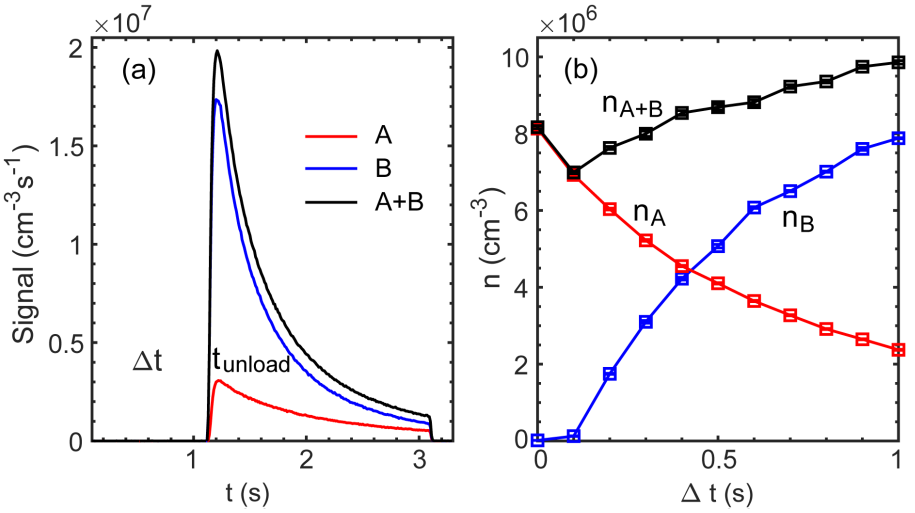

Figure 3.12: *(a) Trap unloading signal as a function of time for the A, B and A+B sample. The interaction time in this plot is $\Delta t = 1s$ and we unload the trap for $t_{unload} = 2s$. (b) Integrated trap unloading signals as a function of the interaction time Δt. In both plots the connection guide voltage is set to be $V_{conn} = 2000\,V$ and trap offset is $V_{off} = 0.05V_{\mu}$.*

guide voltage in range of $V_{\mathrm{conn}} = 200\mathrm{V}$ to $V_{\mathrm{conn}} = 2000\mathrm{V}$ and thereby its maximum transverse trapping field from $E_{\mathrm{conn}} = 2\mathrm{kV/cm}$ to $E_{\mathrm{conn}} = 20\mathrm{kV/cm}$. In total we use four different settings for V_{conn} to record the additional loss after an interaction time of $\Delta t = 1\mathrm{s}$. The result is plotted in Figure 3.13 as a function of the product of the integrated densities for the A and B sample, which we obtain as

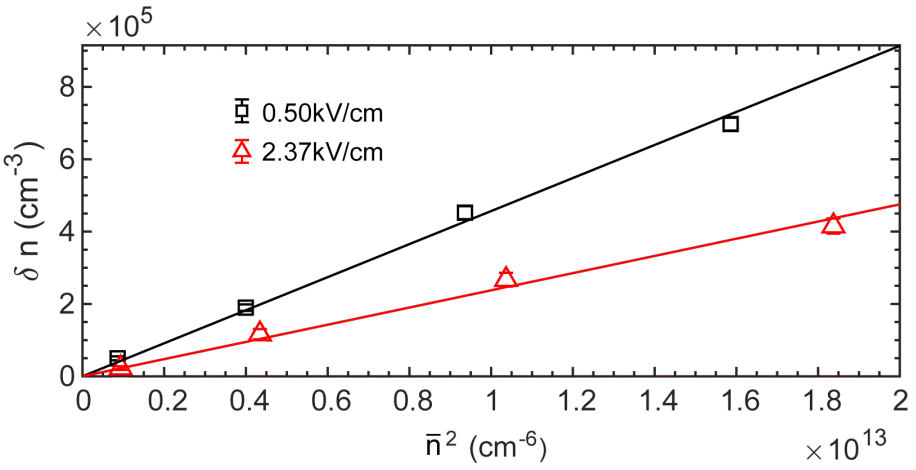

Figure 3.13: *Additional loss δn due to the interaction of sample A and sample B for $\Delta t = 1s$ as a function of the product of the integrated densities of the two samples. The solid lines depict a linear fit to the data. The trap offset was set to be $V_{off} = 0.05V_{\mu}$ (black) and $V_{off} = 0.30V_{\mu}$ (red).*

$$\bar{n}^2 = \int_0^1 n_A(t) \cdot n_B(t) dt. \tag{3.7}$$

The expected linear behavior, as a function of $\bar{n}^2$, proves the observation of molecule-molecule collision induced loss from our electric trap.

The ability to tune the homogeneous trap offset field E_{off} (see section 3.1.3) allows us to record the collisional loss as a function of the applied electric field. Figure 3.13 shows two clearly distinct slopes, proportional to the respective two-body loss rates k, for the two trap offset fields $E_{\text{off}} = 0.50\text{kV/cm}$ and $E_{\text{off}} = 2.37\text{kV/cm}$. This is a clear indication for an electric field dependence of the measured collision process. However to investigate this in more detail we need a profound method to extract a precise value for the two-body loss rate k from our collision measurements.

3.2.5 Extraction of the two-body loss rate k

To gain a more qualitative understanding of our measurements we set up a model describing the dynamics of the trapped samples including molecule-molecule collision induced two-body loss, characterised by the two-body loss rate k. We use this model to fit the measured collision signal and thereby extract a robust value for k. We start by looking at the time evolution of the densities of the trapped ensembles

$$\dot{n}_x = \lambda_x - \Gamma_x n_x - k n_x^2 \tag{3.8}$$

where x can be the measurement sequence A, B, or A+B. The loading rate of the molecules into the trap is given by λ and k is the two-body collisional loss rate. Single-body loss processes, including trap losses due to holes in the potential, Majorana transitions and collisions with background gas, are governed by the rate coefficient Γ. Due to the interaction of A and B molecules in the A+B sample, we observe additional collisional loss δn (see Equation 3.2) that not only alters the density of the A+B sample but also has an impact on the rate coefficient Γ_{A+B}. Assuming sample A and sample B do not interact, which is equivalent to $k = 0$, Γ_{A+B} is given by the weighted sum of the single-body loss rates of the A and B sample as

$$\Gamma_{A+B} = \frac{\Gamma_A n_A + \Gamma_B n_B}{n_{A+B}}. \tag{3.9}$$

However, since $k \neq 0$ the A and the B sample do interact and thereby cause collision induced loss from the electrostatic trap, such that these molecules and the associated single-body loss rate do not contribute to Γ_{A+B}. We need to account for this in the expression for the single-body loss rate parameter, according to Equation 3.2, such that we arrive at

$$\Gamma_{A+B} \approx \frac{\Gamma_A n_A + \Gamma_B n_B - \Gamma_n \delta n}{n_{A+B}}, \tag{3.10}$$

where Γ_n is the single-body loss rate of the collision signal or equivalently the single-body loss rate of the molecules lost from the trap. This seems counter-intuitive but

this term is required to ensure that $\delta n = 0$ for $k = 0$, as we will see later. We want to note that in the expression for Γ_{A+B} we neglect that elastic collisions can in principle alter the velocity distribution of the trapped ensemble and thus the single-body loss rate. However, as we show in section 3.2.6, the impact of elastic collisions is very small such that Equation 3.10 is a good approximation for Γ_{A+B}.

With this we have everything in place to derive an expression for the time evolution of the additional loss δn. Therefore we take the time derivative of Equation 3.2, given by

$$\dot{\delta}n = \dot{n}_A + \dot{n}_B - \dot{n}_{A+B} \tag{3.11}$$

and insert the time evolution of the trapped ensembles, A, B and A+B, given by Equation 3.8 to arrive at

$$\dot{\delta}n = \lambda_A + \lambda_B - \lambda_{A+B} - \Gamma_A n_A - \Gamma_B n_B + \Gamma_{A+B} n_{A+B} - k(n_A^2 + n_B^2 - n_{A+B}^2). \tag{3.12}$$

We simplify this equation by making use of the fact that $\lambda_{A+B} = \lambda_A + \lambda_B$ and utilise the expressions for Γ_{A+B} and δn, given by Equation 3.10 and 3.2, respectively, to obtain

$$\dot{\delta}n = -\Gamma_n \delta n - k(n_A^2 + n_B^2 - (n_A + n_B - \delta n)^2), \tag{3.13}$$

which we simplify and thereby finally arrive at

$$\dot{\delta}n = 2k n_A n_B - \delta n[\Gamma_n + 2k(n_A + n_B)] + k(\delta n)^2. \tag{3.14}$$

This differential equation consists of four different contributions. The single-body loss rate of the collision signal Γ_n, the densities of trapped molecules n_A and n_B, being functions of the interaction time Δt, and the two-body loss rate k. The largest contribution to Equation 3.14 is given by the first term, the product term of the densities of the A and the B sample. The quadratic part of Equation 3.14 however is just a small correction term. Thus we first neglect it to solve the resulting linear differential equation analytically. Afterwards we include the quadratic term pertubatively in a regular pertubation series to first order [184].

We use the ansatz $\delta n = \delta n_0 + \epsilon \delta n_1$, which we insert into the differential Equation 3.14 and order the terms according to the power of ϵ resulting in two differential equations, one for δn_0 and one for δn_1. The differential equation of δn_0 is just the linear part of Equation 3.14 and thus given by

$$\dot{\delta}n_0 = 2k n_A n_B - \delta n_0[\Gamma_n + 2k(n_A + n_B)]. \tag{3.15}$$

This is a first order linear ordinary differential equation with variable coefficients that can be solved analytically as [185]

$$\delta n_0(t) = e^{-q(t)} \int_0^t dt' e^{q(t')} 2k n_A(t') n_B(t') \tag{3.16}$$

with

$$q(t) = \int_0^t dt' [\Gamma_n + 2k\,(n_A(t') + n_B(t'))]\,. \tag{3.17}$$

In a second step we consider the contribution of the quadratic term via the differential equation for δn_1, given as

$$\dot{\delta} n_1 = k(\delta n_0)^2 - \delta n_1[\Gamma_n + 2k(n_A + n_B)]. \tag{3.18}$$

Again, we can also solve this differential equation analytically to obtain [185]

$$\delta n_1(t) = e^{-q(t)} \int_0^t dt' e^{q(t')} k(\delta n_0(t'))^2. \tag{3.19}$$

By combining the contribution of the dominating linear part and the quadratic correction, $\delta n(t) = \delta n_0(t) + \delta n_1(t)$ we obtain the solution of the differential Equation 3.14. This provides us an analytic expression for the time evolution of the additional loss δn, which we can use to fit the measured collision signal.

Since we can measure the density of trapped molecules n_A and n_B, as a function of the interaction time, exemplary depicted in Figure 3.12 (b) for $V_{\text{conn}} = 2000\text{V}$ and $E_{\text{off}} = 0.50\text{kV/cm}$, as well as Γ_n, we can reduce the number of fit parameters such that k is the only free parameter. In order to obtain the single-body loss rate Γ_n from our measurements, we extract the trap unloading curve of the collision signal, utilising Equation 3.2 and the time dependent trap unloading curves, exemplary shown in Figure 3.12 (a) for $V_{\text{conn}} = 2000\text{V}$ and $E_{\text{off}} = 0.50\text{kV/cm}$. The result is illustrated in Figure 3.14 (a) showing the trap unloading signal of the additional loss due to A–B collisions, as a function of the trap unloading time for $V_{\text{conn}} = 2000\text{V}$ and $V_{\text{conn}} = 200\text{V}$. As expected, we observe a significant difference in the collision signal between the low density ($V_{\text{conn}} = 200\text{V}$) and the high density sample ($V_{\text{conn}} = 2000\text{V}$). We fit a single exponential decay to the $V_{\text{conn}} = 2000\text{V}$ data excluding the first 150ms, to ensure a representative flux of molecules for all relevant velocity classes that can be detected, and thereby obtain $\Gamma_n = 0.83 \pm 0.02\text{s}^{-1}$.

To calculate the integrated collision signal for a given interaction time, we again utilise Equation 3.2, but now we use the integrated trap unloading signals, exemplary illustrated in Figure 3.12 (b). The result is depicted in black in Figure 3.14 (b) showing the density of lost molecules due to A–B collisions as a function of Δt for a connection guide voltage of $V_{\text{conn}} = 2000\text{V}$ and a trap offset field of $E_{\text{off}} = 2.37\text{kV/cm}$. The blue data points depict the solution of Equation 3.14 fitted to the collision data at $\Delta t = 1\text{s}$, thereby yielding the two-body loss rate $k = (1.71 \pm 0.10) \times 10^{-8}\text{cm}^3\text{s}^{-1}$. If we exclude the quadratic term and only consider the linear contribution in Equation 3.14 we obtain $k = (1.72 \pm 0.10) \times 10^{-8}\text{cm}^3\text{s}^{-1}$, proving that the quadratic term provides only a very small correction to k.

We want to note that it can take up to five days of measurements to get good statistics for the measured loss for a single interaction time Δt. Thus the collision data shown in black in Figure 3.14 (b) is the only data set where we recorded the additional loss due to A–B collisions for interaction times in range of $\Delta t \in [0, 1]\text{s}$. For all the other collision measurements presented in this thesis we record the additional loss only for $\Delta t = 1\text{s}$. As a consequence we can only fit the model to the experimental

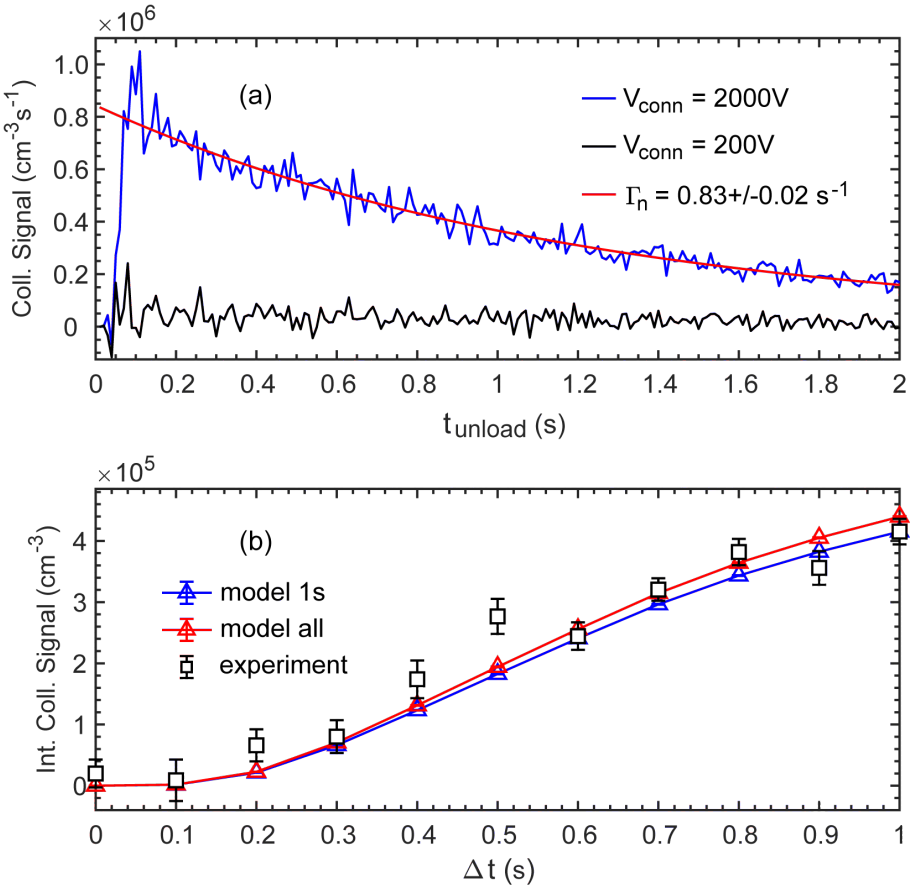

Figure 3.14: *(a) Trap unloading signal of the additional loss plotted against the trap unloading time for connection guide voltages $V_{conn} = 2000\,V$ and $V_{conn} = 200\,V$. The interaction period is $\Delta t = 1s$ and the trap offset field is set to $E_{off} = 0.50 kV/cm$. The red line depicts a single exponential fit to the $V_{conn} = 2000\,V$ data, excluding the first $150ms$. (b) Measured collisional loss in black as a function of Δt and the respective models fitted to all data points (red) and the collisions signal at $\Delta t = 1s$ only (blue). The connection guide voltage was again set to $V_{conn} = 2000\,V$ but the trap offset field is $E_{off} = 2.37 kV/cm$.*

data at $\Delta t = 1$s, which is possible since k is the only free fit parameter in our model. However to test if this is a valid approach we fit the solution of Equation 3.14 once to the collisions signals for all interaction times depicted in Figure 3.14 (b) (red) and once to the measured collision signal at $\Delta t = 1$s (blue) only to extract the respective rate coefficients as $k = (1.83 \pm 0.15) \times 10^{-8} \mathrm{cm}^3 \mathrm{s}^{-1}$ and $k = (1.71 \pm 0.10) \times 10^{-8} \mathrm{cm}^3 \mathrm{s}^{-1}$, respectively. The two-body loss rates agree within the errorbars showing that it is a valid approach to only consider the collision data at $\Delta t = 1$s. We want to emphasize that, according to Equation 3.16 and 3.19, we still have to measure the densities n_A and n_B for interaction times in range of $\Delta t \in [0, 1]$s to perform the numeric integrals, such that we can fit the model to the measured collision signal.

The purpose of our measurement scheme, introduced in section 3.2.1, is to extract a precise value for the two-body loss rate k, insensitive to small changes in the single-body loss rate coefficient Γ. This is important for our experiment since our trap lifetime shows a velocity dependence, causing deviations from a single exponential decay (see section 3.1.3), that is difficult to disentangle from collisional two-body loss. In the following we will compare the dependence of k on Γ for the measurement scheme developed in this thesis with the standard two-body loss model, used to model collisional loss [62]. The two-body loss model is given by Equation 3.8 with $\lambda = 0$ for the A sample which we can solve as [185]

$$n_A(t) = -\frac{n_{A,0} \cdot \Gamma_A}{k \cdot n_{A,0} - (\Gamma_A + k \cdot n_{A,0}) \cdot e^{\Gamma_A \cdot t}} \tag{3.20}$$

with $n_{A,0}$ being the density in the trap at $t = 0$ for the A sample. We can now fit

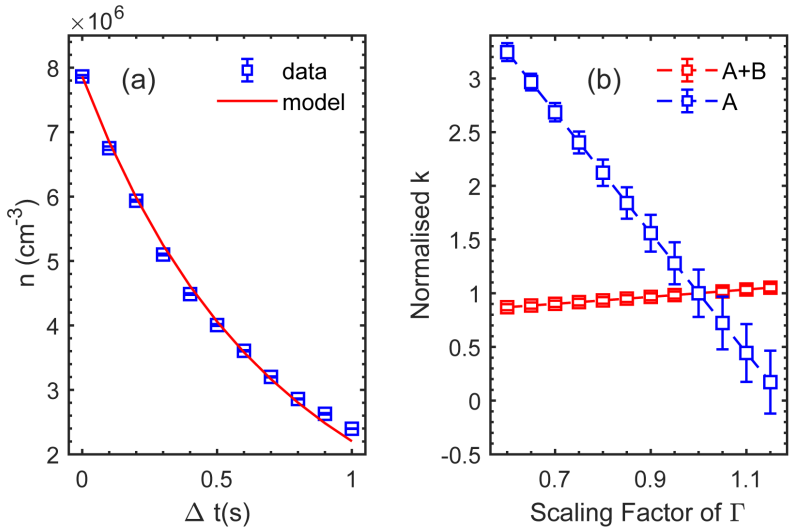

Figure 3.15: *(a) Integrated densities of the A sample as a function of the interaction time in blue together with fit of Equation 3.20 to the data in red. (b) Dependence of the two-body loss rate k on the rate coefficient Γ when fitting Equation 3.20 to the integrated densities of the A sample (blue) and the solution of Equation 3.14 to the integrated collision signal (red).*

Equation 3.20, to the measured integrated densities for the A sample as a function of the interaction time Δt, as illustrated in Figure 3.15 (a), to obtain the two-body loss rate k for a given rate coefficient Γ. We repeat this fitting process for multiple values of Γ which we obtain by multiplying a scaling factor $s \in [0.6, 1.15]$ to the measured single-body loss rate to test how sensitive the fitted rate coefficient k is on Γ. The result is shown in Figure 3.15 (b) in blue, where we normalised the extracted two-body loss rates to the value for k which we obtain for the measured value of Γ ($s = 1$). In addition Figure 3.15 (b) also shows the dependence of k on Γ for the measurement scheme developed in this thesis in red. Here we fit

the collision model (solution of Equation 3.14) to the measured integrated collision signal (see Figure 3.13) but instead of scaling Γ_A we multiply Γ_n with the scaling factor $s \in [0.6, 1.15]$. We can clearly see, that in contrast to the two-body loss model (blue), our measurement scheme to record collisional loss (red), is insensitive to small changes in the single-body loss rate parameter.

The extraction of k allows us to determine the collisional loss rate, given by $\Gamma_{\text{coll}} = \bar{n} \cdot k$, the product between the integrated density of the trapped ensemble (see Equation 3.7) and the two-body loss rate. For the trap offset fields $E_{\text{off}} = 0.50\text{kV/cm}$ and $E_{\text{off}} = 2.37\text{kV/cm}$, we obtain $\Gamma_{\text{coll}} = 0.20\text{Hz}$ and $\Gamma_{\text{coll}} = 0.09\text{Hz}$, respectively. As mentioned in section 3.2.1, these loss rates are about a factor of 5 to 10 lower than the measured single-body loss rates and thus hard to disentangle from velocity-dependent changes of Γ in our trap. Therefore, to extract a precise value for k from collision experiments performed in our trap, the simple two body-loss model is not sufficient, whereas the model presented in this thesis is well suited.

The two-body loss rate k is a molecule specific parameter that is independent of the density of the trapped ensemble. To probe this we perform collision measurements for four different densities of trapped molecules, which we adjust via the maximum transverse trapping field in the connection guide. This straight piece of quadrupole guide connects the buffergas cell with the centrifuge decelerator, illustrated in 3.1. We tune the maximum transverse trapping field from $E_{\text{conn}} = 2\text{kV/cm}$ to $E_{\text{conn}} = 20\text{kV/cm}$. Thereby we vary the density of molecules in the trap by more than a factor of four, as can be seen in Figure 3.16. As expected k does not change as a function of the density of trapped molecules for both trap offset fields $E_{\text{off}} = 0.50\text{kV/cm}$ and $E_{\text{off}} = 2.37\text{kV/cm}$.

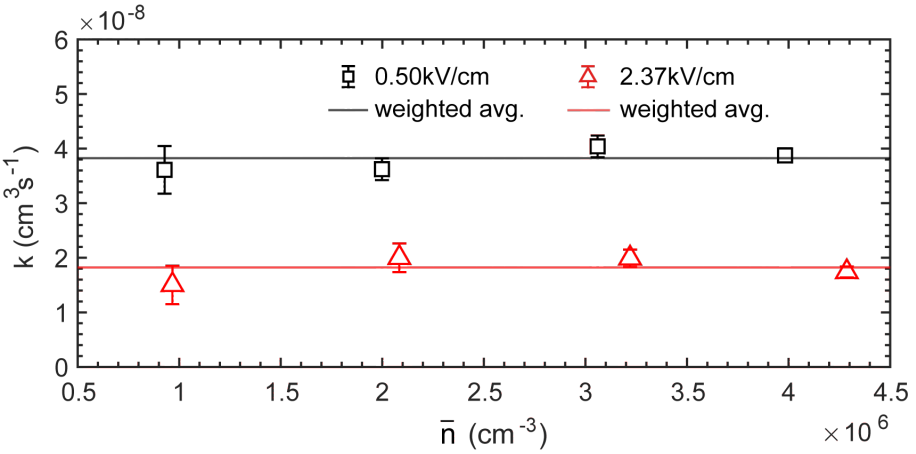

Figure 3.16: *Two-body loss rate k as a function of the integrated trapped density (see Equation 3.7). Black and red show measured data and weighted average for a trap offset field of $E_{off} = 0.50kV/cm$ and $E_{off} = 2.37kV/cm$, respectively.*

3.2.6 Electric field dependent collisions – dipolar relaxation

The loss rates depicted in Figure 3.16 show no dependence on the density of the trapped ensembles but clearly a statistically significant difference between the two trap offsets $V_{\text{off}} = 0.05V_\mu$ and $V_{\text{off}} = 0.30V_\mu$. This indicates an electric field dependence of the collision process which we can investigate with the methods developed in the previous section.

Therefore we measure the collisional loss from our microstructured electric trap caused by A–B collisions for six different trap offsets between $V_{\text{off}} = 0.05V_\mu$ and $V_{\text{off}} = 0.30V_\mu$. Using the analytic expression for δn, derived in section 3.2.5, we are able to extract the rate coefficients k, depicted in red in Figure 3.17 as a function of the applied trap offset field E_{off}. The two-body loss rate k shows a clearly statistically significant electric field dependence of 13 σ when we vary the homogeneous offset field from $E_{\text{off}} = 0.50\text{kV/cm}$ to $E_{\text{off}} = 2.37\text{kV/cm}$ and thereby suppress k by more than a factor of two.

The suppression of collision induced trap losses without affecting thermalising elastic collisions is a key ingredient to realise efficient rethermalisation of the trapped ensemble for potential future evaporative cooling [164] of naturally occurring polar molecules. Therefore it is essential for us to understand the loss mechanism from our electric trap and control the collision process. We theoretically model the collisions in our trap considering elastic k_{el} and inelastic k_{in} contributions to the calculated two-body loss rate k_{th}. The final result is depicted in black in Figure 3.17, showing excellent agreement with the measured loss rates, after rescaling the densities of trapped molecules by a factor of about 0.5. The rescaling is necessary due to inaccuracies in our density calibration and we refer the interested reader to section 3.1.4 for additional information. At this point we want to note that we scaled the densities in all measurements presented in this thesis accordingly to get a consistent picture.

Elastic Collisions

When calculating the two-body loss rate due to elastic collisions k_{el} we need to consider two contributions; the corresponding cross-section σ_{el} and the probability P_{loss} for a molecule to be lost from the trap in an elastic collision process [177]. Due to the molecules' large mean collision energy of $\bar{E}_{coll} = 0.4K \cdot k_B$ in the trap many partial waves contribute to the collision process. Thus we can use the semi-classical Eikonal approximation [178] to calculate the differential cross-section $\frac{d\sigma}{d\Omega}(v_{\text{rel}}, \theta)$, which is a function of the relative velocity of the colliding particles v_{rel} and the scattering angle θ. In this calculation we only consider the isotropic part of the dipole-dipole interaction $V_{\text{dd}}(r) = -\langle d \rangle^2 / 4\pi\epsilon_0 r^3$. The differential cross-section $\frac{d\sigma}{d\Omega}$ is illustrated in Figure 3.18 (a) as a function of the relative velocity for selected scattering angles between $\theta = 0°$ and $\theta = 180°$. Throughout all scattering angles the differential cross-section gets smaller for increasing relative velocities and scattering angles. The dependence of $\frac{d\sigma}{d\Omega}$ on θ is even more visible in Figure 3.18 (b) showing

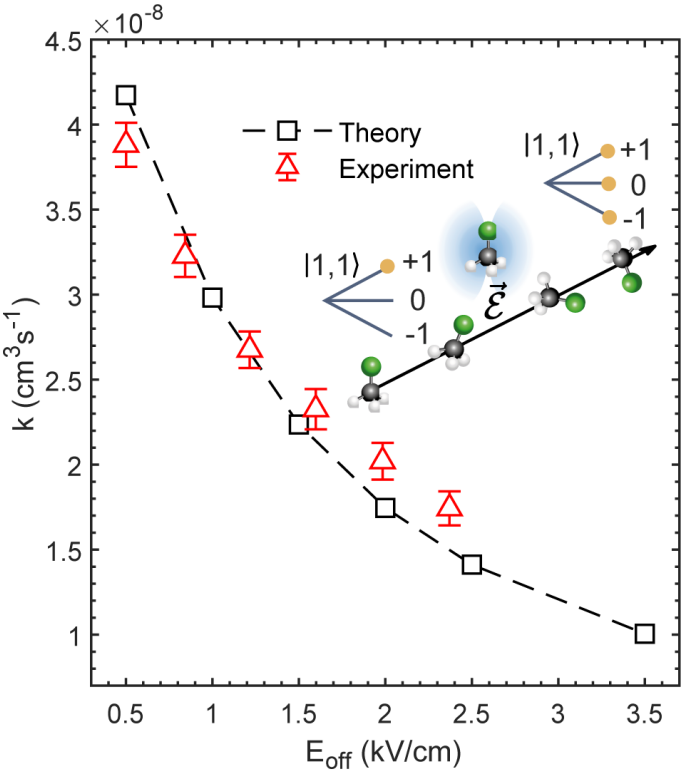

Figure 3.17: *Electric field dependence of the two-body loss rate k. The experimental data is shown in red, whereas calculation results, including inelastic and elastic collision processes, are depicted in black. To overlap theory and experiment, we globally scaled the measured densities by a factor of about* 0.5*. The inset illustrates the inelastic collisions process. Two molecules fly past each other in the presence of the trap offset field and interact via the dipole-dipole interaction. This leads to a redistribution of the initially trapped population over trapped and untrapped M-sublevels of the $|J = 1, K = 1\rangle$ state.*

the differential cross-section averaged over the relative velocities in the trap. The fast decrease of $\frac{d\sigma}{d\Omega}$ as a function of θ can be explained by the semi-classical character of the collision process, which strongly favors scattering in forward direction [177]. We obtain the total elastic cross-section for the molecules in the trap by integrating the differential cross-section over the full solid angle in 4π [177]

$$\sigma_{\mathrm{el}} = \int_0^{2\pi} \int_0^{\pi} \frac{d\sigma}{d\Omega}(v_{\mathrm{rel}}, \theta) \sin\theta d\theta d\phi. \tag{3.21}$$

We want to mention here that σ_{el} varies for different trap offset fields due to the dependence of the relative velocity distribution on E_{off} (see section 3.2.2). However since the collision process itself does not show an electric field dependence the impact of E_{off} onto the elastic cross-section is small. We can exemplary look at two trap offset fields, namely $E_{\mathrm{off}} = 0.50\mathrm{kV/cm}$ and $E_{\mathrm{off}} = 2.37\mathrm{kV/cm}$ and the respective

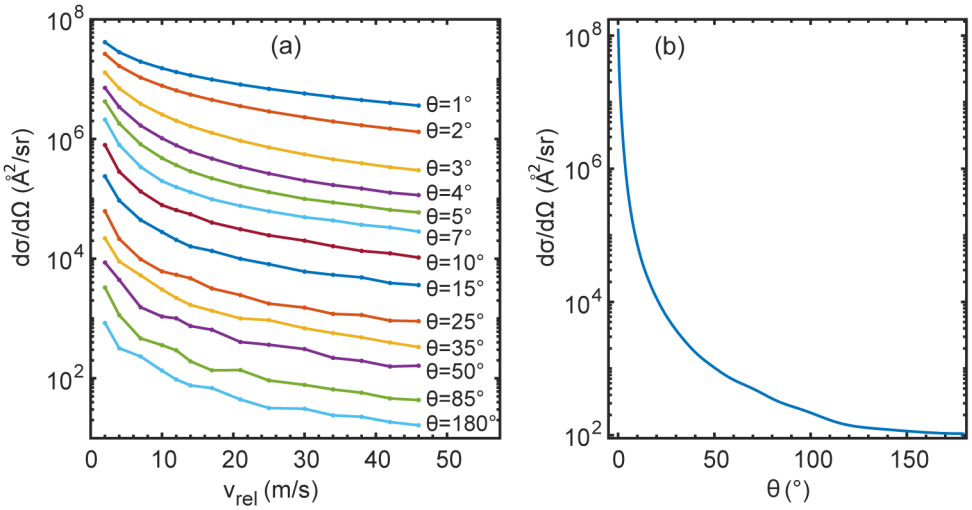

Figure 3.18: *(a) Differential elastic cross-section as a function of the relative velocity v_{rel} for selected scattering angles θ. (b) Differential cross-section averaged over the relative velocity distribution in the trap $D(v_{rel})$ plotted against the scattering angle θ.*

elastic collision cross-sections, $\sigma_{\mathrm{el}} = 6.97 \cdot 10^{-12}\mathrm{cm}^2$ and $\sigma_{\mathrm{el}} = 7.50 \cdot 10^{-12}\mathrm{cm}^2$, showing only a small electric field dependence.

These values are about a factor of 3.5 larger than the elastic cross-section for collisions in the guide, $\sigma_{\mathrm{el}} = 2.0 \cdot 10^{-12}\mathrm{cm}^2$, calculated in 2017 [78, 177]. When comparing elastic collisions in the guide and in the trap we need to consider the relative velocity of the colliding particles and the dipole moment d_{avg}, averaged over the populated rotational states, since the elastic cross-section scales as $\sigma_{el} \propto d_{avg}^2/v_{\mathrm{rel}}$ [178]. The mean relative velocities are given by $\bar{v}_{\mathrm{rel}} = 28.2\mathrm{m/s}$ and $\bar{v}_{\mathrm{rel}} = 19.8\mathrm{m/s}$ and the averaged dipole moments by $d_{avg} = 0.56\mathrm{D}$ and $d_{avg} = 0.83\mathrm{D}$ for the measurements in the guide and in the trap for $E_{\mathrm{off}} = 0.50\mathrm{kV/cm}$, respectively. The mean relative velocity in the guide is larger than in the trap, since molecules are only confined in the transversal direction, wheras in the trap molecules are confined in all three dimensions. This results in a larger longitudinal velocity in the guide and thereby in a larger mean relative velocity. The averaged dipole moment d_{avg} is smaller for the measurements performed in 2017 than for the measurements shown in this thesis as the buffergas cell was operated at about 7.5K instead of 4K, resulting in more rotational states being populated and therefore in a smaller value for d_{avg}. Taking all these aspects into account we expect a 3.1 times larger elastic cross-section in the trap than in the guide. However we observe σ_{el} being even about a factor of 3.5 larger in the trap which we attribute to the fact that we do not use the mean relative velocity for the calculations in thesis but average over the measured relative velocity distributions, depicted in Figure 3.10 (b).

Since we measure collisional loss with the measurement scheme described in section 3.2.1 we need to not only calculate the elastic collision cross-section but more-

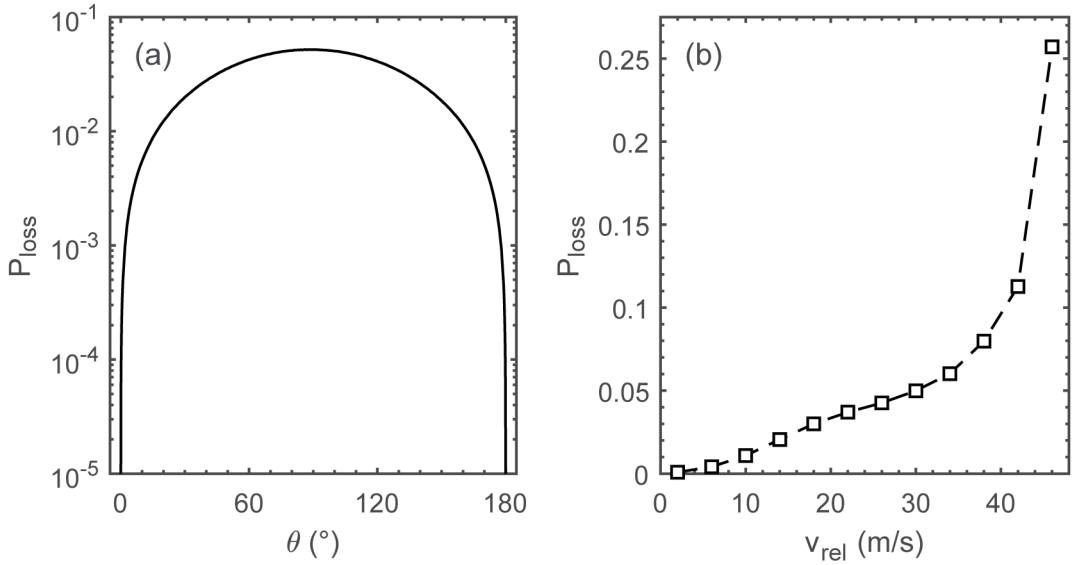

Figure 3.19: *(a) Elastic collision induced loss probability P_{loss}, averaged over the relative velocity distribution $D(v_{rel})$ in the trap for an offset field of $E_{off} = 2.37 kV/cm$. (b) P_{loss} as a function of the relative velocity of the colliding molecules averaged over all possible scattering angles θ.*

over the elastic loss rate coefficient k_{el}. Therefor we have to consider the likelihood $P_{\mathrm{loss}}(v_{\mathrm{rel}}, \theta)$ for a molecule to be lost from the trap in an elastic collision process as a function of the scattering angle θ and the relative velocity v_{rel} [114]. These calculations are performed utilising Monte Carlo simulations for a given trap offset field E_{off} and the respective electric field distribution in the trap, that resembles the molecules' position distribution. We randomly sample the molecules from the electric field distribution and two molecules can only collide if the electric field value is identical for both of them. Of course, we need to consider that according to the electric field value kinetic energy is transformed into potential energy. We randomly sample θ from a flat distribution from 0 to π and v_{rel} from the relative velocity distribution in the trap $D(v_{\mathrm{rel}})$ obtained from time-of-flight measurements (see section 3.2.2). Elastic collisions lead to an energy transfer between the colliding molecules, which we calculate in the centre of mass frame [177]. To determine $P_{\mathrm{loss}}(v_{\mathrm{rel}}, \theta)$, we compare the molecule's total energy after the collision process with the trap depth in the laboratory frame. If the total energy of a molecule is higher than the trap depth the molecule will be lost from the trap. In addition, there is a second contribution to $P_{\mathrm{loss}}(v_{\mathrm{rel}}, \theta)$ we have to consider, as the loss probability from our trap shows a $E^{5/2}$ energy dependence for molecules with a linear Stark shift. To account for this we compare the molecules' kinetic energy before and after the collision process in the laboratory frame and consider the change in the loss probability accordingly. In general both of the colliding molecules can be lost from the trap but to avoid double counting we assume only one of the two to be lost [114].

Figure 3.19 (a) shows P_{loss}, averaged over the relative velocity distribution in

the trap, as a function of the scattering angle θ. We observe the expected behavior with the loss probability being maximal for a scattering angle of $\pi/2$ and in addition a steep decrease below 3° and above 178°, similar to the results obtained in 2017 for collisions in the guide [177]. Figure 3.19 (b) depicts P_{loss}, averaged over θ, as a function of the relative velocity v_{rel}, showing that the loss probability increases by more than three orders of magnitude from $v_{\text{rel}} = 2\text{m/s}$ to $v_{\text{rel}} = 46\text{m/s}$. With this we have everything in place to calculate the elastic loss cross-section as a function of v_{rel} [177]

$$\sigma_{\text{el,loss}}(v_{\text{rel}}) = \int_0^{2\pi} \int_0^{\pi} \frac{d\sigma}{d\Omega}(v_{\text{rel}}, \theta) P_{\text{loss}}(v_{\text{rel}}, \theta) \sin\theta d\theta d\phi, \tag{3.22}$$

and the corresponding two-body loss rate $k_{\text{el}}(v_{\text{rel}}) = \sigma_{\text{el,loss}}(v_{\text{rel}}) \cdot v_{\text{rel}}$. By averaging over the relative velocity distribution in the trap we obtain a loss rate of $k_{\text{el}} = 3.84 \cdot 10^{-11}\text{cm}^3\text{s}^{-1}$ for a trap offset field of $E_{\text{off}} = 2.37\text{kV/cm}$.

We can compare this value with the calculation result for collisions in the guide obtained in 2017 [177], $k_{\text{el}} = 3.46 \cdot 10^{-10}\text{cm}^3\text{s}^{-1}$, which is larger by one order of magnitude. When comparing the two collision experiments we have to keep in mind that in 2017 molecules were only transversely confined and we observed longitudinal velocities up to 80m/s [114]. In contrast, for the measurements presented in this thesis, molecules are confined in all three dimensions in our electric trap with a cut-off velocity not exceeding 25m/s. Therefore, as already mentioned, we observe a larger elastic cross-section σ_{el} in the trap due to the lower relative velocity v_{rel}. On the other, the loss probability in the guide is larger due to the larger longitudinal velocity v_z. In the end these are two competing effects, resulting in a roughly nine times larger loss rate k_{el} for the collisions in the guide compared to the collision measurements in the trap.

Inelastic Collisions

In the following discussion we present the contribution of inelastic collisions to the calculated two-body loss rate k_{th}. Therefor we consider the Langevin capture model [179] and long-ranged dipolar collisions. To describe dipolar collisions between the molecules in our trap we start by considering two molecules in the presence of an electric field flying past each other with relative velocity v_{rel} on a straight line trajectory, as schematically illustrated by the inset in Figure 3.17 for two molecules in the $|J = 1, K = 1\rangle$ state. The molecules interact via the long ranged dipole-dipole interaction, redistributing the initial population over trapped and untrapped M-sublevels. Solving the Hamiltonian for this system, we then integrate over the untrapped population after the collision process to obtain the loss cross-section σ_{loss} which is related to the loss rate as $k_{dd} = \sigma_{loss} \cdot v_{rel}$.

The Hamiltonian, describing the dipolar collision process between two molecules in the presence of an electric field is given by [183]

$$\hat{H} = \hat{H}_s + \hat{H}_{dd}. \tag{3.23}$$

The first term describes the interaction of the molecules' dipole moments, given by the operator $\hat{\boldsymbol{d}}_i$ for particle $i = 1, 2$, with an externally applied electric field $\boldsymbol{E}$, as

$$\hat{H}_s = -(\hat{\boldsymbol{d}}_1 + \hat{\boldsymbol{d}}_2) \cdot \boldsymbol{E}. \tag{3.24}$$

Making use of the Wigner-Eckhart-theorem [149] allows us to evaluate the matrix elements of the Stark Hamiltonian $\hat{H}_{s,i} = -\hat{\boldsymbol{d}}_i \cdot \boldsymbol{E}$ in the single-particle symmetric top basis $|JKM\rangle$, introduced in section 2.2.1. For an electric field pointing in z-direction of the lab frame, $\boldsymbol{E} = E\boldsymbol{e}_z$, the matrix elements are given by [13]

$$\begin{aligned}&\langle J_i' K_i' M_i' |\, \hat{H}_{s,i} \,| J_i K_i M_i \rangle = \\ &-dE(-1)^{M_i'-K_i'} \sqrt{(J_i'+1)(J_i+1)} \begin{pmatrix} J_i' & 1 & J_i \\ -K_i' & 0 & K_i \end{pmatrix} \begin{pmatrix} J_i' & 1 & J_i \\ -M_i' & 0 & M_i \end{pmatrix}.\end{aligned} \tag{3.25}$$

However, to theoretically model dipolar collisions between a pair of molecules we need to describe our system in the two-particle basis which is given by the tensor product of single-particle states as $|J_1 K_1 M_1\rangle \otimes |J_2 K_2 M_2\rangle = |J_1 K_1 M_1, J_2 K_2 M_2\rangle$. In the two-particle basis the matrix elements for the interaction between the molecules and an electric field can be obtained from the results in the single-particle as

$$\hat{H}_s = \hat{H}_{s,1} \otimes \mathbb{1} + \mathbb{1} \otimes \hat{H}_{s,2}. \tag{3.26}$$

Figure 3.20 (a) and (b) show the Stark shifts of a CH_3F molecule in the $|J = 1, K = 1\rangle$

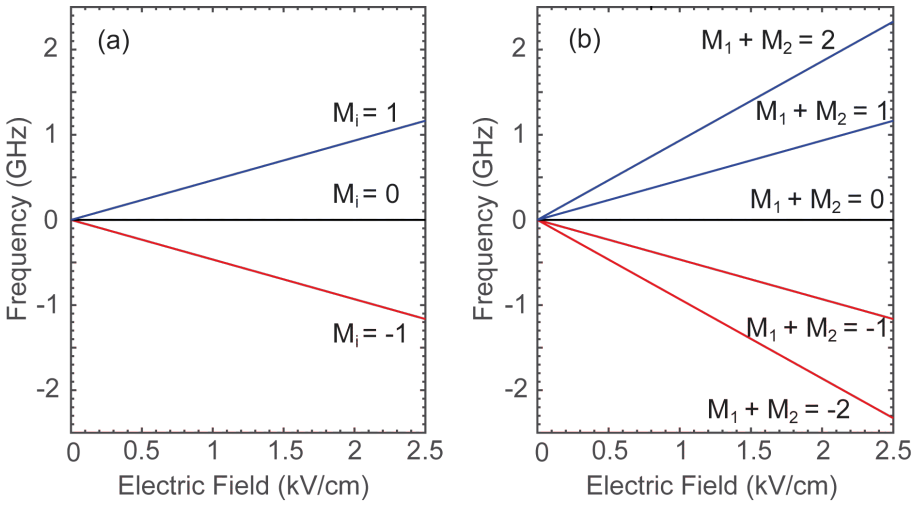

Figure 3.20: *Stark shift of CH_3F in the $|J = 1, K = 1\rangle$ state in the (a) single-particle and (b) two-particle basis. Only the states color-coded in blue are low-field seeking and thus trappable. The states illustrated in black and red will be lost from the trap.*

state in the single-particle and two-particle basis, respectively. As introduced in section 2.2.1, fluoromethane is a symmetric top molecule, so that there is a degenerate

pair of opposite parity states for each $|K| > 0$. Thus we observe a linear electric field response in Figure 3.20 (a) where its sign depends on the product of K and M. We use the convention that a positive signed M-value shows a low-field-seeking electric field response, such that $K = -|K|$. Figure 3.20 (b) illustrates the Stark shift for CH_3F in the two-particle basis $|J_1 = 1, K_1 = 1, J_2 = 1, K_2 = 1\rangle$. Since we have to consider all possible combinations of the different M-levels of the single-particle basis, the Stark shift depicted in Figure 3.20 (b) shows five instead of three levels. Here, the sign of the Stark shift is given by the product of K and $M_1 + M_2$, with M_i being the M-quantum number of particle $i = 1, 2$. At this point we want to note that only molecules in a low-field-seeking state, color-coded in blue in Figure 3.20 (a) and (b), can be trapped. Whereas molecules showing no electric field response, color-coded in black in Figure 3.20, or molecules in high-field-seeking states, depicted in red, will be eventually lost from the trap.

In addition to the interaction of the molecules with an external electric field we also need to consider the second contribution to the Hamiltonian $\hat{H}$ in Equation 3.23, the dipole-dipole interaction, described by [183]

$$\hat{H}_{dd} = \frac{\hat{\boldsymbol{d}}_1 \cdot \hat{\boldsymbol{d}}_2 - 3(\hat{\boldsymbol{d}}_2 \cdot \boldsymbol{e}_r)(\boldsymbol{e}_r \cdot \hat{\boldsymbol{d}}_1)}{4\pi\epsilon_0 |\boldsymbol{r}(t)|^3} \tag{3.27}$$

with the vacuum permittivity ϵ_0, the unit vector $\boldsymbol{e}_r$ pointing from molecule 1 to molecule 2 and the time-dependent distance between the two molecules, $\boldsymbol{r}(t)$. Again we can evaluate the matrix elements, here directly in the two-particle basis [183, 13]

$$\begin{aligned}
&\langle J_1' K_1' M_1', J_2' K_2' M_2' | \, \hat{H}_{dd} \, | J_1 K_1 M_1, J_2 K_2 M_2 \rangle = \\
&-\sqrt{30} \frac{d^2}{4\pi\epsilon_0 |\boldsymbol{r}(t)|^3} (-1)^{M_1' - K_1' + M_2' - K_2'} \sqrt{(2J_1'+1)(2J_1+1)(2J_2'+1)(2J_2+1)} \\
&\times \sum_{p=-2}^{2} (-1)^p C_{-p}^{(2)}(\theta, \phi) \sum_{m=-1}^{1} (-1)^p \begin{pmatrix} 1 & 1 & 2 \\ m & p-m & -p \end{pmatrix} \begin{pmatrix} J_1' & 1 & J_1 \\ -K_1' & 0 & K_1 \end{pmatrix} \\
&\qquad \times \begin{pmatrix} J_1' & 1 & J_1 \\ -M_1' & m & M_1 \end{pmatrix} \begin{pmatrix} J_2' & 1 & J_2 \\ -K_2' & 0 & K_2 \end{pmatrix} \begin{pmatrix} J_2' & 1 & J_2 \\ -M_2' & p-m & M_2 \end{pmatrix}
\end{aligned} \tag{3.28}$$

where $C_{-p}^{(2)}(\theta, \phi)$ are the unnormalised spherical harmonics. The dipole-dipole interaction redistributes the initially trapped population over low- and high-field seeking states in the trap, according to the selection rules given by Equation 3.28. This is known as dipolar relaxation, a well known effect from atomic physics [186, 187, 188, 189].

We consider the molecules' movement in the trap with the time-dependent interparticle distance $\boldsymbol{r}(t)$. Therefor we fix the position of molecule 1 at the origin of the coordinate system, which is defined by the externally applied electric field $\boldsymbol{E} = E\boldsymbol{e}_z$, pointing in z-direction, as depicted in Figure 3.21. Molecule 2 is moving past molecule 1 on a classical straight line trajectory described by the unit vector

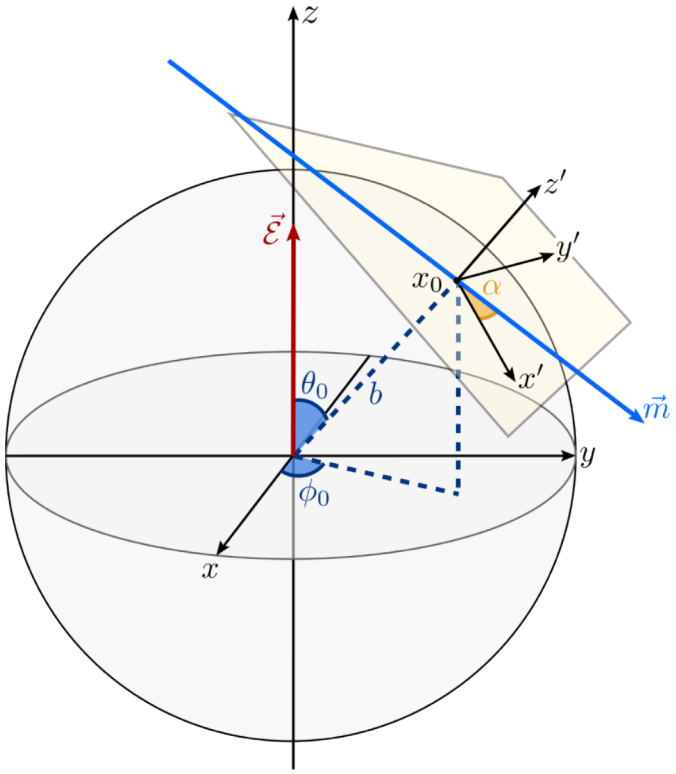

Figure 3.21: *Illustration of the coordinate system we use to calculate dipolar collisions between a pair of molecules in the trap. The externally applied electric field defines the z-axis of the system. Molecule 1 is fixed at the origin of the sphere, while molecule 2 is moving in the x'-, y'-plane in the direction given by the unit vector* $\hat{\boldsymbol{m}}$.

$\hat{\boldsymbol{m}}$, which is related to the inter-particle distance according to $\boldsymbol{r}(t) = b \cdot \boldsymbol{x_0} + v_{rel} t \cdot \hat{\boldsymbol{m}}$, with v_{rel} being the relative velocity. The minimal distance between the two particles, or equivalently the distance between the origin of the coordinate system and $\boldsymbol{x_0}$, is given at time $t = 0$ by the impact parameter b. Thus $\boldsymbol{r}(t)$ with $t \in [-\infty, \infty]$ has to lie within a plane perpendicular to b and can go through $\boldsymbol{x_0}$ in any direction. We account for this with the angle $\alpha \in [0, 2\pi]$ between the x-axis of the plane x' and the unit vector $\hat{m}$ along the trajectory, as depicted in Figure 3.21. The position of $\boldsymbol{x_0}$ can be at any point on the sphere and is defined by $\theta_0 \in [0, \pi]$ and $\phi_0 \in [0, 2\pi]$, the azimuthal and polar angle of a spherical coordinates system. Taking all these aspects into consideration the movement of molecule 2 through the trap can be expressed by the time-dependent spherical coordinates, defined as

$$r = |\boldsymbol{r}| = \sqrt{b^2 + v_{rel}^2 t^2} \tag{3.29}$$

$$\theta = \cos^{-1}\left(\frac{r_z}{|\boldsymbol{r}|}\right) = \cos^{-1}\left(\frac{b\cos\theta_0 - v_{rel} t \cos\alpha \sin\theta_0}{\sqrt{b^2 + v_{rel}^2 t^2}}\right) \tag{3.30}$$

$$\phi = \tan^{-1}\left(\frac{r_y}{r_x}\right) = \tan^{-1}\left(\frac{v_{rel}t\sin\alpha}{b\sin\theta_0 + v_{rel}t\cos\alpha\cos\theta_0}\right) \tag{3.31}$$

which we insert into Equation 3.27 to model the collision process. Due to the electric field $\boldsymbol{E} = E\boldsymbol{e_z}$ pointing in z-direction we have a cylindrical symmetry in our model with the z-axis being the symmetry axis. Thus we have set $\phi_0 = 0$ in the expressions for θ and ϕ since it only adds a phase factor of 2π.

The trajectory of molecule 2 is assumed to be a classical straight line trajectory, that is not altered by the dipole-dipole interaction. In the following we will show that this is a reasonable assumption for the molecules in our trap due to their large mean collision energy of $\langle E_{coll}\rangle = 0.4K \cdot k_B$. Since trajectories of molecules with low kinetic energy are more prone to be altered by the dipole-dipole potential

$$V_{dd}(r,t) = -\frac{d^2}{4\pi\epsilon_0|\boldsymbol{r}(t)|^3} \tag{3.32}$$

than trajectories of fast molecules we will exemplary look at a pair of molecules moving very slowly in our electrostatic trap with a relative velocity as small as $v_{rel} = 5\text{m/s}$. We assume the trap offset field to be $E_{\text{off}} = 0.50\text{kV/cm}$ and chose the impact parameter such that the transition probability is maximum, $b = \sqrt{\sigma_{loss}(E_{off}, v_{rel})/\pi}$. To see how much the dipole-dipole potential V_{dd}, given by Equation 3.32, alters the trajectory of molecule 2 we need to compare the momentum of molecule 2, $p_{mol} = m \cdot v_{rel}$, flying past molecule 1 to the momentum transfer caused by V_{dd}, which can be calculated as

$$p_{\text{dd}} = \int_{-\infty}^{\infty} \frac{dV_{\text{dd}}(r,t)}{dr} dt. \tag{3.33}$$

To give an upper bound to the impact of the dipole-dipole potential on the trajectory of molecule 2 we assume p_{dd} to be perpendicular to p_{mol}, resulting in a deflection of $\sim 10°$. In addition to giving an upper bound for the deflection we can also look at the impact of the dipole-dipole potential on the trajectory for the mean relative velocity in the trap $\bar{v}_{\text{rel}} = 19.8\text{m/s}$, where molecule 2 is only deflected by $\sim 0.7°$. Taking this into account in combination with the relative velocity distribution in the trap, illustrated in Figure 3.10 (b), we can conclude that it is reasonable to describe the trajectories of the molecules in our trap by classical straight line trajectories not being altered by V_{dd}.

We want to note that in general there is a third contribution to the Hamiltonian $\hat{H}$ (Equation 3.23), namely $\hat{H}_{rot}$, the Hamiltonian associated with the rotational energy of the molecules [190]. However, population transfer between a pair of states can only occur if the transition is non-adiabatic, where the likelihood of this population transfer depends on the energy mismatch between the states coupled by $\hat{H}_{dd}$ and the relative velocity of the colliding particles [191]. The larger the relative velocity between the molecules is, the more likely it is for a transition to be

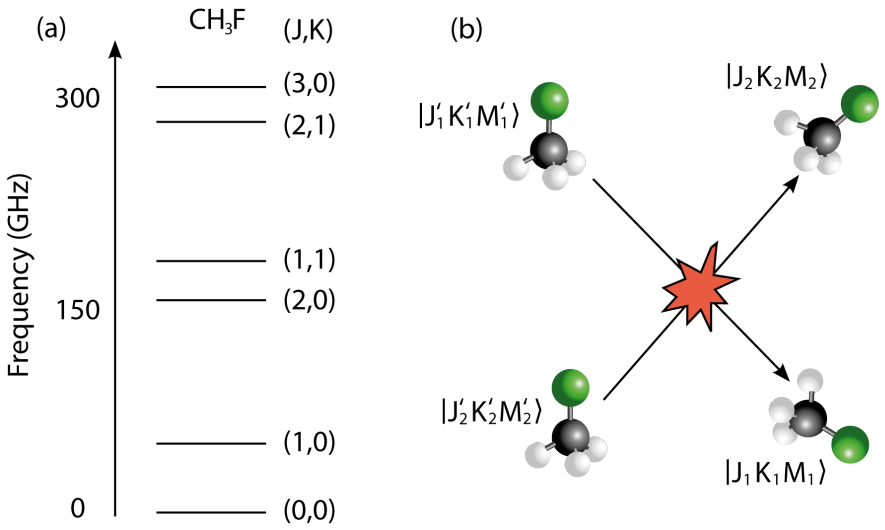

Figure 3.22: *(a) Rotational energies of different (J,K)-manifolds in CH_3F. (b) Schematic illustration of the collision process between two CH_3F molecules.*

non-adiabatic. In contrast, the larger the energy difference is, the smaller is the likelihood for a non-adiabatic transfer. In the following we will show that collision induced population transfer with the energy mismatch between the initial and the final state of the two-particle system being on the order of the rotational energy is highly unlikely and can be neglected. Therefore we follow the calculations performed by Zeppenfeld [191], utilising a simple back-of-the-envelope estimation based on Landau-Zener theory. For the only significantly populated (J,K)-manifolds in the trap, namely (1,1) and (2,1) we arrive at a maximum possible energy mismatch of $\Delta/h \approx 15$ GHz for a state changing collision using Equation 3.28 with $\phi = 0$ and $\theta = \pi/2$. This is significantly smaller than the ~ 102 GHz rotational splitting between the (1,1)- and the (2,1)-manifold in CH_3F [192, 193], shown in Figure 3.22 (a). Thus it is justified to consider the rotational levels in our system in separate collision calculations weighted by their respective population in the trap. In these calculations the Hamiltonian $\hat{H}$ describing the system is given by equation 3.23, so that $\hat{H}_{rot}$ is not taken into account. This reduces the dimensions of the Hamiltonian and thereby saves computation time, which is necessary since the calculations are very computation intense with an estimated total calculation time of roughly seven months on up to six computers running in parallel.

In total we need to perform calculations for collisions within the (1,1)- and within the (2,1)-manifold as well as for a specific collision process between molecules from the (1,1)- and the (2,1)-manifold which we will present in the following using a representative example. Molecule 1 with initial state $|J_1' = 1, K_1' = 1, M_1' = 1\rangle$ collides with molecule 2 with initial state $|J_2' = 2, K_2' = 1, M_2' = 1\rangle$, as schematically depicted in Figure 3.22 (b). The interaction between the molecules is mediated by $\hat{H}_{dd}$ with exemplary final states $|J_1 = 2, K_1 = 1, M_1 = 0\rangle$ and $|J_2 = 1, K_2 = 1, M_2 = 0\rangle$.

In this example both molecules are no longer in a trappable state and therefore will be lost from the trap. The redistribution of the population however just took place within the respective M-sublevels. Therefore the energy mismatch between the initial and final state of the collision process is given by the Stark splitting for the two-particle system and thus on the order of up to a few GHz. However if the final state of molecule 2 in the above example would be $|J_2 = 2, K_2 = 1, M_2 = 0\rangle$, the collision process would be highly unlikely due to the large energy mismatch of ~ 102 GHz between the initial and the final state and thus can be neglected.

In order to calculate the loss cross-section σ_{loss} and the two-body loss rate k_{dd} for the dipolar collisions in our trap we need to determine the state population after the collision process by solving the Schrödinger equation [191]

$$i\hbar\frac{d}{dt}\left|\Psi(t)\right\rangle = \hat{H}\left|\Psi(t)\right\rangle \tag{3.34}$$

utilising the Hamiltonian given by Equation 3.23. As mentioned in the previous paragraph, we can perform separate calculations for the individual (J,K)-manifolds and weight the results according to the state distribution in the trap. For each of these calculations the initial state vector $|\Psi(t = -\infty)\rangle$ is given by the population of the individual M-levels of the two-particle system in the trap, which we obtain using the state distribution measurement introduced in section 3.2.3. We solve the Schrödinger equation and thereby obtain the state population after the collision process in high field seeking states $|\Psi_{hfs}(t = \infty, \theta_0, b, \alpha)|^2$ for a given relative velocity v_{rel} and a given trap offset field E_{off}. We obtain the loss cross-section by integrating the untrapped population over all possible trajectories and the full solid angle 4π

$$\sigma_{\text{loss}} = \int_0^{\pi}\int_0^{\infty}\int_0^{2\pi}\int_0^{2\pi} \left|\Psi_{hfs}(t = \infty, \theta_0, b, \alpha, E_{\text{off}}, v_{\text{rel}})\right|^2 \sin(\theta_0)\; d\theta_0\; db\; d\phi_0\; d\alpha. \tag{3.35}$$

Due to the underlying cylindrical symmetry in our system the integral over ϕ_0 just gives a phase factor of 2π, whereas for each θ_0, α and impact parameter b, we need to solve the Schrödinger equation to obtain the population in untrapped states $|\Psi_{hfs}(t = \infty, \theta_0, b, \alpha)|^2$. For the two angles $\theta_0 \in [0, \pi]$ and $\alpha \in [0, 2\pi]$, we use a step size of 20° and for the impact parameter b which we vary from $b_{\text{min}} = 5 \cdot 10^{-10}$m to $b_{\text{max}} = 1 \cdot 10^{-7}$m we use a step size of $db = 5 \cdot 10^{-10}$m. This ensures a good compromise between reasonable computation time and accurate calculation results, where finer steps for θ_0, α and b improve the accuracy only in the low single digit percentage range. We solve the Schrödinger equation for 14 different relative velocities $v_{\text{rel}} = [2, 4, 7, 10, 12, 14, 17, 21, 25, 30, 34, 38, 42, 46]$m/s, covering the relative velocity distribution in the trap (see Figure 3.10 (b)) and 6 different trap offset fields $E_{\text{off}} = [0.5, 1.0, 1.5, 2.0, 2.5, 3.5]$kV/cm. In total this adds up to a calculation time of roughly seven months on up to six computers running in parallel. Figure 3.23 (a) and (b) depict σ_{loss} for the (1,1)- and (2,1)-manifold, as a function of the relative velocity for six different trap offset fields. For all data shown in

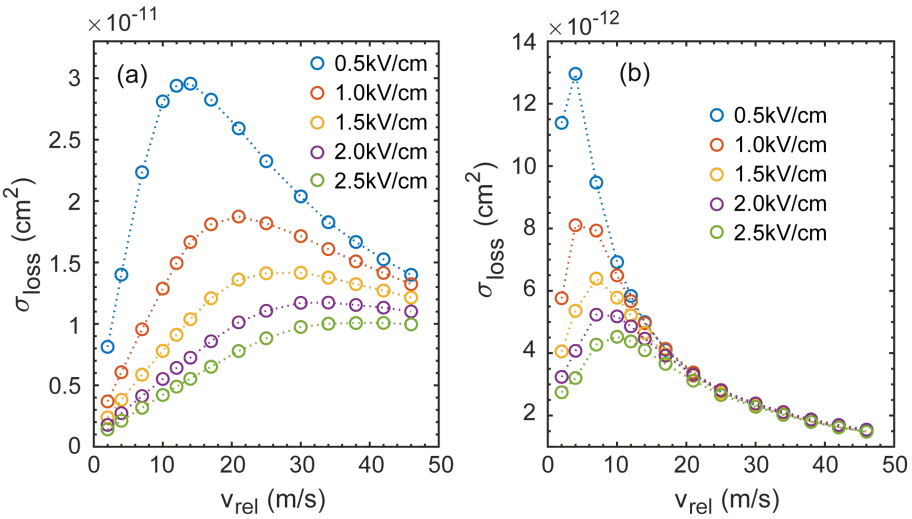

Figure 3.23: *(a) and (b) show the loss cross-sections for the (1,1)- and (2,1)-manifold as a function of the relative velocity v_{rel} of the colliding molecules, respectively. Both plots include data for trap offset fields from $E_{off} = 0.5kV/cm$ to $E_{off} = 2.5kV/cm$.*

Figure 3.23 (a) and (b) the loss cross-section σ_{loss} increases from the minimal relative velocity used in our calculations, $v_{\text{rel}} = 2\text{m/s}$ up to a maximum value before it starts to decrease again. The increase of σ_{loss} can be explained by the applied trap offset field interacting with the molecules' dipole moments, resulting in a Stark splitting or equivalently a detuning Δ between the states coupled by H_{dd}. For a population transfer from a low-field-seeking to a high-field-seeking state to occur the transition has to be non-adiabatic [191]. According to Landau-Zener theory this is fulfilled if the transition rate $\gamma = hv_{\text{rel}}/r$, with r being the interparticle distance at which the transition occurs, is larger than the energy mismatch between the state coupled by the dipole-dipole interaction, $\Delta < \gamma$ [191]. Thus a certain minimal relative velocity is required to overcome the energy splitting between the M-sublevels and the probability for a loss to occur becomes larger for increasing v_{vrel}, until the transition rate is clearly larger than Δ. From this point on σ_{loss} starts to decrease for increasing relative velocities.

Along these lines we can also observe in Figure 3.23 (a) and (b) that with increasing electric field strength and thereby increasing Stark splittings between trapped and untrapped states, the maximum of the loss cross-section shifts to higher velocities, since a larger transition rate is required for a non-adiabatic transfer. In addition, the maximum value for σ_{loss} occurs for higher relative velocities in the (1,1)- than in the (2,1)-manifold due to the larger Stark splitting. Besides different Stark shifts for the molecules in the two (J,K)-manifolds there is another difference, the number of M-sublevels, given by $2(J+1)$. As a consequence losses are more pronounced for molecules in the (1,1)- than in the (2,1)-manifold due to the larger fraction of high-field-seeking states, visible in Figure 3.23 (a) and (b).

We obtain the loss cross-section for the trapped ensemble at a given offset field E_{off} by summing σ_{loss} with statistical weights according to relative velocity and state distribution in the trap. This allows us to obtain the rate coefficient due to dipolar relaxation as $k_{\text{dd}}(E_{\text{off}}) = \sigma_{\text{loss}}(E_{\text{off}}) \cdot v_{\text{rel}}$.

In addition to the long-ranged dipole-dipole interaction we estimate further inelastic collisional loss by the Langevin capture model [179] with the corresponding loss rate

$$k_{\text{lv}}(v_{\text{rel}}) = 3\pi v_{\text{rel}} \left(\frac{d_{\text{avg}}^2}{4\pi\epsilon_0 v_{\text{rel}}^2} \right)^{2/3} . \tag{3.36}$$

Here d_{avg} is the dipole moment averaged over the state distribution in the trap and ϵ_0 the vacuum permittivity. By averaging $k_{\text{lv}}(v_{\text{rel}})$ over the relative velocity distribution in the trap we obtain $k_{\text{lv}} = 6.67 \cdot 10^{-10}\text{cm}^3\text{s}^{-1}$ for a trap offset field of $E_{\text{off}} = 0.50\text{kV/cm}$. We want to note that the loss rate changes slightly for different trap offset fields due to the dependence of the relative velocity distributions on E_{off} (see section 3.2.2 for more details). With this we have now everything in place to calculate the theoretical loss rate $k_{\text{th}} = k_{\text{dd}} + k_{\text{lv}} + k_{\text{el}}$ with contributions from dipolar relaxation, langevin loss rate and elastic collisional loss as a function of E_{off}. The result is depicted in black in Figure 3.17, where the by far dominating contribution to k_{th} is dipolar relaxation, that is also the only of the three contributing loss mechanisms showing a direct electric field dependence.

Impact of inelastic collisional loss in the guide and in the trap

We started the collision section 3.2 with a brief review of the collision measurements performed with the Cryofuge in 2017, where we investigated two-body losses from a quadrupole guide for CH_3F and ND_3 [78]. In section 3.2.6 we already compared the impact of elastic losses for the collision studies in the guide and in the trap. In the following we will now repeat this for the contribution of inelastic losses for the two measurements. According to Equation 3.36 the Langevin loss-rate is a function of the relative velocity v_{rel} and the dipole moment d_{avg} averaged over the populated rotational $|J, K, M\rangle$ states. In 2017 the averaged dipole moment was determined as $d_{\text{avg}} = 0.56\text{D}$ [78], whereas now we obtain a value of $d_{\text{avg}} = 0.83\text{D}$, utilising the state distribution measurements, presented in section 3.2.3. The averaged dipole moment is larger for the measurements shown in this thesis due to a improved state purity resulting from a colder buffergas cell. We determine the relative velocity distribution of the molecules in the trap, as illustrated in section 3.2.2, and can exemplary look at the A+B measurement sequence with $t_{\text{load}} = 0.5\text{s}$ and an offset field of $E_{\text{off}} = 0.50\text{kV/cm}$, where we obtain a mean relative velocity of $\bar{v}_{\text{rel}} = 19.3\text{m/s}$. This value is significantly lower than $\bar{v}_{\text{rel}} = 28.2\text{m/s}$ measured by Wu et. al. in 2017 [177], since in contrast to the three dimensional confinement in the trap, molecules in the guide are only confined transversely but can move freely in the longitudinal direction. Taking into account that for the collision measurements in the trap $\bar{v}_{\text{rel}}$ is lower and d_{avg} is larger than for the measurements in the guide we expect a larger Langevin

loss-rate for the collisions in the trap. Indeed we obtain a two-body loss rate of $k_{\mathrm{lv,trap}} = 6.67 \cdot 10^{-10}\mathrm{cm}^3\mathrm{s}^{-1}$ for collision in the trap and $k_{\mathrm{lv,guide}} = 4.23 \cdot 10^{-10}\mathrm{cm}^3\mathrm{s}^{-1}$ for inelastic two-body losses in the guide. According Equation 3.36 and the presented values for $\bar{v}_{\mathrm{rel}}$ and d_{avg} one would expect $k_{\mathrm{lv,guide}}/k_{\mathrm{lv,trap}} \approx 0.5$, however we obtain a ratio of 0.6, due to the fact that we calculate the Langevin loss-rate by averaging over the measured relative velocity distribution instead of using $\bar{v}_{\mathrm{rel}}$.

In addition to the Langevin loss-rate we can also consider the impact of dipolar relaxation for the two collision experiments. For the measurements in the trap we identified dipolar relaxation as the by far dominant collisional loss mechanism which we suppressed by a factor of two by increasing an external electric field from $E_{\mathrm{off}} = 0.50\mathrm{kV/cm}$ to $E_{\mathrm{off}} = 2.37\mathrm{kV/cm}$. In the following we will take a look at the impact of dipolar relaxation for the collision measurements in the guide. Here there are two important aspects we need to consider; the average electric field in the guide is with $E_{\mathrm{guide}} = 45\mathrm{kV/cm}$ significantly larger than in the trap and due to the warmer buffergas cell temperature the fraction of molecules in $|2,1\rangle$ has increased and more rotational states are populated [78]. As a consequence the calculations presented in section 3.2.6 are no longer feasible for all populated rotational states within reasonable calculation time, such that we perform the calculations only for a pair of molecules with a relative velocity of $v_{\mathrm{rel}} = 28.2\mathrm{m/s}$ within the (1,1)-manifold at an electric field of $E_{\mathrm{guide}} = 45\mathrm{kV/cm}$. According to the results presented in section 3.2.6, this should give an upper bound for the two-body loss rate k_{dd}, caused by dipolar relaxation, which we calculate as $k_{\mathrm{dd}} = \sigma_{\mathrm{loss}} \cdot v_{\mathrm{rel}} = 8.83 \cdot 10^{-10}\mathrm{cm}^3\mathrm{s}^{-1}$. This value is significantly lower than the one's obtained for collisions in the trap (see Figure 3.17) and comparable to the calculated Langevin loss-rate $k_{\mathrm{lv,guide}}$ in the guide. Thus the assumption made in the Science paper in 2017 [78], that all inelastic collisional losses are covered by the Langevin capture model is reasonable due to the large external electric field in the guide. However as mentioned in the publication by Wu et al. [78], the theoritcally calculated loss-rate was 40% to 60% lower than the experimentally determined value for k, which Wu et. al. attributed to imprecision in the density calibration or imperfections of the Langevin model. With the calculations performed in this section it seems reasonable that neglecting the contribution of dipolar relaxation explains the difference between experiment and theory.

Chapter 4

Outlook

This thesis covered two distinct topics, where in the first part we proposed how to utilise opto-electric or opto-magnetic Sisyphus cooling to extend molecule research in the cold and ultracold temperature regime to more diverse species. Here we found that molecules with closely spaced opposite parity levels in the ground state, like symmetric top molecules, diatomic radicals with Λ- or Ω-doubling or linear polyatomic molecules excited to a vibrational bending mode, are in particular promising candidates. In the second part of this thesis we demonstrated the observation of electric field controlled dipolar collisions between cold, trapped CH_3F molecules. By tuning an external electric field we were able to suppress collision induced two-body loss from the trap by a factor of two. In addition we identified the loss, using a semi-classical model, to be predominantly caused by dipolar relaxation, a state changing collision process. The demonstrated suppression of inelastic two-body loss without affecting energy exchanging elastic collisions can be an important ingredient to measure rethermalisation and potentially observe evaporative cooling with polyatomic symmetric top molecules.

Cold and ultracold dipolar collisions

The observation of a quantum degenerate gas of naturally occurring polar molecules is a long time outstanding goal in the field of cold and ultracold molecules. Due to the rapid progress in recent years both laser cooling, as well as opto-electric Sisyphus cooling allow molecules to be directly cooled to ultracold temperatures [120, 109, 118, 21]. However, to observe a Bose–Einstein condensate, the particles typically have to be cooled to quantum degeneracy by means of evaporative cooling techniques [4, 5], relying on efficient rethermalisation of the molecular sample via energy exchanging elastic collisions. For rethermalisation to be efficient a key requirement is the suppression of inelastic collisions, leading to loss, without affecting thermalising elastic collisions [194], as demonstrated in this thesis. This in combination with the high density samples of trapped molecules renders our experiment a good starting point to investigate rethermalisation. Thereto we have to cut into

the energy distribution of the trapped ensemble using a radio-frequency knife [21] removing molecules above a given energy, such that thermalising elastic collisions can repopulate these energy classes. For our experiment we estimate the maximum achievable density after applying a radio-frequency knife at 7GHz·h, averaged over the trapping time, to be $n = 1.0 \cdot 10^7 \mathrm{cm}^{-3}$. In combination with a relative velocity of $v_{\mathrm{rel}} = 14\mathrm{m/s}$ and an elastic collision cross-section of $\sigma_{\mathrm{el}} = 7.81 \cdot 10^{-12}\mathrm{cm}^2$ this results in an elastic collision frequency of about 0.11Hz. In addition we have to consider that the eikonal approximation [178] strongly favors forward scattering such that the energy transfer in an elastic collision process is typically small and that our trap lifetime is finite with a 1/e trap decay time of 1s. Taking all these aspects into account we utilise a Monte-Carlo type simulation to estimate that about 0.35% of the molecules repopulate energy classes above the cutoff frequency (here 7GHz). Therefore, with the current experimental setup, it will be very challenging to measure rethermalisation, without further cooling or a larger density of trapped molecules. However, opto-electric Sisyphus cooling has already been demonstrated for CH_3F in our group, reaching temperatures of about 30mK [27]. This can improve the 1/e trap decay time of up to a factor of 60 [21] so that after applying opto-electric Sisyphus cooling the observation of rethermalisation should be possible.

Cooling the molecular samples does not only help to measure rethermalisation but also opens up more exciting research avenues. For example in the field of cold chemistry the observation of energy dependent collision resonances [195] and control over the reaction processes [68] becomes feasible. At even lower temperatures, in the quantum limit, interaction lengths on the order of 1μm [113] can be obtained for polar molecules opening research opportunities like the investigation of dipole-blockaded [196, 197] or strongly correlated system [198, 199].

Opto-electric Sisyphus cooling of radical molecules with the cryofuge

In 2016 Prehn et al. prepared an ensemble of $3 \cdot 10^5$ H_2CO molecules at a temperature of about 420μK using opto-electric Sisyphus cooling [21], which is the to date largest number of of molecules directly cooled to ultracold temperatures. However, the comparably slow spontaneous decay ($\sim$ 100Hz) of the vibrational excited state and the resulting trap losses during cooling, limited the preparation of an even larger ensemble of ultracold molecules. This renders molecular radicals in particular interesting for opto-electric or opto-magnetic Sisyphus cooling due to the possibility to use an electronic excited state with decay rates on the order of MHz. The generality of our experimental setup makes it the ideal platform to extend opto-electric Sisyphus cooling to molecular radicals like CH or YbOH. Both of these molecules are hard to laser cool and therefore have not yet been laser cooled in all three-dimensions. However, they are ideal candidates for opto-electric Sisyphus cooling as they possess closely spaced opposite parity states in their ground state due to Λ- or Ω-doubling in CH and a degenerate vibrational bending mode in YbOH. Consequently, these molecules show a a strong electric field response, that allows efficient

centrifuge deceleration and trapping, but the molecular source in our experiment would have to be modified as radicals no longer arrive in gas bottle but have to be produced e.g. by laser ablation [89]. However, the production of radical molecules is well studied and routinely achieved by various research groups [94, 106, 107], such that production, deceleration and trapping of these molecular radicals should be straightforward to implement with the Cryofuge setup. Beyond good cooling properties, like the large spontaneous decay rate, CH and YbOH possess inversion doublets that provide additional fascinating research opportunities for fundamental physics tests. The Λ-doublet transitions in the ground state of CH are very sensitive to probe variations in the finestructure constant α or the electron-to-proton mass ratio μ [158]. The linear triatomic radical YbOH, is also particularly interesting for fundamental physics tests as it is proposed to enable measurements that surpass the current limit of $|d_e| < 1.1 \cdot 10^{-29}$e·cm for the dipole moment of the electron [127]. For all of these envisioned experiments opto-electric Sisyphus cooling or cooling in general is particularly relevant, as it increases the interrogation times and improves statistics.

Bibliography

[1] T.W. Hänsch and A.L. Schawlow. Cooling of Gases by Laser Radiation. *Optics Communications*, 13(1):68 (2), 1975.

[2] V.I. Balykin, V.S. Letokhov, and V.G. Minogin. Cooling atoms by means of laser radiation pressure. *Soviet Physics Uspekhi*, 28:803 (24), 1985.

[3] W.D. Phillips, J.V. Prodan, and H.J. Metcalf. Laser cooling and electromagnetic trapping of neutral atoms. *Journal of the Optical Society of America B*, 2(11):1751 (7), 1985.

[4] M.H. Anderson, J.R. Ensher, M.R. Matthews, C.E. Wieman, and E.A. Cornell. Observation of bose-einstein condensation in a dilute atomic vapor. *Science*, 269(5221):198 (4), 1995.

[5] K.B. Davis, M.-O. Mewes, M.R. Andrews, N.J. Van Druten, D.S. Durfee, D.M. Kurn, and W. Ketterle. Bose-Einstein condensation in a gas of sodium atoms. *Physical Review Letters*, 75(22):3969 (5), 1995.

[6] B.B. Blinov, D.L. Moehring, L.-M. Duan, and C. Monroe. Observation of entanglement between a single trapped atom and a single photon. *Nature*, 428(3):153 (4), 2004.

[7] A. Reiserer, N. Kalb, G. Rempe, and S. Ritter. A quantum gate between a flying optical photon and a single trapped atom. *Nature*, 508(4):237 (4), 2014.

[8] M. Greiner, O. Mandel, T. Esslinger, T.W. Hänsch, and I. Bloch. Quantum phase transition from a superfluid to a Mott insulator in an ultracold gas of atoms. *Nature*, 415(1):39 (6), 2003.

[9] I. Bloch, J. Dalibard, and W. Zwerger. Many-body physics with ultracold gases. *Reviews of Modern Physics*, 80(3):885 (80), 2008.

[10] T. Udem, R. Holzwarth, and T.W. Hänsch. Optical frequency metrology. *Nature*, 416(3):233 (5), 2002.

[11] M. Takamoto, F.-L. Hong, R. Higashi, and H. Katori. An optical lattice clock. *Nature*, 435(5):321 (4), 2005.

[12] C.H. Townes and A.L. Schawlow. *Microwave Spectroscopy*. Dover Publicatios, Inc., 1975.

[13] J.M. Brown and A. Carrington. *Rotational Spectroscopy of Diatomic Molecules*. 1st edition, 2003.

[14] D. DeMille. Quantum Computation with Trapped Polar Molecules. *Physical Review Letters*, 88(6):067901 (4), 2002.

[15] R. V. Krems. Cold controlled chemistry. *Physical Chemistry Chemical Physics*, 10(28):4079 (14), 2008.

[16] T. Lahaye, C. Menotti, L. Santos, M. Lewenstein, and T. Pfau. The physics of dipolar bosonic quantum gases. *Reports on Progress in Physics*, 72(12):126401 (41), 2009.

[17] E. Altman, K.R. Brown, G. Carleo, L.D. Carr, E. Demler, C. Chin, B. DeMarco, S.E. Economou, M.A. Eriksson, K.-M.C. Fu, M. Greiner, K.R.A. Hazzard, R.G. Hulet, A.J. Kollár, B.L. Lev, M.D. Lukin, R. Ma, X. Mi, S. Misra, C. Monroe, K. Murch, Z. Nazario, K.-K. Ni, A.C. Potter, P. Roushan, M. Saffman, M. Schleier-Smith, I. Siddiqi, R. Simmonds, M. Singh, I.B. Spielman, K. Temme, D.S. Weiss, J. Vučković, V. Vuletić, J. Ye, and M.W. Zwierlein. Quantum Simulators: Architectures and Opportunities. *PRX Quantum*, 2(1):017003 (19), 2021.

[18] E.B. Norrgard, D.J. McCarron, M.H. Steinecker, M.R. Tarbutt, and D. DeMille. Submillikelvin Dipolar Molecules in a Radio-Frequency Magneto-Optical Trap. *Physical Review Letters*, 116(6):063004 (6), 2016.

[19] L. Anderegg, B.L. Augenbraun, Y. Bao, S. Burchesky, L.W. Cheuk, W. Ketterle, and J.M. Doyle. Laser cooling of optically trapped molecules. *Nature Physics*, 14(9):890 (4), 2018.

[20] L. Caldwell, J.A. Devlin, H.J. Williams, N.J. Fitch, E.A. Hinds, B.E. Sauer, and M.R. Tarbutt. Deep Laser Cooling and Efficient Magnetic Compression of Molecules. *Physical Review Letters*, 123(3):033202 (6), 2019.

[21] A. Prehn, M. Ibrügger, R. Glöckner, G. Rempe, and M. Zeppenfeld. Optoelectrical Cooling of Polar Molecules to Submillikelvin Temperatures. *Physical Review Letters*, 116(6):063005 (6), 2016.

[22] M.D. Di Rosa. Laser-cooling molecules: Concept, candidates, and supporting hyperfine-resolved measurements of rotational lines in the A-X(0,0) band of CaH. *European Physical Journal D*, 31(2):395 (8), 2004.

[23] T.A. Isaev and R. Berger. Polyatomic Candidates for Cooling of Molecules with Lasers from Simple Theoretical Concepts. *Physical Review Letters*, 116(6):063006 (5), 2016.

[24] I. Kozyryev, L. Baum, K. Matsuda, and J.M. Doyle. Proposal for Laser Cooling of Complex Polyatomic Molecules. *ChemPhysChem*, 17(22):3641 (8), 2016.

[25] C.E. Dickerson, H. Guo, A.J. Shin, B.L. Augenbraun, J.R. Caram, W.C. Campbell, and A.N. Alexandrova. Franck-Condon Tuning of Optical Cycling Centers by Organic Functionalization. *Physical Review Letters*, 126(12):123002 (6), 2021.

[26] M. Zeppenfeld, M. Motsch, P.W.H. Pinkse, and G. Rempe. Optoelectrical cooling of polar molecules. *Physical Review A*, 80(4):041401 (4), 2009.

[27] M. Zeppenfeld, B.G.U. Englert, R. Glöckner, A. Prehn, M. Mielenz, C. Sommer, L.D. van Buuren, M. Motsch, and G. Rempe. Sisyphus cooling of electrically trapped polyatomic molecules. *Nature*, 491(11):570 (4), 2012.

[28] L.W. Cheuk, L. Anderegg, Y. Bao, S. Burchesky, S.S. Yu, W. Ketterle, K.-K. Ni, and J.M. Doyle. Observation of Collisions between Two Ultracold Ground-State CaF Molecules. *Physical Review Letters*, 125(4):43401 (6), 2020.

[29] L. Anderegg, S. Burchesky, Y. Bao, S.S. Yu, T. Karman, and E. Chae. Observation of microwave shielding of ultracold molecules. *Science*, 373(6556):779 (4), 2021.

[30] H.J. Williams, L. Caldwell, N.J. Fitch, S. Truppe, J. Rodewald, E.A. Hinds, B.E. Sauer, and M.R. Tarbutt. Magnetic Trapping and Coherent Control of Laser-Cooled Molecules. *Physical Review Letters*, 120(16):163201 (6), 2018.

[31] S. Burchesky, L. Anderegg, Y. Bao, S.S. Yu, E. Chae, W. Ketterle, K.-K. Ni, and J.M. Doyle. Rotational Coherence Times of Polar Molecules in Optical Tweezers. *Physical Review Letters*, 127(12):123202 (5), 2021.

[32] D. DeMille. Diatomic molecules, a window onto fundamental physics. *Physics Today*, 68(12):34 (7), 2015.

[33] T.E. Wall. Preparation of cold molecules for high-precision measurements. *Journal of Physics B: Atomic, Molecular and Optical Physics*, 49(24):243001 (37), 2016.

[34] M.S. Safronova, D. Budker, D. DeMille, D.F.J. Kimball, A. Derevianko, and C.W. Clark. Search for new physics with atoms and molecules. *Reviews of Modern Physics*, 90(2):025008 (106), 2018.

[35] J. Bagdonaite, P. Jansen, C. Henkel, H.L. Bethlem, K.M. Menten, and W. Ubachs. A Stringent Limit on a Drifting Proton-to-Electron Mass Ratio from Alcohol in the Early Universe. *Science*, 339(6115):46 (3), 2013.

[36] S. Truppe, R.J. Hendricks, S.K. Tokunaga, H.J. Lewandowski, M.G. Kozlov, C. Henkel, E.A. Hinds, and M.R. Tarbutt. A search for varying fundamental constants using hertz-level frequency measurements of cold CH molecules. *Nature Communications*, 4(9):1 (7), 2013.

[37] K. Zioutas and Y. Semertzidis. A NEW DETECTOR SCHEME FOR AXIONS. *Physics Letters A*, 130(2):94 (4), 1988.

[38] A. Arvanitaki, S. Dimopoulos, and K. Van Tilburg. Resonant Absorption of Bosonic Dark Matter in Molecules. *Physical Review X*, 8(4):041001 (43), 2018.

[39] L.D. Carr, D. DeMille, R.V. Krems, and J. Ye. Cold and ultracold molecules: Science, technology and applications. *New Journal of Physics*, 11(5):055049 (87), 2009.

[40] N.R. Hutzler. A New Limit on the Electron Electric Dipole Moment: Beam Production, Data Interpretation, and Systematics. *Phd thesis, Harvard University, Cambridge MA, USA*, (February):311, 2014.

[41] I.M. Rabey. Improved shot noise limit of the YbF EDM experiment. *Phd thesis, Imperial College London*, November:134, 2016.

[42] V. Andreev, D.G. Ang, D. DeMille, J.M. Doyle, G. Gabrielse, J. Haefner, N.R. Hutzler, Z. Lasner, C. Meisenhelder, B.R. O'Leary, C.D. Panda, A.D. West, E.P. West, and X. Wu. Improved limit on the electric dipole moment of the electron. *Nature*, 562(10):355 (6), 2018.

[43] J. Baron, W.C. Campbell, D. DeMille, J.M. Doyle, G. Gabrielse, Y.V. Gurevich, P.W. Hess, N.R. Hutzler, E. Kirilov, I. Kozyryev, B.R. O'Leary, C.D. Panda, M.F. Parsons, E.S. Petrik, B. Spaun, A.C. Vutha, and A.D. West. Order of Magnitude Smaller Limit on the Electric Dipole Moment of the Electron. *Science*, 343(6168):269 (4), 2014.

[44] J. Baron, W.C. Campbell, D. DeMille, J.M. Doyle, G. Gabrielse, Y.V. Gurevich, P.W. Hess, N.R. Hutzler, E. Kirilov, I. Kozyryev, B.R. O'Leary, C.D. Panda, M.F. Parsons, B. Spaun, A.C. Vutha, A.D. West, and E.P. West. Methods, analysis, and the treatment of systematic errors for the electron electric dipole moment search in thorium monoxide. *New Journal of Physics*, 19(7):073029 (67), 2017.

[45] L.V. Skripnikov, A.N. Petrov, and A.V. Titov. Communication: Theoretical study of ThO for the electron electric dipole moment search. *Journal of Chemical Physics*, 139(22):221103 (4), 2013.

[46] D. DeMille, F. Bay, S. Bickman, D. Kawall, D. Krause, S.E. Maxwell, and L.R. Hunter. Investigation of PbO as a system for measuring the electric dipole moment of the electron. *Physical Review A*, 61(5):052507 (8), 2000.

[47] X. Wu, Z. Han, J. Chow, D.G. Ang, C. Meisenhelder, C.D. Panda, E.P. West, G. Gabrielse, J.M. Doyle, and D. DeMille. The metastable $Q^3\Delta_2$ state of ThO : a new resource for the ACME electron EDM search. *New Journal of Physics*, 22(2):023013 (16), 2020.

[48] X. Alauze, J. Lim, M.A. Trigatzis, S. Swarbrick, F.J. Collings, N.J. Fitch, B.E. Sauer, and M.R. Tarbutt. An ultracold molecular beam for testing fundamental physics. *Quantum Science Technology*, 6(4):044005 (17), 2021.

[49] J.I. Cirac, P. Zoller, H.J. Kimble, and H. Mabuchi. Quantum State Transfer and Entanglement Distribution among Distant Nodes in a Quantum Network. *Physical Review Letters*, 78(16):3221 (4), 1997.

[50] L.-M. Duan, M.D. Lukin, J.I. Cirac, and P. Zoller. Long-distance quantum communication with atomic ensembles and linear optics. *Nature*, 414(11):413 (6), 2001.

[51] A. Reiserer and G. Rempe. Cavity-based quantum networks with single atoms and optical photons. *Reviews of Modern Physics*, 87(4):1379 (40), 2015.

[52] C. P. Koch, M. Lemeshko, and D. Sugny. Quantum control of molecular rotation. *Reviews of Modern Physics*, 91(3):035005 (37), 2019.

[53] J.W. Park, Z.Z. Yan, H. Loh, S.A. Will, and M.W. Zwierlein. Second-scale nuclear spin coherence time of ultracold $^{23}Na^{40}K$ molecules. *Science*, 357(6349):372 (4), 2017.

[54] A. André, D. DeMille, J.M. Doyle, M.D. Lukin, S.E. Maxwell, P. Rabl, R.J. Schoelkopf, and P. Zoller. A coherent all-electrical interface between polar molecules and mesoscopic superconducting resonators. *Nature Physics*, 2(9):636 (7), 2006.

[55] P. Rabl, D. DeMille, J.M. Doyle, M.D. Lukin, R.J. Schoelkopf, and P. Zoller. Hybrid Quantum Processors : Molecular Ensembles as Quantum Memory for Solid State Circuits. *Physical Review Letters*, 97(3):033003 (4), 2006.

[56] P. Rabl and P. Zoller. Molecular dipolar crystals as high-fidelity quantum memory for hybrid quantum computing. *Physical Review A*, 76(4):042308 (23), 2007.

[57] Q. Wei, S. Kais, B. Friedrich, and D. Herschbach. Entanglement of polar symmetric top molecules as candidate qubits. *The Journal of Chemical Physics*, 135(15):154102 (10), 2011.

[58] D. Herrschbach. Molecular collisions, from warm to ultracold. *Faraday Discussions*, 142:9 (15), 2009.

[59] S.Y.T. van de Meerakker and G. Meijer. Collision experiments with Stark-decelerated beams. *Faraday Discussions*, 142:113 (14), 2009.

[60] S. Chefdeville, Y. Kalugina, S.Y.T. van de Meerakker, C. Naulin, F. Lique, and M. Costes. Observation of Partial Wave Resonances in Low-Energy O_2 - H_2 Inelastic Collisions. *Science*, 341(6150):1094 (4), 2013.

[61] J.D. Weinstein, R. DeCarvalho, T. Guillet, B. Friedrich, and J.M. Doyle. Magnetic trapping of calcium monohydride molecules at millikelvin temperatures. *Nature*, 395(9):148 (3), 1998.

[62] Y. Segev, M. Pitzer, M. Karpov, N. Akerman, J. Narevicius, and E. Narevicius. Collisions between cold molecules in a superconducting magnetic trap. *Nature*, 572(8):189 (5), 2019.

[63] S.Y.T. van de Meerakker, P.H.M. Smeets, N. Vanhaecke, R.T. Jongma, and G. Meijer. Deceleration and Electrostatic Trapping of OH Radicals. *Physical Review Letters*, 94(2):023004 (4), 2005.

[64] M. Kirste, B.G. Sartakov, M. Schnell, and G. Meijer. Nonadiabatic transitions in electrostatically trapped ammonia molecules. *Physical Review A*, 79(5):051401 (4), 2009.

[65] B.G.U. Englert, M. Mielenz, C. Sommer, J. Bayerl, M. Motsch, P.W.H. Pinkse, G. Rempe, and M. Zeppenfeld. Storage and adiabatic cooling of polar molecules in a microstructured trap. *Physical Review Letters*, 107(26):263003 (4), 2011.

[66] O. Dulieu, R. Krems, M. Weidemüller, and S. Willitsch. Physics and Chemistry of Cold Molecules. *Physical Chemistry Chemical Physics*, 13(42):18703 (2), 2011.

[67] J.M. Doyle, B. Friedrich, and E. Narevicius. Physics and Chemistry with Cold Molecules. *ChemPhysChem*, 17(22):3581 (2), 2016.

[68] J.L. Bohn, A.M. Rey, and J. Ye. Cold molecules: Progress in quantum engineering of chemistry and quantum matter. *Science*, 357(6355):1002 (9), 2017.

[69] K.-K. Ni, S. Ospelkaus, D. Wang, G. Quemener, B. Neyenhuis, M.H.G. de Miranda, J.L. Bohn, J. Ye, and D.S. Jin. Dipolar collisions of polar molecules in the quantum regime. *Nature*, 464(4):1324 (5), 2010.

[70] Y. Liu, M.-G. Hu, M.A. Nichols, D.D. Grimes, T. Karman, H. Guo, and K.-K. Ni. Photo-excitation of long-lived transient intermediates in ultracold reactions. *Nature Physics*, 16(9):1132 (5), 2020.

[71] P.D. Gregory, M.D. Frye, J.A. Blackmore, E.M. Bridge, R. Sawant, J.M. Hutson, and S.L. Cornish. Sticky collisions of ultracold RbCs molecules. *Nature Communications*, 10(1):3104 (7), 2019.

[72] X. Ye, M. Guo, M.L. González-Martínez, G. Quéméner, and D. Wang. Collisions of ultracold ^{2}3Na ^{8}7Rb molecules with controlled chemical reactivities. *Science Advances*, 4(1):1 (6), 2018.

[73] J. Kłos, Q. Guan, H. Li, M. Li, E. Tiesinga, and S. Kotochigova. Roaming pathways and survival probability in real-time collisional dynamics of cold and controlled bialkali molecules. *Scientific Reports*, 11:10598 (11), 2021.

[74] G. Valtolina, K. Matsuda, W.G. Tobias, J.-R. Li, L. De Marco, and J. Ye. Dipolar evaporation of reactive molecules to below the Fermi temperature. *Nature*, 588(10):239 (5), 2020.

[75] L. De Marco, G. Valtolina, K. Matsuda, W.G. Tobias, J.P. Covey, and J. Ye. A degenerate Fermi gas of polar molecules. *Science*, 363(6429):853 (4), 2019.

[76] B.C. Sawyer, B.K. Stuhl, M. Yeo, T.V. Tscherbul, M.T. Hummon, Y. Xia, K. Jacek, D. Patterson, J.M. Doyle, and J. Ye. Cold heteromolecular dipolar collisions. *Physical Chemistry Chemical Physics*, 13(42):19059 (67), 2011.

[77] S. Jurgilas, A. Chakraborty, C.J.H. Rich, L. Caldwell, H.J. Williams, N.J. Fitch, B.E. Sauer, M.D. Frye, J.M. Hutson, and M.R. Tarbutt. Collisions between Ultracold Molecules and Atoms in a Magnetic Trap. *Physical Review Letters*, 126(15):153401 (6), 2021.

[78] X. Wu, T. Gantner, M. Koller, M. Zeppenfeld, S. Chervenkov, and G. Rempe. A cryofuge for cold-collision experiments with slow polar molecules. *Science*, 358(6363):645 (4), 2017.

[79] K. Ni, S. Ospelkaus, M.H.G. de Miranda, A. Pe'er, B. Neyenhuis, J.J. Zirbel, S. Kotochigova, P.S. Julienne, D.S. Jin, and J. Ye. A High Phase-Space-Density Gas of Polar Molecules. *Science*, 322(5899):231 (6), 2008.

[80] K. Aikawa, D. Akamatsu, M. Hayashi, K. Oasa, J. Kobayashi, P. Naidon, T. Kishimoto, M. Ueda, and S. Inouye. Coherent Transfer of Photoassociated Molecules into the Rovibrational Ground State. *Physical Review Letters*, 105(20):203001 (4), 2010.

[81] P.K. Molony, P.D. Gregory, Z. Ji, B. Lu, M.P. Köppinger, C.R.L. Sueur, C.L. Blackley, J.M. Hutson, and S.L. Cornish. Creation of Ultracold ^{87}Rb^{133}Cs Molecules in the Rovibrational Ground State. *Physical Review Letters*, 113(25):255301 (5), 2014.

[82] J.W. Park, S.A. Will, and M.W. Zwierlein. Ultracold Dipolar Gas of Fermionic $^{23}Na^{40}K$ Molecules in Their Absolute Ground State. *Physical Review Letters*, 114(20):205302 (5), 2015.

[83] F. Seeßelberg, N. Buchheim, Z-K. Lu, T. Schneider, X.-Y. Luo, E. Tiemann, I. Bloch, and C. Gohle. Modeling the adiabatic creation of ultracold polar $^{23}Na^{40}K$ molecules. *Physical Review A*, 97(1):013405 (7), 2018.

[84] J. Ulmanis, J. Deiglmayr, M. Repp, R. Wester, and M. Weidemüller. Ultracold Molecules Formed by Photoassociation : Heteronuclear Dimers , Inelastic Collisions , and Interactions with Ultrashort Laser Pulses. *Chemical Reviews*, 112(9):4890 (33), 2012.

[85] A. Fioretti, D. Comparat, A. Crubellier, O. Dulieu, and P. Pillet. Formation of Cold Cs_2 Molecules through Photoassociation. *Physical Review Letters*, 80(20):4402 (4), 1998.

[86] J.M. Sage, S. Sainis, T. Bergeman, and D. DeMille. Optical Production of Ultracold Polar Molecules. *Physical Review Letters*, 94(20):203001 (4), 2005.

[87] J. Deiglmayr, A. Grochola, M. Repp, K. Mörtlbauer, C. Glück, J. Lange, O. Dulieu, R. Wester, and M. Weidemüller. Formation of Ultracold Polar Molecules in the Rovibrational Ground State. *Physical Review Letters*, 101(13):133004 (4), 2008.

[88] K. Ni, S. Ospelkaus, D.J. Nesbitt, J. Ye, and D.S. Jin. A dipolar gas of ultracold molecules. *Physical Chemistry Chemical Physics*, 11(42):9626 (14), 2009.

[89] S.E. Maxwell, N. Brahms, R. DeCarvalho, D.R. Glenn, J.S. Helton, S.V. Nguyen, D. Patterson, J. Petricka, D. DeMille, and J.M. Doyle. High-Flux Beam Source for Cold, Slow Atoms or Molecules. *Physical Review Letters*, 95(17):173201 (4), 2005.

[90] L.D. van Buuren, C. Sommer, M. Motsch, S. Pohle, M. Schenk, J. Bayerl, P.W.H. Pinkse, and G. Rempe. Electrostatic extraction of cold molecules from a cryogenic reservoir. *Physical Review Letters*, 102(3):033001 (4), 2009.

[91] D. Patterson and J.M. Doyle. Cooling molecules in a cell for FTMW spectroscopy. *Molecular Physics*, 110(15-16):1757 (10), 2012.

[92] C. Sommer, L.D. van Buuren, M. Motsch, S. Pohle, J. Bayerl, P.W.H. Pinkse, and G. Rempe. Continuous guided beams of slow and internally cold polar molecules. *Faraday Discussions*, 142:203 (18), 2009.

[93] X. Wu, T. Gantner, M. Zeppenfeld, S. Chervenkov, and G. Rempe. Thermometry of Guided Molecular Beams from a Cryogenic Buffer-Gas Cell. *ChemPhysChem*, 17(22):3631 (10), 2016.

[94] V. Zhelyazkova, A. Cournol, T.E. Wall, A. Matsushima, J.J. Hudson, E.A. Hinds, M.R. Tarbutt, and B.E. Sauer. Laser cooling and slowing of CaF molecules. *Physical Review A*, 89(5):053416 (5), 2014.

[95] D. Egorov, W.C. Campbell, B. Friedrich, S.E. Maxwell, E. Tsikata, L.D. van Buuren, and J.M. Doyle. Buffer-gas cooling of NH via the beam loaded buffer-gas method. *The European Physical Journal D*, 31:307 (5), 2004.

[96] N.R. Hutzler, H.-I. Lu, and J.M. Doyle. The Buffer Gas Beam: An Intense, Cold, and Slow Source for Atoms and Molecules. *Chemical Reviews*, 112(9):4803 (22), 2012.

[97] H.L. Bethlem, G. Berden, and G. Meijer. Decelerating Neutral Dipolar Molecules. *Physical Review Letters*, 83(8):1558 (4), 1999.

[98] A. Osterwalder, S.A. Meek, G. Hammer, H. Haak, and G. Meijer. Deceleration of neutral molecules in macroscopic traveling traps. *Physical Review A*, 81(5):051401 (4), 2010.

[99] H.L. Bethlem, G. Berden, F.M.H. Crompvoets, R.T. Jongma, A.J.A. van Roij, and G. Meijer. Electrostatic trapping of ammonia molecules. *Nature*, 406(8):491 (4), 2000.

[100] C. Meng, A.P.P. van der Poel, C. Cheng, and H.L. Bethlem. Femtosecond laser detection of Stark-decelerated and trapped methylfluoride molecules. *Physical Review A*, 92(2):023404 (4), 2015.

[101] E. Narevicius and M.G. Raizen. Toward Cold Chemistry with Magnetically Decelerated Supersonic Beams. *Chemical Reviews*, 112(9):4879 (11), 2012.

[102] Y. Liu, M. Vashishta, P. Djuricanin, S. Zhou, W. Zhong, T. Mittertreiner, D. Carty, and T. Momose. Magnetic Trapping of Cold Methyl Radicals. *Physical Review Letters*, 118(9):093201 (5), 2017.

[103] N. Akerman, M. Karpov, Y. Segev, N. Bibelnik, J. Narevicius, and E. Narevicius. Trapping of Molecular Oxygen together with Lithium Atoms. *Physical Review Letters*, 119(7):073204 (5), 2017.

[104] S.D. Hogan, M. Motsch, and F. Merkt. Deceleration of supersonic beams using inhomogeneous electric and magnetic fields. *Physical Chemistry Chemical Physics*, 13(42):18705 (19), 2011.

[105] S.Y.T. van de Meerakker, H.L. Bethlem, N. Vanhaecke, and G. Meijer. Manipulation and Control of Molecular Beams. *Chemical Reviews*, 112(9):4828 (51), 2012.

[106] M. Yeo, M.T. Hummon, A.L. Collopy, B. Yan, B. Hemmerling, E. Chae, J.M. Doyle, and J. Ye. Rotational State Microwave Mixing for Laser Cooling of Complex Diatomic Molecules. *Physical Review Letters*, 114(22):223003 (5), 2015.

[107] J.F. Barry, E.S. Shuman, E.B. Norrgard, and D. DeMille. Laser Radiation Pressure Slowing of a Molecular Beam. *Physical Review Letters*, 108(10):103002 (5), 2012.

[108] J.F. Barry, D.J. McCarron, E.B. Norrgard, M.H. Steinecker, and D. DeMille. Magneto-optical trapping of a diatomic molecule. *Nature*, 512(8):286 (4), 2014.

[109] S. Truppe, H.J. Williams, N.J. Fitch, M. Hambach, T.E. Wall, E.A. Hinds, B.E. Sauer, and M.R. Tarbutt. An intense, cold, velocity-controlled molecular beam by frequency-chirped laser slowing. *New Journal of Physics*, 19(2):022001 (13), 2017.

[110] N.J. Fitch and M.R. Tarbutt. Principles and Design of a Zeeman - Sisyphus Decelerator for Molecular Beams. *ChemPhysChem*, 17(22):3609 (15), 2016.

[111] B.L. Augenbraun, A. Frenett, H. Sawaoka, C. Hallas, N.B. Vilas, A. Nasir, Z.D. Lasner, and J.M. Doyle. Zeeman-Sisyphus Deceleration of Molecular Beams. *arXiv:*, 2109.03067:6, 2021.

[112] S. Chervenkov, X. Wu, J. Bayerl, A. Rohlfes, T. Gantner, M. Zeppenfeld, and G. Rempe. Continuous Centrifuge Decelerator for Polar Molecules. *Physical Review Letters*, 112(1):013001 (5), 2014.

[113] X. Wu. A Centrifuge Decelerator and a Thermometer for Cold Polar Molecules. *Phd thesis, Technische Universität München, Garching bei München, Germany*, (March):106, 2017.

[114] T. Gantner. Cold , Dense , and Slow Samples of Polyatomic Molecules for Collision Experiments. *Phd thesis, Technische Universität München, Garching bei München, Germany*, (May):106, 2019.

[115] D. Comparat. Molecular cooling via Sisyphus processes. *Physical Review A*, 89(4):043410 (20), 2014.

[116] F. Robicheaux. A proposal for laser cooling of OH molecules. *Journal of Physics B: Atomic, Molecular and Optical Physics*, 42(19):195301 (8), 2009.

[117] E.S. Shuman, J.F. Barry, and D. DeMille. Laser cooling of a diatomic molecule. *Nature*, 467(10):820 (4), 2010.

[118] M.H. Steinecker, D.J. Mccarron, Y. Zhu, and D. DeMille. Improved Radio-Frequency Magneto-Optical Trap of SrF Molecules. *ChemPhysChem*, 17(22):3664 (6), 2016.

[119] S. Truppe, H.J. Williams, M. Hambach, L. Caldwell, N.J. Fitch, E.A. Hinds, B.E. Sauer, and M.R. Tarbutt. Molecules cooled below the Doppler limit. *Nature Physics*, 13(12):1173 (6), 2017.

[120] L. Anderegg, B.L. Augenbraun, E. Chae, B. Hemmerling, N.R. Hutzler, A. Ravi, A. Collopy, J. Ye, W. Ketterle, and J.M. Doyle. Radio Frequency Magneto-Optical Trapping of CaF with High Density. *Physical Review Letters*, 119(10):103201 (5), 2017.

[121] L.W. Cheuk, L. Anderegg, B.L. Augenbraun, Y. Bao, S. Burchesky, W. Ketterle, and J.M. Doyle. Λ -Enhanced Imaging of Molecules in an Optical Trap. *Physical Review Letters*, 121(8):83201 (6), 2018.

[122] S. Ding, Y. Wu, I.A. Finneran, J.J. Burau, and J. Ye. Sub-Doppler Cooling and Compressed Trapping of YO Molecules at μ K Temperatures. *Physical Review X*, 10(2):21049 (9), 2020.

[123] D.J. McCarron, M.H. Steinecker, Y. Zhu, and D. DeMille. Magnetic Trapping of an Ultracold Gas of Polar Molecules. *Physical Review Letters*, 121(1):013202 (6), 2018.

[124] S. Stellmer, B. Pasquiou, R. Grimm, and F. Schreck. Laser Cooling to Quantum Degeneracy. *Physical Review Letters*, 110(26):263003 (5), 2013.

[125] J. Hu, A. Urvoy, Z. Vendeiro, V. Crepel, W. Chen, and V. Vuletić. Creation of a Bose-condensed gas of ^{87}Rb by laser cooling. *Science*, 358(6366):1078 (3), 2017.

[126] I. Kozyryev, L. Baum, K. Matsuda, B.L. Augenbraun, L. Anderegg, A.P. Sedlack, and J.M. Doyle. Sisyphus Laser Cooling of a Polyatomic Molecule. *Physical Review Letters*, 118(17):173201 (6), 2017.

[127] B.L. Augenbraun, Z.D. Lasner, A. Frenett, H. Sawaoka, C. Miller, T.C. Steimle, and J.M. Doyle. Laser-cooled polyatomic molecules for improved electron electric dipole moment searches. *New Journal of Physics*, 22(2):022003 (8), 2020.

[128] D. Mitra, N.B. Vilas, C. Hallas, L. Anderegg, B.L. Augenbraun, L. Baum, C. Miller, S. Raval, and J.M. Doyle. Direct laser cooling of a symmetric top molecule. *Science*, 369(6509):1366 (4), 2020.

[129] L. Baum, N.B. Vilas, C. Hallas, B.L. Augenbraun, S. Raval, D. Mitra, and J.M. Doyle. 1D Magneto-Optical Trap of Polyatomic Molecules. *Physical Review Letters*, 124(13):133201 (6), 2020.

[130] R.J. Bouwens, J.A. Hammerschmidt, M.M. Grzeskowiak, T.A. Stegink, P.M. Yorba, and W.F. Polik. Pure vibrational spectroscopy of S0 formaldehyde by dispersed fluorescence. *Journal of Chemical Physics*, 104(2):460 (20), 1996.

[131] M. Motsch, M. Schenk, M. Zeppenfeld, M. Schmitt, W.L. Meerts, P.W.H. Pinkse, and G. Rempe. Spectroscopy of the $\tilde{A}^1A_2 \leftarrow \tilde{X}^1A_1$ transition of formaldehyde in the 30140-30790 cm^{-1} range: The $2_0^1 4_0^3$ and $2_0^2 4_0^1$ rovibrational bands. *Journal of Molecular Spectroscopy*, 252(1):25 (6), 2008.

[132] J. Dalibard and C. Cohen-Tannoudji. Laser cooling below the Doppler limit by polarization gradients: simple theoretical models. *Journal of the Optical Society of America B*, 6(11):2023 (23), 1989.

[133] T. Junglen, T. Rieger, S.A. Rangwala, P.W.H. Pinkse, and G. Rempe. Slow ammonia molecules in an electrostatic quadrupole guide. *European Physical Journal D*, 31(2):365 (9), 2004.

[134] C.C. Chen, S. Bennetts, G.R. Escudero, F. Schreck, and B. Pasquiou. Sisyphus optical lattice decelerator. *Physical Review A*, 100(2):23401 (9), 2019.

[135] E.R. Hudson. Deceleration of continuous molecular beams. *Physical Review A*, 79(6):061407 (4), 2009.

[136] C. Sommer. Construction and Operation of a Cryogenic Source for Cold Polar Molecules. *Phd thesis, Technische Universität München, Garching bei München, Germany*, (April):160, 2011.

[137] H.W. Kroto. *Molecular Rotation Spectra*. John Wiley and Sons Ltd., New York, 1975.

[138] R.N. Zare, A.L. Schmeltekopf, W.J. Harrop, and D.L. Albritton. A Direct Approach for the Reduction of Diatomic Spectra to Molecular Constants for the Construction of RKR Potentials. *Journal of Molecular Spectroscopy*, 46(1):37 (30), 1973.

[139] T. Bergeman and R.N. Zare. Fine structure, hyperfine structure, and Stark effect in the NO A $^2\Sigma^+$ state by optical radio-frequency double resonance. *The Journal of Chemical Physics*, 61(11):4500 (15), 1974.

[140] H. Bethe, F. Hund, N.F. Mott, W. Pauli, A. Rubinowicz, G. Wentzel, and A. Smekal. *Quantentheorie (Handbuch der Physik Band 24)*. Springer, 2. auflage edition, 1933.

[141] L.A. Kaledin, J.C. Bloch, M.C. McCarthy, and R.W. Field. Analysis and Deperturbation of the $A^2\Pi$ and $B^2\Sigma^+$ states of CaF. *Journal of Molecular Spectroscopy*, 197(2):289 (8), 1999.

[142] P.M. Sheridan, J.G. Wang, M.J. Dick, and P.F. Bernath. Optical-Optical Double Resonance Spectroscopy of the $C^2\Pi$- $A^2\Pi$ and $D^2\Sigma^+$-$A^2\Pi$ Transitions of SrF. *Journal of Physical Chemistry A*, 113(47):13383 (7), 2009.

[143] A. Bernard and R. Gravina. The emission spectrum of yttrium monoxide - New rotational and vibrational results on the $A^2\Pi$-$X^2\Sigma^+$ system. *Astrophysical Journal Supplement Series*, 52:443 (8), 1983.

[144] A.V. Avdeenkov and J.L. Bohn. Collisional dynamics of ultracold OH molecules in an electrostatic field. *Physical Review A*, 66(5):052718 (10), 2002.

[145] M.G. Kozlov. Linear polyatomic molecules with Π ground state: Sensitivity to variation of the fundamental constants. *Physical Review A*, 87(3):032104 (9), 2013.

[146] I. Kozyryev. Laser Cooling and Inelastic Collisions of the Polyatomic Radical SrOH. *Phd thesis, Harvard University, Cambridge MA, USA*, (May):203, 2017.

[147] P.F. Bernath. *Spectra of Atoms and Molecules*. Oxford University Press, 2005.

[148] C.M. Western. PGOPHER: A program for simulating rotational, vibrational and electronic spectra. *Journal of Quantitative Spectroscopy and Radiative Transfer*, 186:221 (22), 2017.

[149] A.R. Edmonds. *Angular Momentum in Quantum Mechanics*. Princeton University Press, 4 edition, 1996.

[150] C.M. Tesch and R. de Vivie-Riedle. Quantum Computation with Vibrationally Excited Molecules. *Physical Review Letters*, 89(15):157901 (4), 2002.

[151] F. Robicheaux. A proposal for laser cooling of OH molecules. *Journal of Physics B: Atomic, Molecular and Optical Physics*, 42(19):195301 (18), 2009.

[152] N.E. Shafer-Ray, K.A. Milton, B.R. Furneaux, E.R.I. Abraham, and G.R. Kalbfleisch. Design of a biased Stark trap of molecules that move adiabatically in an electric field. *Physical Review A*, 67(4):045401 (4), 2003.

[153] G. Xu. Manipulation and quantum control of ultracold atoms and molecules for precision measurements. *Phd thesis, The University of Texas at Austin*, page 199, 2011.

[154] K.W. Miller, S. Dürr, and C.E. Wieman. rf-induced Sisyphus cooling in an optical dipole trap. *Physical Review A*, 66(2):023406 (8), 2002.

[155] W. Gordy and R.L. Cook. *Microwave Molecular Spectra*. John Wiley, New York, 1984.

[156] G. Herzberg. *Molecular Spectra and Molecular Structure: III. Electronic Spectra and Electronic Structure of Polyatomic Molecules*. Van Nostrand Reinhold Company Ltd, 1966.

[157] C. Zhang, B.L. Augenbraun, Z.D. Lasner, N.B. Vilas, J.M. Doyle, and L. Cheng. Accurate prediction and measurement of vibronic branching ratios for laser cooling linear polyatomic molecules. *The Journal of Chemical Physics*, 155(9):091101 (7), 2021.

[158] S. Truppe. New Physics with Cold Molecules : Precise Microwave Spectroscopy of CH and the Development of a Microwave Trap. *Phd thesis, Imperial College London*, (November):249, 2014.

[159] G.C. Dousmanis, T.M. Sanders, and C.H. Townes. Microwave Spectra of the Free Radicals OH and OD. *Physical Review*, 100(6):1735 (20), 1955.

[160] S. Weinreb, A.H. Barrett, M.L. Meeks, and J.C. Henry. Radio Observations of OH in the Interstellar Medium. *Nature*, 4909(11):829 (3), 1963.

[161] M. Zachwieja. The $A^2\Delta$ - $X^2\Pi$ Band System of the ^{13}CH Radical. *Journal of Molecular Spectroscopy*, 182:18 (16), 1997.

[162] K.H. Becker, H.H. Brenig, and T. Tatarczyk. Lifetime measurements on electronically excited CH(A $^2\Delta$) radicals. *Chemical Physics Letters*, 71(2):242 (4), 1980.

[163] P.F. Bernath, C.R. Brazier, T. Olsen, R. Hailey, W.T.M.L. Fernando, C. Woods, and J.L. Hardwick. Spectroscopy of the CH Free Radical. *Journal of Molecular Spectroscopy*, 147(1):16 (11), 1991.

[164] G. Valtolina, K. Matsuda, W.G. Tobias, J.-R. Li, L. De Marco, and J. Ye. Dipolar evaporation of reactive molecules to below the Fermi temperature. *Nature*, 588(12):239 (5), 2020.

[165] D. Patterson and J.M. Doyle. A slow, continuous beam of cold benzonitrile. *Physical Chemistry Chemical Physics*, 17(7):5372 (4), 2015.

[166] D. Patterson. Buffer Gas Cooled Beams and Cold Molecular Collisions. *Phd thesis, Harvard University, Cambridge MA, USA*, (March):192, 2010.

[167] X. Wu. Centrifuge Decelerator for Cold Polar Molecules Produced by Buffergas Cooling. *Master thesis, Technische Universität München, Garching bei München, Germany*, (March):83, 2010.

[168] S. Pohle. A Cryogenic Source for Cold Polar Molecules. *Diploma thesis, Technische Universität München, Garching bei München, Germany*, (July):70, 2007.

[169] I. Özdemir and D. Perinic. Helium sticking coefficient on cryopanels coated by activated carbon. *Journal of Vacuum Science Technology A*, 16(4):2524 (4), 1998.

[170] M. Motsch, C. Sommer, M. Zeppenfeld, L.D. van Buuren, P.W.H. Pinkse, and G. Rempe. Collisional effects in the formation of cold guided beams of polar molecules. *New Journal of Physics*, 11(5):055030 (18), 2009.

[171] M. Motsch. Cold Guided Beams of Polar Molecules. *Phd thesis, Technische Universität München, Garching bei München, Germany*, (December):151, 2009.

[172] M. Zeppenfeld. Electric Trapping and Cooling of Polyatomic Molecules. *Phd thesis, Technische Universität München, Garching bei München, Germany*, (September):112, 2013.

[173] R. Glöckner. Rotational-state cooling and detection of trapped CH3F molecules. *Phd thesis, Technische Universität München, Garching bei München, Germany*, (December):89, 2015.

[174] A. Prehn. An Ultracold Gas of Electrically Trapped Formaldehyde. *Phd thesis, Technische Universität München, Garching bei München, Germany*, (May):150, 2018.

[175] R. Braun and P. Hess. Optimization of a commercial quadrupole mass spectrometer for time-of-flight measurements of laser desorption. *International Journal of Mass Spectrometry and Ion Processes*, 125(2-3):229 (11), 1993.

[176] H.C.W. Beijerinck, R.G.J.M. Moonen, and N.F. Verster. Calibration of a time-of-flight machine for molecular beam studies. *Journal of Physics E: Scientific Instruments*, 7(1):31 (6), 1974.

[177] X. Wu, T. Gantner, M. Koller, M. Zeppenfeld, S. Chervenkov, and G. Rempe. Suppl. Material: A cryofuge for cold-collision experiments with slow polar molecules. *Science*, 358(6363):21, 2017.

[178] J.L. Bohn, M. Cavagnero, and C. Ticknor. Quasi-universal dipolar scattering in cold and ultracold gases. *New Journal of Physics*, 11(5):055039 (18), 2009.

[179] M.T. Bell and T.P. Softley. Ultracold molecules and ultracold chemistry. *Molecular Physics*, 107(2):99 (34), 2009.

[180] A. Christianen, M.W. Zwierlein, G.C. Groenenboom, and T. Karman. Photoinduced Two-Body Loss of Ultracold Molecules. *Physical Review Letters*, 123(12):123402 (6), 2019.

[181] B.G.U. Englert. Sisyphus-Kühlung von polyatomaren Molekülen. *Phd thesis, Technische Universität München, Garching bei München, Germany*, (August):150, 2013.

[182] M. Kirste, X. Wang, H.C. Schewe, G. Meijer, K. Liu, A. van der Avoird, L.M.C. Janssen, K.B. Gubbels, G.C. Groenenboom, and S.Y.T. van de Meerakker. Quantum-State Resolved Bimolecular Collisions of Velocity-Controlled OH with NO Radicals. *Science*, 338(6110):1060 (3), 2012.

[183] M.L. Wall, K. Maeda, and L.D. Carr. Simulating quantum magnets with symmetric top molecules. *Annalen der Physik*, 525(10-11):845 (20), 2013.

[184] C.M. Bender and S.A. Orszag. *Advanced Mathematical Methods for Scientists and Engineers I Asymptotic Methods and Perturbation Theory.* Springer, 1 edition, 1991.

[185] E. Kamke. *Differentialgleichungen Lösungsmethoden und Lösungen 1.* Springer, 6 edition, 1979.

[186] Y.V. Suleimanov. Zeeman relaxation of magnetically trapped Eu atoms. *Physical Review A*, 81(2):022701 (8), 2010.

[187] A. Lagendijk, I.F. Silvera, and B.J. Verhaar. Spin exchange and dipolar relaxation rates in atomic hydrogen: Lifetimes in magnetic traps. *Physical Review B*, 33(1):626 (3), 1986.

[188] J. M.V.A. Koelman, H.T.C. Stoof, B.J. Verhaar, and J.T.M. Walraven. Lifetime of magnetically trapped ultracold atomic deuterium gas. *Physical Review B*, 38(13):9319 (4), 1988.

[189] A.J. Moerdijk and B.J. Verhaar. Collisional two- and three-body decay rates of dilute quantum gases at ultralow temperatures. *Physical Review A*, 53(1):19 (4), 1996.

[190] J.L. Bohn. Inelastic collisions of ultracold polar molecules. *Physical Review A*, 63(5):052714 (5), 2001.

[191] M. Zeppenfeld. Nondestructive detection of polar molecules via Rydberg atoms. *Europhysics Letters*, 118(1):13002 (6), 2017.

[192] W. Hüttner, editor. *Landolt-Börnstein - Group II Molecules and Radicals.* volume 29c edition, 2010.

[193] D.R. Lide, editor. *CRC Handbook of Chemistry and Physics*. 71th edition, 1990.

[194] K.B. Davis, M.-O. Mewes, M.A. Joffe, M.R. Andrews, and W. Ketterle. Evaporative Cooling of Sodium Atoms. *Physical Review Letters*, 74(26):5202 (4), 1995.

[195] A.B. Henson, S. Gersten, Y. Shagam, J. Narevicius, and E. Narevicius. Observation of Resonances in Penning Ionization Reactions at Sub-Kelvin Temperatures in Merged Beams. *Science*, 338(6104):234 (6), 2012.

[196] E. Urban, T.A. Johnson, T. Henage, L. Isenhower, D.D. Yavuz, T.G. Walker, and M. Saffman. Observation of Rydberg blockade between two atoms. *Nature Physics*, 5(2):110 (5), 2009.

[197] M.D. Lukin, M. Fleischhauer, R. Cote, L.M. Duan, D. Jaksch, J.I. Cirac, and P. Zoller. Dipole Blockade and Quantum Information Processing in Mesoscopic Atomic Ensembles. *Physical Review Letters*, 87(3):037901 (4), 2001.

[198] G. Pupillo, A. Micheli, M. Boninsegni, I. Lesanovsky, and P. Zoller. Strongly Correlated Gases of Rydberg-Dressed Atoms : Quantum and Classical Dynamics. *Physical Review Letters*, 104(22):223002 (4), 2010.

[199] Y.O. Dudin and A. Kuzmich. Strongly Interacting Rydberg Excitations of a Cold Atomic Gas. *Science*, 336(6083):887 (4), 2012.

Acknowledgments

First of all I want to thank my doctoral advisor Gerhard Rempe for giving me the opportunity to work in this amazing group and to do research at the highest level. The supportive atmosphere in the Quantum Dynamics division are a consequence of your leadership. In addition, I particularly want to thank you for the freedom and support you give us to try out new ideas.

Special thanks goes to Martin Zeppenfeld for helping us to solve all kinds of problems. Whenever we were stuck we knew that we can rely on him helping us to solve the problem. Without his support this thesis would not have been possible.

Next I want to thank Thomas Gantner for introducing me to the experiment and the field of cold molecules. I really appreciate your willingness to answer every single of my questions as well as the great working atmosphere and the fun in the lab.

Special thanks also goes to Isabel Rabey for the knowledge and expertise about molecular physics she brought to our experiment. Furthermore I want to thank her for the positive attitude no matter what went wrong in the lab.

I also want to specifically thank Florian Jung and Jindaratsamee Phrompao for their dedication and support to measure the data presented in this thesis. I wish you all the best for your remaining time at MPQ.

Next I want to thank Xing Wu for sharing his knowledge about the Cryofuge experiment and molecular physics in general with me.

Big thanks also goes to the technicians Tobias Urban, Florian Furchtsam, Johannes Siegl and Tom Wiesmeier for their great effort and expertise to extend and improve the experiment.

Furthermore I want to thank the molecule team and the whole Quantum Dynamics division for the amazing atmosphere, the readiness to help and the fun outside of the lab.

Last but not least I want to thank my familiy for the constant support not only throughout this thesis but also during my studies. Without you this thesis would not have been possible.